On Dynamical Causes of Eddy Variability in the Ocean

Stavroula Biri

Department of Earth Sciences

University of Hamburg

Dissertation submitted for the degree of

Dr. rer. nat.

Hamburg, 2013

I hereby declare, on oath, that I have written the present dissertation on my own and have not used other than the acknowledged resources and aids.

Hamburg 2013,

Acknowledgements

Abstract

The temporal changes of the oceans eddy variability and the underlying dynamical causes are investigated. The study is based on a 18.5 year long time series of satellite altimetry sea surface height (SSH) anomalies (TOPEX/Poseidon, Jason-1 and Jason-2), from which statistics for the eddy kinetic energy field (EKE) are computed. In this study it is demonstrated that the most energetic regions coincide with major current systems, meandering jets and frontal areas. These are the domains where SSH non-gaussianity is acquainted most likely due to inhomogeneities in the ocean. It is also shown that the distribution of SSH skewness and kurtosis can be used to assess the seasonal variations of meandering jets and ocean surface circulation processes. The extent to which the eddy field is reacting to changes in the wind forcing is addressed. EKE fields, computed from an eddy-resolving global circulation model STORM driven both by NCEP forcing and by climatology, are used complementary to the altimetry. The results suggest that changes of EKE depict a complex pattern and are far from uniform. A comparison of the time series of wind stress and EKE suggests that changing winds cause a response in eddy activity. In several parts of the ocean there is no direct relation between the wind forcing and the increase in EKE, pointing to non-local forcing effects of eddy variability. On basin average, changes in EKE appear to be correlated with climate modes. Ocean variability contains all temporal and spatial scales. The investigation of temporal changes in EKE and its causes was extended through spectral analysis, which is appropriate for estimating the impact of different scales on the overall energy distribution. The global frequency spectra for altimetry is aliased by tidal residuals. In the Atlantic through a joint data-model analysis it is evident that as the resolution increases the model's spectra gets closer to the altimetry. Regionally, the shape of the frequency spectra of SSH has steeper slopes at higher frequencies and flatter slopes at lower frequencies. The slopes of wavenumber spectra in high energy regions, dominated by non-linearity, follow roughly k^{-4} or k^{-3} at the mesoscale. Thus, surface quasi-geostrophy turbulence theory appears more appropriate to provide a dynamical explanation of these spectral slopes. The low energy regions have flatter slopes ranging from -3 to -2. Further research is needed in order to clarify the causes of EKE on a global scale.

Contents

List of Figures

List of Tables

Chapter 1

Introduction

The oceans cover 71 % of the earth's surface· due to the high heat capacity of water the oceans are an important climate regulator. The ocean - as a fluid constantly in motion - circulation and the interaction between sea and the atmosphere at the ocean surface boundary layer are fields undergoing investigation through both observations and model simulations in global as well as in regional scale.

In general, "climate variations range from the large-amplitude climatic transitions of the past millennia to small-amplitude fluctuations on shorter time scales" [Dijkstra, 2008]. Large scale characteristics of the ocean circulation can be identified by the mean flow field, which consists of sea surface currents as the Gulf Stream or the Kuroshio Current. When the mean flow becomes unstable, mesoscale features emerge and the global flow field becomes more complex. My research is focused on the mesoscale circulation, which refers to a class of energetic phenomena of spatial scales ranging from 50 to 500 km and time scales ranging from a few days to several months. Mesoscale circulation occurs in the form of linear Rossby waves and of non-linear eddies [Chelton et al., 2007]. Part of the complexity of the mesoscale field is due to the fact that baroclinic eddies may be advected by the mean flow into regions with quite different properties from where they were initially formed [Vallis, 2006].

Altimetry is based on the fact that the ocean can be thought as a surface of equal potential of the earth's gravity field, which would be a sphere ignoring the earth's rotation, while including rotation into the equation then the earth's elliptical shape arises. However, the ocean deviates from the ideal ellipsoid due to variations in the earth's gravity field. Radar altimeters can be used to measure these variations in sea surface height.

One of the first altimeters, TOPEX/Poseidon, was launched on 10 August 1992

as a joint satellite mission between the U.S. and the French space agency. It was the first radar altimeter to provide continuous global coverage of sea surface height (SSH) measurements. TOPEX/Poseidon flew on non-sun-synchronous and prograde orbit at the altitude of 1336 km, so as to minimise atmospheric drag and gravity forces acting on the satellite, and to make orbit determination more accurate. With inclination of an 66° measures ocean topography covering almost 90 percent of the ocean with an accuracy of 4 cm. A repeat cycle of 9.916 days was selected with a distance between successive tracks of the order of 315 km at the equator. Satellite altimetry was a pioneering achievement which led to a new understanding of the patterns of ocean circulation and its effect on climate. Also, due to its global coverage satellite altimetry provided the possibility to compare ocean general circulation models to observations. A graphical representation of the altimeter's measuring principle is given in **Fig. 1.1**.
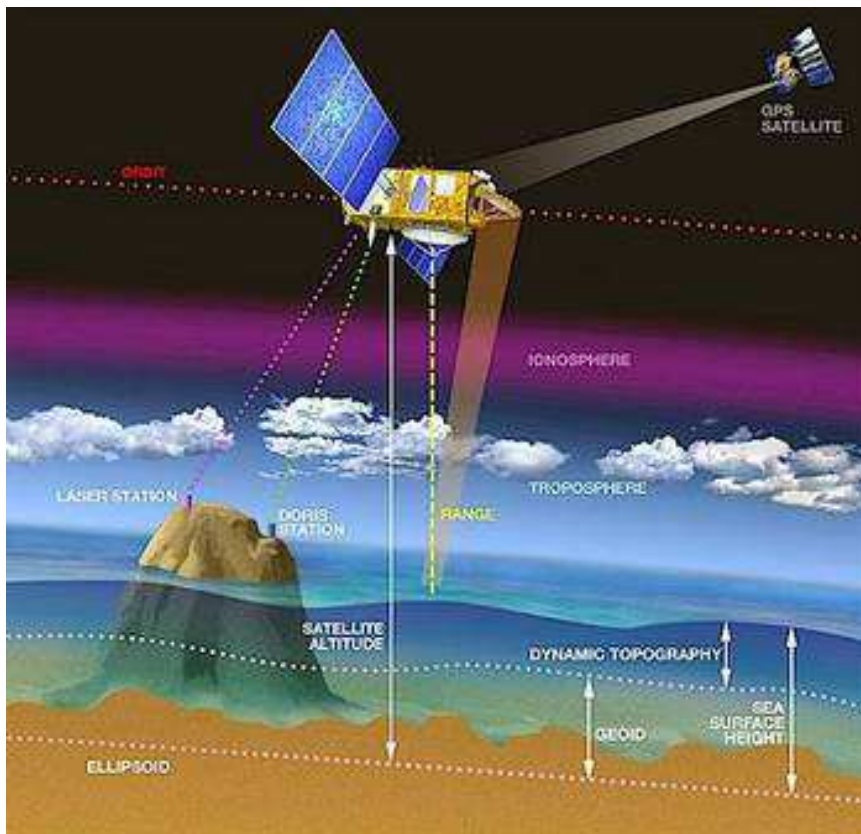
Figure 1.1: TOPEX/Poseidon's basic measuring principle (credits:CNES, http://www.aviso.oceanobs.com/en/altimetry/principle/basic-principle.html).

TOPEX/Poseidon carried the following instruments:

- Laser Retroreflector Array reflects laser signals from a network of 10 to 15 ground laser tracking stations to provide tracking data for precise orbit determination and the altimeter bias calibration.

- Dual-frequency Doppler tracking system receiver (Doris) uses a two-channel receiver (401.25 MHz and 2036.25MHz) to observe the Doppler signals from a network of about 50 ground transmitting beacons. It provides all-weather global tracking of the satellite for precise orbit determination. Doris beacons are equipped with meteorological sensors measuring temperature, humidity, and atmospheric pressure to correct for atmospheric effects on the transmitted signals. The Doris signals are transmitted at two frequencies to allow the removal of the effects of ionospheric free electrons on the tracking data as well as the altimeter signals.

- The GPSDR operating at 12227.6 MHz and 1575.4 MHz, receives signals from up to 6 GPS satellites. The GPS antenna is mounted on a long boom to reduce multipath effects which can severely corrupt the measurements.

- A dual-frequency NASA Radar Altimeter operating at 13.6 GHz (Ku band) and 5.3 GHz (C band) simultaneously, the measurements made at the two frequencies are combined to obtain the altimeter height of the satellite above the sea, the wind speed modulus, the significant wave height and the ionospheric correction.

- The three-frequency Topex Microwave Radiometer which measures the sea surface microwave emissivity at frequencies 18 GHz to remove wind speed on the water vapor measurement, 21 GHz to measure water vapor and 37 GHz to remove the effect of cloud cover on the water vapor measurement. Measurements are combined to obtain the error in the satellite range measurements caused by pulse delay due to water vapor and to obtain the sigma naught correction for liquid water absorption.

- Single frequency Solid State radar ALTimeter operates at a single frequency of 13.65 GHz (Ku band) and validates the new technology of a low-power (49 W), light-weight altimeter for future Earth observing missions. It shares the same antenna as the NRA; thus only one altimeter operates at any given time. It operates about 10% of the time, or one cycle over ten.

Jason-1 launched on 7 December 2001 continues measuring sea surface height following

the same principles as TOPEX/Poseidon, and it was followed by Jason-2 launched on 20 June 2008.

The following sections will provide the scientific reasoning of this thesis, starting from the motivation and the description of the scientific goals. A short outline of the thesis is also provided in the last section of this chapter.

1.1 Scientific Background and Motivation

The ocean is conditioned by atmospheric radiation, wind stress, temperature, pressure and rainfall. The ocean is the flywheel or the inertia on the global heat engine and serves to smooth out the high-frequency fluctuations of the atmosphere. The two fluids are strongly coupled, having both positive and negative feedback loops and greatly differing time constants [Apel, 1987]. Several frequencies of variability are clearly related to forcing mechanisms. However, variability can also arise through processes internal in the climate system giving rise to frequencies that are not directly related to the temporal variability of the forcing [Dijkstra, 2008].

Mesoscale variability which resembles two dimensional turbulence, is a flow characterised by coherent vortices, separated by near-irrotational regions dominated by strong straining motions [Gille and Llewellyn Smith, 2000]. In the ocean, the energy of mesoscale processes generally exceeds the energy of the mean flow by an order of magnitude or more [Morrow and Le Traon, 2011]. Due to the strong effect of mesoscale eddies on the sea surface properties they can be observed on images of sea surface temperature and ocean colour, through which information on the dynamic processes of eddies can not be conveyed. This becomes possible from sea surface height observations [Fu et al., 2010]. Recent studies [Chelton et al., 2007] revealed that most of the westward propagation, previously attributed to Rossby waves actually consists of non-linear mesoscale eddies that could not be resolved before due to TOPEX/Poseidon's sampling pattern. However, Rossby waves can be detected in regions of low eddy energy as for example the eastern Pacific.

Chelton et al. [2011] applying an SSH-based eddy detection and tracking procedure tracked approximately $177,000$ eddies with a lifetime of 4 weeks or longer. The number of eddies however, decreased with increasing lifetimes. The trajectories of the eddies indicated that they occur everywhere, while there are slightly more cyclonic than anticyclonic eddies with lifetimes more than 16 weeks. The regions with the fewest eddies were located in the northeast and southeast Pacific Ocean. Their research suggests that eddies form nearly everywhere, with formation rates being highest in the eastern

boundary currents systems and concluded that eddies are most likely generated by baroclinic instability of the vertically sheared ocean current.

The mean radius scale of the eddies varies with latitude, decreasing poleward. These scales are larger than the baroclinic Rossby radius of deformation at mid and high latitudes and consistent with the up-scale energy cascade as described by quasi-geostrophic turbulence [Fu et al., 2010]. Eddies can be identified apart from their radius scale also by their other characteristic, non-linearity.

The ocean is driven by density differences and wind-forcing at the surface, their combination produces enhanced stratification and associated shear in the upper $50-1000\,\text{m}$ of the ocean. Stratification is larger in the upper ocean, decaying into an almost unstratified abyss. The sloping isopycnals indicate that there is a pool of available potential energy that might be converted into kinetic energy and so the ocean is potentially baroclinically unstable [Vallis, 2006]. Kinetic energy of the circulation system is strongly dominated by the geostrophic motions whose spatial structure can be controlled by a number of competing processes including atmospheric forcing, up and down-scale turbulent energy cascades, topographic interactions etc. [Ferrari and Wunsch, 2009].

The ocean as a turbulent fluid demonstrates a tight relationship between the large-scale circulation and small-scale mixing, with energy being exchanged amongst all scales of motion [Ferrari and Wunsch, 2009]. The forcings of mesoscale circulation are mainly instabilities from the large-scale circulation and interactions between currents, bathymetry and the direct forcing by the wind. Since eddies transport heat, mass, momentum and tracers and interact with the mean flow field, it is important to understand eddy dynamics, their transport properties and their impact on climate. Furthermore the exchange of momentum between the ocean and atmosphere via wind stress is important for the study of air-sea interactions, climate variability and ocean processes [Collins et al., 2012].

In that context it is important to also consider the seasonal and interannual variations in eddy kinetic energy (EKE). On a global scale the seasonal EKE variations at high latitudes have been associated with seasonal wind stress variations, even though other forcing mechanisms may play an important role [Brachet et al., 2004; Scharffenberg and Stammer, 2010; Stammer, 1997b]. The seasonal variations of EKE in correspondence with forcing agents (such as the wind stress, climate modes etc.) have also been investigated regionally [Meredith and Hogg, 2006; Morrow et al., 2010; Qiu and Chen, 2004, and others], attributing the variations to seasonal shifts of the position of fronts, climate mode forcing and variation in the intensity of baroclinic instability.

The physical processes which lead to the generation of eddies are under ongoing

investigation. Once eddies are generated, eddy-eddy interactions transfer energy to large scale barotropic and first baroclinic motions and to small scale, surface-trapped eddies [Ferrari and Wunsch, 2009]. The general picture is that of a large-scale flow which is unstable to eddies smaller in scale. These eddies grow and develop smaller eddies and energy is transferred into smaller and smaller scales in a cascade process. When eddies that are sufficiently small - able to feel the effect of viscosity - are generated, the energy is drained away [Vallis, 2006]. The energy and scales of the variability are found to be highly inhomogeneous in space, exhibiting dependence on latitude as well as proximity to strong mean flows [Fu, 2009].

"A turbulent flow has eddies with a spectrum between some upper and lower bounds, the former often determined by the forcing scale or the domain scale, and the latter usually by viscosity. The individual eddies come and go and are inherently unpredictable" [Vallis, 2006]. Frequencies smaller than the Coriolis frequency are considered to be almost completely geostrophically balanced at least below the surface boundary layers. The geostrophic eddy field dominates the energy content at sub-inertial frequencies, whereas mixed layer turbulence is the largest reservoir at super-inertial frequencies [Ferrari and Wunsch, 2009]. In steady state the kinetic energy is constant, at equilibrium the kinetic energy generated by surface stresses is balanced by the conversion of kinetic energy into potential energy, into compressive internal energy and mostly viscous dissipation. The generation and destruction of oceanic potential and internal energy is confined to the surface mixed layer [Wunsch and Ferrari, 2004].

From the space domain point of view, the spectra at high wavenumber end exhibit a power law of the form k^{-p}, where the exponent can be interpreted as an indicator of the dynamic process governing eddy energy transfer in spectral space [Fu et al., 2010]. In previous studies [Fu, 1983; Le Traon et al., 2008; Stammer, 1997a] the governing dynamics at high wavenumbers was argued to be compliant with geostrophic turbulence theory or surface quasi-geostrophic turbulence identifying exponents varying from -5 to $-11/3$ in high eddy energy regions and around -2 in low eddy energy regions.

Furthermore from previous studies [Ferrari and Wunsch, 2010] it appears that turbulent eddy-eddy interactions shape the wavenumber spectrum at small scales. It is argued by Ferrari and Wunsch [2010] that " despite the overwhelming evidence that oceanic motions are turbulent, in the sense that non-linear interactions rapidly redistribute energy across wavenumbers, classical theories of turbulence cannot account for many aspects of the observations. First, turbulence theories assume that eddies decorrelate on timescales shorter than a wave period, so that energy can spread away from the linear wave dispersion relationship. However the spectra show that the bulk of

the mid-latitude ocean kinetic energy is confined to a narrow strip in k_x, ω space suggesting that (non-linear) wave dynamics remains relevant despite any truly turbulent interactions. Second, turbulent theories assume that there is a wide range of scales where dynamics are controlled by internal interactions and not by external forcing. Observations suggest that wind forcing remains important on all scales"

1.2 Scientific Goals

The research, as part of this thesis, has as a goal to improve our understanding of the eddy variability in the global ocean, the extent of its temporal changes and potentially underlying causes. These questions are intimately related but were never investigated conclusively in combination.

From previous studies it is already known that the distribution of sea surface height is not Gaussian (e.g. Hughes et al. [2010]; Sura and Gille [2010]; Thompson and Demirov [2006]). We revisit this topic by studying sea surface height anomaly dynamics using the first four moments of sea surface height and the velocity field. The latter is computed using the Jason-1 - TOPEX/Poseidon (JTP) tandem mission sea surface height. Previous studies [Thompson and Demirov, 2006] showed that skewness and kurtosis can be used as a means to reveal geographical pattern of the eddies in the global ocean (sense of rotation, extreme events). Recently the non-Gaussian higher order statistics where studied in more detail from a dynamical aspect [Hughes et al., 2010; Sura, 2011; Sura and Gille, 2010], showing that non-Gaussian statistics of sea surface height can be described by stochastic theory. I investigate the seasonal variations of higher-order statistics as a means to infer information about the system dynamics.

I study temporal changes of the ocean's eddy variability and underlying dynamical causes. The goal is specifically to investigate the extent to which the eddy field is reacting to changes in the wind forcing. To that end interannual to decadal changes in eddy variability are identified in terms of normalized temporal trends of sea surface height and EKE and are compared with changes in wind stress derived from NCEP/NCAR reanalysis-1 [Kalnay et al., 1996] daily averages of 10 m wind speed components. Results are compared also with 30 year-long sea surface height and EKE time series obtained from a high resolution, eddy resolving global model STORM, driven by NCEP/NCAR reanalysis-1 [Kalnay et al., 1996] forcing and also with a second run forced by 15-yr ERA-15 climatology. Given that variability in the model's eddy kinetic energy agrees surprisingly well with the observed changes, the model is used to investigate sources and sinks of kinetic energy as a function of time to identify dynamical causes of what

is being observed.

In the last section I investigate spectral sea level relations, their interpretation in terms of ocean dynamics and the comparison of respective results in terms of underlying dynamical processes. Herein I investigate spectral sea level relations in the frequency and wavenumber domain. Spectra have been computed before, even since the early years of satellite altimetry [Fu, 1983], however understanding the differences in the shape of the spectra between high and low eddy energy regions remains open [Fu et al., 2010]. To proceed I compare observed spectra with those obtained from MIT general circulation model (MITgcm) simulation over the Atlantic (from 30°S to 70°N) with resolutions ranging from 1/3°, 1/6°, 1/12° to 1/24° and also STORM model. Spectra from observational and simulation sources are being interpreted in terms of ocean dynamics.

These overarching goals will be addressed by investigating three questions:

1. What can we learn from higher order statistics such as skewness and kurtosis of sea surface height about dynamical processes leading to the observed eddy variability and its changes on the seasonal cycle? (Chapter 3)

2. To which extent is the eddy field reacting to changes in the atmospheric forcing notably interannual to decadal changes of the wind forcing and can such relation be used to quantify sources of eddy variability? (Chapter 4)

3. Can a joint model-data analysis of frequency and wavenumber spectra be used to identify dynamical principles leading to observed sea surface height timeseries and to separate those from noise effects in the data? (Chapter 5)

In the next section an outline of the thesis structure will be given.

1.3   Thesis Outline

This thesis is organised as follows:

In Chapter 2, an overview of the data sets provided by altimetry, STORM and MITgcm models is given. In addition, a detailed description of the statistical and computational methods used throughout the thesis is provided.

Chapter 3, simple statistics are utilized as a means to unveil physical aspects in the ocean. Here the theoretical background of using skewness and kurtosis as statistical tool will be explained, focusing on the physical processes that can be observed through them by investigating seasonal differences in the distributions of skewness and kurtosis

and comparing them to the corresponding velocity components pattern derived from the TOPEX/Poseidon-Jason-1 tandem mission where isotropy does not have had to be assumed. Global and regional results will be presented and discussed. The content of this chapter, is to be submitted for peer-reviewed publication entitled *A Probabilistic Description of the Mesoscale Eddy Field in the Ocean* by S. Biri, M. G. Scharffenberg and D. Stammer.

In Chapter 4 the temporal changes of the ocean's eddy variability and the underlying dynamical causes are investigated. Specifically, I revisit the question to which extent the eddy field is reacting to changes in the wind forcing. The normalized temporal trends of sea surface height anomalies and EKE are used to infer decadal changes in eddy variability. I first investigate the geographical pattern of EKE variability and its causes. Through a comparison of the time series of wind stress and EKE I approach the effect of the external forcing onto the temporal evolution of the kinetic energy field and the response of the latter to the former (if existing). Another important influence on to EKE comes from the climate modes. In order to estimate this effect I study how EKE correlates to the appropriate climate index on a basin scale. Since I establish that STORM results are in very good agreement with altimeter results, I use the model simulation to approach how each individual term of the Lorenz energy cycle interacts with EKE. However, I expect that EKE can also be effected by non-local forcing effects of eddy variability or other processes. Results are presented and discussed. The content of this chapter, is to be submitted for peer-reviewed publication entitled *Causes for Temporal Variations of Eddy Kinetic Energy in the Ocean* by S. Biri, D. Stammer and J.-S. von Storch.

Chapter 5 is concerned with spectral sea level relations in the frequency and wavenumber domains. In this chapter frequency and wavenumber spectra of sea surface height anomalies are investigated in terms of ocean dynamics. The contribution from errors in the altimeter observations is discussed. The observed spectra are compared with those obtained from the MITgcm run over the North Atlantic, with different resolutions and with the STORM model. Results potentially can serve to identify local modes of variability previously not identified in the observations.

The final Chapter 6 provides an overview of the findings contained in this thesis and the respective concluding remarks, as well as recommendations for future work.

Chapter 2

Data and Methodology

2.1 Introduction

The measuring principle of the radar altimeter onboard TOPEX/Poseidon and its successors Jason-1 and Jason-2 (**Fig. 1.1**) is the transmission of a short high frequency microwave pulse toward the ocean surface through a 1.5 m parabolic dish antenna. The interval between two consequent bursts is variable and depends on the altitude of the satellite. The pulse is partially reflected back to space and, the time needed for the pulse to travel from the satellite to the ocean surface and back can be determined very accurately [Fu and Cazenave, 2001]. The sea surface height (SSH) can then be calculated using the travel time of the pulse in combination with a well defined orbit,
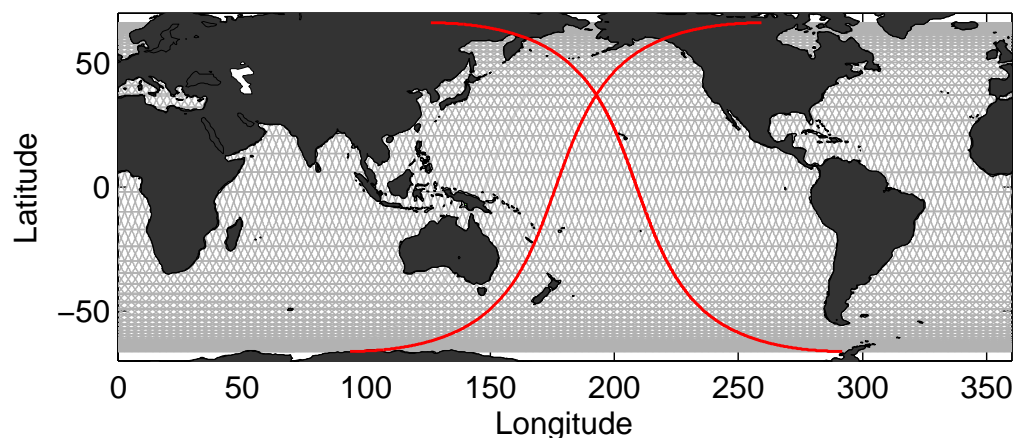
Figure 2.1: TOPEX/Poseidon's ground tracks.

reference ellipsoid and geoid.

However, the estimation of SSH should be additionally corrected for several parameters such as the path delay in the return signal of the radar due to the electron content in the uppermost layer of the atmosphere (ionosphere). Further details on the corrections applied to altimetry can be found in Fu and Cazenave [2001] along with a full description of satellite altimetry applications.

In **Fig. 2.1** the vast global coverage of TOPEX/Poseidon's ground tracks is shown, a sample of an ascending and a descending arc is highlighted in red. The choice of the inclination at $66°$ is advantageous both for the coverage (which reaches almost 90% of the world oceans) and for avoiding tidal aliasing, while in combination to the 9.916 days repeat cycle results in having around 315 km distance between successive tracks at the equator.

Satellite altimetry is a mature and well understood technology, firmly suitable for investigating mesoscale phenomena. With the continuation of the TOPEX/Poseidon mission through the JASON satellite series, we can produce a continuous altimetry time series from which we gain insight into many important aspects of the global and regional ocean circulation. In addition, we take advantage of the fact that altimetric measurements have been used for several years and are in that sense free of inadequacies of the earlier years.

In this chapter the data sets used throughout the thesis will be introduced and their interrelation will be described. Also a thorough introduction to the methodology used at the consequent chapters will be given.

2.2 Data

2.2.1 Altimetry

This thesis is based on sea surface height data from the global ocean topography experiment TOPEX/Poseidon, Jason-1 and Jason-2 satellites with horizontal along-track resolution of 6.2 km and repetitivity of 9.9156 days, which were obtained using the Radar Altimeter Database System (RADS), Version 3.0. On the data set corrections for the effects of the inverted barometer, the ionosphere, the wet and dry troposphere, the geophysical tides and the atmospheric dynamics were applied. We used sea surface height data that span from January 1, 1993, to June 30, 2011, which are derived by combining repeat cycles 11 to 363 from TOPEX/Poseidon, 21 to 259 from Jason-1 and 21 to 111 from Jason-2 respectively, so as to produce a continuous 18.5 year time series.

Due to the lack of a well defined geoid, the mean sea surface derived from a combination of eight satellite missions was subtracted from the data set. In addition the 18.5-year mean was subtracted from each measurement so as to produce its time variable, sea surface height anomaly.

2.2.2 General Circulation Models

Even though satellite altimetry provides an ideal set for the study of the mesoscale from the observational point of view, general circulation models can be used complementary to it in order to deepen our understanding on the scientific goals described in Chapter 1. Models are free of several inadequacies which follow the observations even after corrections are applied, such as residual tides and noise. In the following sections two gcms with different characteristics, STORM (global) and MITgcm (regional), will be introduced.

2.2.2.1 STORM

For comparison, I use the results of a high resolution global model STORM. The STORM experiment consists of atmosphere and ocean model components that are based on the latest version of the well proven ECHAM atmosphere model and the MPIOM ocean model. The mean horizontal resolution of the atmosphere model is approximately $40\,km$ (768×384 grid cells on a Gaussian Grid). With vertically 199 model levels, the computational grid has a total size of 59 Mio points. To simulate mesoscale ocean eddies properly, the ocean model component MPIOM TP6M, uses a setup with a horizontal grid spacing of $10\,km$, yielding 3602×2394 grid cells per layer, and vertically 80 model layers, the model equations need to be solved for a total of 690 Mio grid cells. A curvilinear tripolar grid was chosen to achieve an almost evenly spaced ocean grid. Within the experiment the Earth system models used are ECHAM6-JSBACH/MPIOM (COSMOS framework), the Model Components used are ECHAM6, representing the atmosphere, MPIOM, representing the ocean and sea ice, JSBACH, representing the land surface and vegetation. The Earth system modeling tools used are OASIS3 coupler. Further information on the STORM simulation can be found in von Storch et al. [2012b]. "The model was spun up for 25 years using the OMIP forcing derived from the ERA15 re-analysis, consisting of a climatological mean forcing plus a daily forcing that describes synoptic variations in year 1982 and is repeatedly applied, after the 25-year spin-up phase, the kinetic energy in the deep ocean reaches a quasi-equilibrium state,the forcing was then switched to the 6 hourly NCEP/NCAR

reanalysis-1 [Kalnay et al., 1996] for the period 1948 to 2010" [von Storch et al., 2012a].

Both the annual and monthly output of sea surface height will be used and the EKE field derived from SSH provided from the STORM experiment forced by NCEP/NCAR reanalysis-1 [Kalnay et al., 1996] for the time period of 1981 to 2010, regridded on a regular grid with resolution of $1/10\,°$. In addition the last 15 years of the spin-up phase are used to investigate ocean internal processes.

2.2.2.2 MITgcm

Complementary to altimetry I use MIT general circulation model results [Marshall et al., 1997] covering the Atlantic north of $30\,°$S up to $70\,°$N and for four different resolutions of $32\,km$, $16\,km$ $8\,km$ and $4\,km$. The model is set up on a bipolar curvilinear grid, with one pole located over North America and the other over Europe. In the vertical, the model utilizes 50 levels of varying depth from $10\,m$ in the upper ocean to $550\,m$ in the deep ocean, while bottom topography was derived by ETOPO2. The initial settings of the model are that it is at rest, with annual mean temperature and salinity from WOCE Global Hydrographic Climatology [Gouretski and Koltermann, 2004]. "The model is forced at the surface by fluxes of momentum, heat and freshwater computed using bulk formulae and the 1948-2008 6-hourly atmospheric state from the NCEP RA1 reanalysis. At the open southern boundary, the model is forced by a $1\,°$ resolution global solution of the MITgcm forced by the same NCEP data set. A barotropic net inflow of $0.9\,Sv$ into the Arctic is prescribed at Bering Strait, the model northern open boundary, which balances a corresponding outflow through the southern boundary. The model sea surface temperature is weakly relaxed to the 1948–2008 monthly ERSST V3 database [Smith et al., 2008] and the model sea surface salinity to the WOA2005 monthly climatology [Boyer et al., 2005]. The vertical mixing parametrization uses the KPP formulation by Large et al. [1994]. Background coefficients of vertical diffusion and viscosity are both $10^{-5}\,m^2s^{-1}$. Horizontally, biharmonic diffusion and viscosity represent unresolved eddy mixing. Coefficients of horizontal diffusion and viscosity are both $1 \times 10^{11}\,m^4s^{-1}$. The model further incorporates a dynamic thermodynamic sea ice model [Zhang and Rothrock, 2000] and solves for anthropogenic tracers. An annual averaged river run-off is applied. The model was integrated forward for $122\,yr$, that is, forced twice by the NCEP 1948-2008 data set. The first 61-yr run was disregarded since its first $20\,yr$ were contaminated by adjustment from the climatological initial condition. The second period of 61-yr started from the velocity and density fields reached at the end of the first run. In the period after 1970, all analysed quantities were seen to

agree between both runs, implying a good degree of model spin-up" [Serra et al., 2010]. I use monthly data, spanning from 1955 to 2010 for resolutions $8 - 32\,\text{km}$ and daily data for the period 2004 to 2010 for the $4\,\text{km}$ resolution. The data were interpolated first on a regular grid. In order for the frequency and wavenumber spectra computed for MITgcm to be comparable to the one derived from altimetry, I interpolated the data on to the along-track arcs.

2.2.3 Wind Velocity and Wind Stress data

For the computation of wind stress the wind at $10\,\text{m}$ above sea surface was used, provided by NCEP/NCAR reanalysis-1 [Kalnay et al., 1996] for the period 1948 to 2009. The wind stress is computed following the approach described in Smith [1988]. The winds vary sharply in speed and direction throughout the atmospheric Ekman layer, at a solid boundary the wind speed must be zero just at the surface; so the wind and water velocities must match just at the boundary [Apel, 1987]. The stress is the aerodynamic force per unit area exerted by the wind on the sea surface, given by:

$$\tau = c_d \rho_\alpha |\mathbf{u}_w| \mathbf{u}_w \tag{2.1}$$

where $\mathbf{u}_w$ is the wind velocity, ρ_α the air density and c_d the aerodynamic drag coefficient, which is a function of wind speed. The drag coefficient in neutral stratification can be obtained by:

$$c_d = [K/\ln(z/z_0)]^2 \tag{2.2}$$

where $K = 0.4$ is the von Karman constant [Smith, 1988].

2.3 Methodology

2.3.1 Eddy Kinetic Energy

The Eddy Kinetic Energy (EKE) can be estimated from along-track SSH anomaly data following the methodology described in Stammer [1997a]. Assuming geostrophic balance and isotropic conditions from the along-track SSH anomalies we can compute EKE following the equation:

$$EKE = \langle v_s^2 \rangle \tag{2.3}$$

where

$$v_s = -\frac{g}{f}\frac{\partial \zeta}{\partial l} \tag{2.4}$$

is the surface geostrophic velocity component normal to the local track orientation and ζ and l the along-track SSH anomaly and northward coordinate respectively. All altimetry derived distributions are plotted on a $2° \times 2°$ geographical grid, otherwise it will be explicitly specified.

On the other hand with the use of STORM monthly output of SSH, after removing the same 18 year (1993–2010) mean in order to produce SSH anomaly in correspondence with the respective product from altimetry, EKE can be derived from the gridded data following the equation:

$$EKE = \frac{1}{2}\left(\left(\frac{g}{f}\frac{dSSH}{dx}\right)^2 + \left(-\frac{g}{f}\frac{dSSH}{dy}\right)^2\right) \tag{2.5}$$

Eddy kinetic energy is computed from SSH anomaly for STORM so as to produce the geostrophic component which is available also from altimetry. Keep in mind that by subtracting the long term mean in order to produce SSH anomalies changes of the large scale circulation are included in the results.

2.3.2   Statistics

A straight forward way to identify regions of high and low energy in the world's oceans, is the distributions of SSH **root mean square** derived as:

$$SSH_{rms} = \sqrt{\frac{1}{N}\sum_{k=1}^{N} SSH_k{}^2} \tag{2.6}$$

It is already known from previous studies that the distribution of sea surface height is not Gaussian [Hughes et al., 2010; Sura, 2011; Sura and Gille, 2010; Thompson and Demirov, 2006]. To establish this non-gaussianity we compute the **kernel density** of sea surface height, a non-parametric estimate of the probability distribution function. For an independent and identically distributed (iid) random variable $x_1, x_2, ..., x_n$ with an unknown density f, the shape of this density function can be derived through its

kernel density estimator as:

$$\hat{f}_h(x) = \frac{1}{n} \sum_{i=1}^{n} K_h(x - x_i) \quad = \frac{1}{nh} \sum_{i=1}^{n} K\left(\frac{x - x_i}{h}\right) \tag{2.7}$$

where $K(\cdot)$ is the kernel – a symmetric but not necessarily positive function that integrates to one – and h>0 is a smoothing parameter called the bandwidth. The kernel function we used is normal and the bandwidth is a function of the number of points in x. After the density function is estimated, a set of theoretical distributions (Gaussian, Exponential, Logistic) is fitted.

In addition a **Lillitest** of PDFs obtained within an individual 2° × 2° gridbox with respect to normality was performed. We tested each individual time series on the satellite track using the Lillietest, by combining all results from within each 2° × 2° region, the percentage of time series that are Gauss distributed can be estimated. The Lillietest performs Lilliefors goodness-of-fit test of composite normality, when the test fails it means that the null hypothesis (the data are normally distributed), can be rejected at the 5 % level. The Lilliefors test is a 2-sided goodness-of-fit test suitable for situations where a fully-specified null distribution is not known, and its parameters must be estimated. "The Lilliefors test is a variation of the Kolmogorov-Smirnov test that accounts for the uncertainty of the estimate of the mean and variance. The Lilliefors statistics is given by:

$$D_L = max \mid \hat{F}_X(x) - F_{\mathcal{N}}^*(x) \mid , \tag{2.8}$$

where $F_{\mathcal{N}}^* \frown \mathcal{N}(\hat{\mu}_x, \hat{\sigma}_x)$ is the normal distribution in which the mean and the standard deviation are replaced with sample mean and standard deviation. D_L measures the distance between the empirical distribution function and the normal distribution fitted to the data. Large realizations of D_L indicate that the null hypothesis should be rejected" [von Storch and Zwiers, 1999].

We study sea surface height anomaly dynamics using simple statistics, namely the third and fourth statistical moments, **skewness** and **kurtosis** respectively. Skewness and kurtosis of sea surface height anomaly are also indicative of the deviation of the density distribution from the normal distribution. The higher moments were computed globally and regionally for the 18.5 year time series and seasonally, applying the following equations:

$$S = E\left[\left(\frac{X - \mu}{\sigma}\right)^3\right] \tag{2.9}$$

17

2. DATA AND METHODOLOGY

$$K = E\left[\left(\frac{X - \mu}{\sigma}\right)^4\right] - 3 \qquad (2.10)$$

where E is the expectation operator, μ is the mean, σ is the standard deviation of sea surface height anomaly and X is the sea surface height. Time series shorter than 5 months were ignored in the computations. We use the definition of 'excess' kurtosis, which we will refer to as simply kurtosis from here on, in our study since it is more extensively used and for that our results can be comparable to previous studies. The standard errors of skewness and kurtosis can be approximated as $\sigma_s = \sqrt{6/N_{in}}$ and $\sigma_k = \sqrt{24/N_{in}}$ respectively, where N_{in} is the effective number of independent observations (Sura and Gille [2010] and reference therein).

Skewness was introduced as a statistical tool, used to identify the behaviour of the wind field distribution using different satellite data as well as numerical model output [Monahan, 2006a,b, 2008], and it was observed that sea surface wind stress is highly non-Gaussian, with characteristic relationships between moments. The same methodology can be applied to sea surface height.

In order to investigate the interannual to decadal changes in EKE, the temporal trend of EKE was computed by applying **linear regression** [Emery and Thomson, 2001] at the time domain (monthly average over annual period) for each grid point fitting a model of the form:

$$y_i = \hat{y}_i + \epsilon_i \qquad (2.11)$$

where

$$\hat{y}_i = \alpha_0 + \alpha_1 x_i \qquad (2.12)$$

where α_0, α_1 are the regression coefficients and ϵ is the residual or error. The regression coefficients can be found by minimizing the sum of squared errors (SSE). SSE is the total variance that is not explained by the regression model given in **eq. 2.11** and **eq. 2.12**.

$$SSE = \sum_{i=1}^{N} \epsilon_i^2 = \sum_{i=1}^{N} (y_i - \hat{y}_i) = \sum_{i=1}^{N} [y_i - (\alpha_0 + \alpha_1 x_i)]^2 = SST - SSR \qquad (2.13)$$

in which

$$SST = \sum_{i=1}^{N} (y_i - \overline{y})^2 \quad and \quad SSR = \sum_{i=1}^{N} (\hat{y}_i - \overline{y})^2 \qquad (2.14)$$

The sum of square total (SST) is the variance in the data and the sum of squares

regression (SSR) is the amount of variance explained by the regression model. The minimization conditions are acquired by setting the partial derivatives of **eq. 2.13** with respect to α_0 and α_1 to zero. We have for α_0

$$\frac{\partial SSE}{\partial \alpha_0} = \frac{\partial}{\partial \alpha_0} \left\{ \sum_{i=1}^{N} [y_i - (\alpha_0 + \alpha_1 x_i)]^2 \right\} = -2 \sum_{i=1}^{N} [y_i - (\alpha_0 + \alpha_1 x_i)] =$$

$$-2 \left(\sum_{i=1}^{N} y_i - N\alpha_0 - \alpha_1 \sum_{i=1}^{N} x_i \right) = 0 \quad (2.15)$$

for α_1

$$\frac{\partial SSE}{\partial \alpha_1} = \frac{\partial}{\partial \alpha_1} \left\{ \sum_{i=1}^{N} [y_i - (\alpha_0 + \alpha_1 x_i)]^2 \right\} = -2 \sum_{i=1}^{N} [y_i - (\alpha_0 + \alpha_1 x_i)] =$$

$$-2 \left(\sum_{i=1}^{N} x_i y_i - \alpha_0 \sum_{i=1}^{N} x_i - \alpha_1 \sum_{i=1}^{N} x_i^2 \right) = 0 \quad (2.16)$$

These equations can be solved simultaneously in order to find an estimate of the coefficient α_1 (the slope of the regression line), this is then used to obtain an estimate of the second coefficient α_0 (the intercept of the regression line). In particular

$$\hat{\alpha_1} = \frac{\sum_{i=1}^{N} (x_i - \overline{x})(y_i - \overline{y})}{\sum_{i=1}^{N} (x_i - \overline{x})^2} = \frac{\left[N \sum_{i=1}^{N} x_i y_i - \sum_{i=1}^{N} x_i \sum_{i=1}^{N} y_i \right]}{\left[N \sum_{i=1}^{N} x_i^2 - \left(\sum_{i=1}^{N} x_i \right)^2 \right]} \quad (2.17)$$

$$\hat{\alpha_0} = \overline{y} - \hat{\alpha_1} \overline{x} \quad (2.18)$$

The global distribution of the coefficient $\hat{\alpha_1}$ was then plotted on a $2° \times 2°$ geographical grid.

Regions where the estimated slope of the regression line had less than 60% significance were shaded. To obtain the significance level the cross correlation coefficient between the original data and the fitted line was computed at zero lag following:

$$C_{xy}(\tau) = E[\{y(t) - \mu_y\}\{x(t+\tau) - \mu_x\}] = \frac{1}{N-k} \sum_{i=1}^{N-k} [y_i - \overline{y}][x_{i+k} - \overline{x}] \quad (2.19)$$

and the normalized cross correlation coefficient function for a stationary process is

$$r_{xy} = \frac{C_{xy}(\tau)}{\sigma_x \sigma_y} \tag{2.20}$$

where σ_x and σ_y is the variance of x and y respectively.

The p-value is then applied for testing the hypothesis of no correlation. Each p-value is the probability of getting a correlation as large as the observed value by random chance, when the true correlation is zero. If p is small, then the correlation r_{xy} is significant. To compute the p-value r_{xy} is transformed into a t-student distribution as:

$$t = \frac{r_{xy}\sqrt{n-2}}{\sqrt{1-r_{xy}^2}} \tag{2.21}$$

where n are the degrees of freedom and is compared to $N(0, 1/\sqrt{n})$ the asymptotic distribution of the cross-correlation.

2.3.3   Frequency and Wavenumber Spectra

The variance of a time series $X_1, X_2, ..., X_N$ of finite length may be attributed to different time scales by expanding it into a finite series of trigonometric functions, as:

$$X_t = A_0 + \sum_{k=1}^{(N-1)/2} (a_k cos\frac{2\pi kt}{N} + b_k sin\frac{2\pi kt}{N}) \tag{2.22}$$

so the variance of the time series is distributed to the periodic components in **eq. 2.22**, and given by:

$$variance = \frac{1}{2} \sum_{k=1}^{(N-1)/2} (a_k^2 + b_k^2) \tag{2.23}$$

[von Storch and Zwiers, 1999].

By definition for an ergodic weakly stationary process X_N with auto-covariance function $\gamma(\tau), \tau = 0, \pm 1, ...$, the spectrum of X_N is the Fourier transform of the auto-covariance function:

$$\Gamma(\omega) = F\{\gamma\}(\omega) = \sum_{\tau=1}^{\infty} \gamma(\tau)e^{-2\pi i\tau\omega}, \ \ for \ \ all \ \ \omega \in [-1/2, 1/2] \tag{2.24}$$

The spectrum of a real-valued process has several properties. It is symmetric, contin-

uous and differentiable everywhere within the $[-1/2, 1/2]$ interval, thus

$$\frac{d}{d\omega}\Gamma(\omega) \mid_{\omega=0} = 0 \qquad (2.25)$$

where ω represents frequency. The auto-covariance function can be reconstructed from the spectrum by using the inverse Fourier transform and the spectrum is a linear function of the auto-covariance function. In order to ensure weak stationarity, two conditions must be satisfied. First the mean of the process should be independent of time, so a random variable should have zero mean. Second, the auto-covariance function must be a function of τ alone. For ergodic weakly stationary processes variance is attributed to time scale ranges or frequency intervals [von Storch and Zwiers, 1999].

Welch introduced modifications in block averaging, arguing that using a data taper on each block reduces the potential bias due to leakage in the periodogram and showed that if the blocks overlap the resulting spectra has better variance properties [Percival and Walden, 1993]. If N_S is a block size and $h1, ..., h_{N_S}$ a data taper, given a time series with realization $X_1, X_2, ..., X_N$ of a stationary zero mean process, the spectral estimator for each block can be derived by:

$$\hat{S}_l^{(d)}(f) = \Delta t |\sum_{t=1}^{N_S} h_t X_{t+l-1} e^{-i2\pi f t \Delta t}|^2 \quad -1 \leq l \leq N + 1 - N_S \qquad (2.26)$$

The Welch's overlapped segment averaging spectral estimator is then given by:

$$\hat{S}(f) = \frac{1}{N_B} \sum_{j=0}^{N_B-1} \hat{S}_{jn+1}^{(d)}(f) \qquad (2.27)$$

where N_B is the total number of blocks to be averaged together and n is an integer-valued shift factor satisfying $0 < n \leq N_S$ and $n(N_B - 1) = N - N_S$ [Percival and Walden, 1993].

The altimeter data were interpolated in time and space, gaps that were larger than 20 days in time and larger than 30 km in space were ignored in the interpolation. The interpolated data were used to compute the frequency and wavenumber spectra using Welch's method. The data were considered as one section which was windowed using a Hamming window. Before the computation of the frequency spectra any remaining trend was removed. Hereinafter, frequency spectra were computed for every along-track position and then averaged globally or regionally.

For the computation of wavenumber spectra of SSH the methodology described

2. DATA AND METHODOLOGY

by Scharffenberg and Stammer [2011] was followed. Explicitly for latitudes between $\pm 60°$, each arc was divided into 21 segments each $10°$ of latitude. The tracks of the satellite altimeter are curved, as a consequence arc segments over the different $10°$ latitude contain a different number of measurements and represent different maximum length scales. In order to make the arc segments comparable, the length of the longest possible arc segment was chosen (from $50°$ - $60°$ latitude) as a reference, then shorter segment were zero-padded to that length. The data were consequently demeaned and de-trended. Finally, the Welch method as described above was applied to compute the wavenumber spectra for each $10° \times 10°$ geographic region and then averaged globally or regionally. The spatial distribution of wavenumber slope between different cut-off ranges was estimated by fitting a logarithmic line for each $10° \times 10°$ box.

The methodology described here will be applied in the following chapters. Any modifications or special details on methodology will be further analysed in the respective chapter where and if needed.

Chapter 3

Higher Order Statistics of Sea Surface Height

3.1 Introduction

Mesoscale circulation has been thoroughly and extensively studied in the last few decades on global as well as on regional scale. However, many questions still remain unclear or unanswered, some of them are addressed in a review by Ferrari and Wunsch [2009]. Probability Density Functions (PDF) which provide a basic statistical description of turbulent flow fields can be used to infer information about mesoscale circulation features. For diagnostic and modelling purposes in the atmosphere and ocean the additional need exists for a parametrizations of the PDF of the flow field. PDFs for both sea surface height and velocities have been computed before [Gille and Llewellyn Smith, 2000; Llewellyn Smith and Gille, 1998; Thompson and Demirov, 2006] and have been shown to be non-Gaussian. The geostrophic velocity PDFs from altimetry have been previously described having Gaussian cores but non-Gaussian tails [Bracco et al., 2000; Sura and Gille, 2010]. PDFs of sea surface height are expected to show similar patterns, since "geostrophic velocities are derived by differencing SSH values, the PDFs of geostrophic velocities are expected to resemble PDFs of SSH, convolved with themselves" [Sura and Gille, 2010].

Skewness and kurtosis are statistical parameters that can be used to infer the deviation of a distribution from the Gaussian as demonstrated in recent studies. In particular skewness was used to identify the behaviour of the atmospheric wind field distribution using different satellite data as well as numerical model output [Monahan, 2006a,b, 2007, 2008]. Based on this analysis it was shown that sea surface wind stress

is highly non-Gaussian, with characteristic relationships between moments. Thompson and Demirov [2006] calculated the skewness of sea level variability for the world oceans using gridded altimeter data for the period 1993 to 2001. The cross validation with a quasi-geostrophic model led to the conclusion that sea level skewness can be used to identify the mean path of unstable ocean jets as well as regions dominated by eddies. More recently, Sura [2011] confirmed theoretically that regions of low kurtosis can be used to identify and map mixing barriers in the upper ocean, using the stochastic theory of non-Gaussian oceanic variability in an idealized zonal current. It is shown by Sura and Gille [2010] that in most parts of the world oceans kurtosis is uniformly larger than 1.5 times the squared skewness minus an adjustment constant. They investigated the possibility of predicting the probabilities of extreme sea surface height anomalies from first physical principles which may provide a useful null hypothesis for non-Gaussian sea surface height variability. A similar argument was posed by Hughes et al. [2010]. After investigating the spatial variation of the distribution of sea level and especially relative vorticity using gridded altimeter data, they concluded that meandering jets depict a characteristic pattern of skewness and kurtosis and a specific relationship between moments.

In this chapter the issue concerning the shape of sea surface height PDF is revisited using altimeter data covering the overall period from 1993 to 2010 (for further details on the data see Chap. 2 section 2.2.1). It is being investigated if the shape of the PDF can be described by a theoretical distribution. The geographical pattern of sea surface height non-gaussianity is inferred. I take the next step trying to identify physical processes that can be observed through skewness and kurtosis distributions of sea surface height. In addition, the information that can be inferred through their seasonal variations are addressed.

3.2   SSH PDFs

The global sea surface height probability density function, estimated based on a normal kernel function, is displayed in **Fig. 3.1**. As SSH anomalies are being investigated the PDF is centered around zero. Included in the panel are an exponential (dotted), a logistic (dash-dotted) as well as a Gaussian distribution fit (dashed) to the PDF, suggesting that on global average a Gaussian distribution can not explicitly describe the sea surface height PDF. The latter is narrower and more peaked relative to the fitted normal distribution. The exponential distribution fit appears to be in better agreement for the core of the SSH distribution while the tails are closer to the Gaussian rather
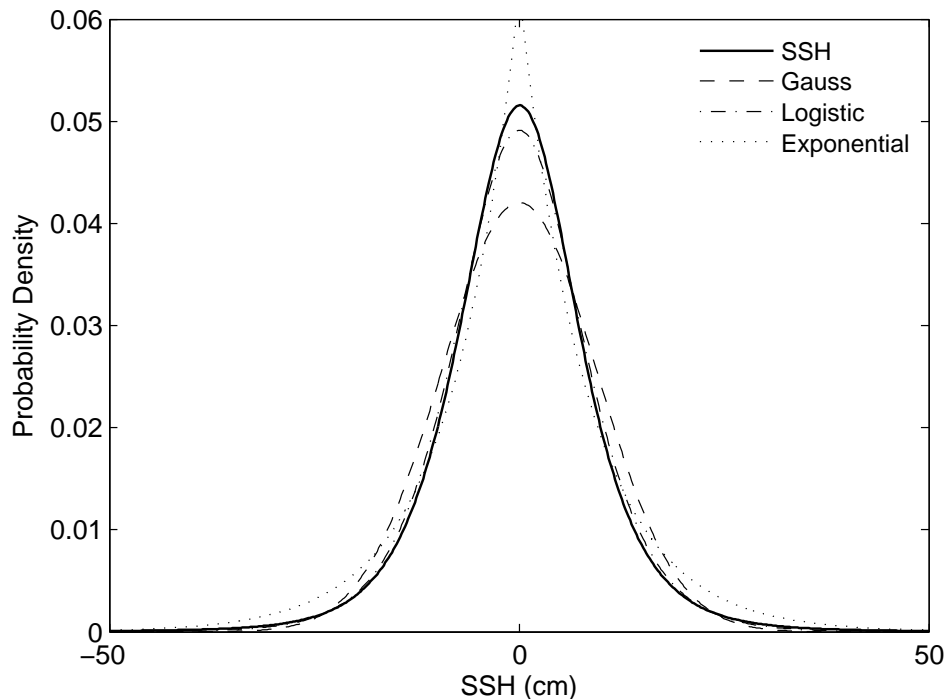
Figure 3.1: Sea surface height kernel density function. The theoretical distributions Gaussian, Exponential and Logistic are overlaid.

then to the exponential theoretical fit. Surprisingly, the Logistic distribution seems to fit the sea surface height PDF extremely well. The Logistic probability distribution is hyperbolic with zero skewness, kurtosis equal to 6/5 and is given by:

$$f(x; \mu, s) = \frac{e^{-(x-\mu)/s}}{s \left(1 + e^{-(x-\mu)/s}\right)^2} = \frac{1}{4\,s}\ \text{sech}^2\left(\frac{x-\mu}{2\,s}\right), \quad s^2 = \frac{3}{\pi^2}\sigma^2 \qquad (3.1)$$

where μ is the mean and s is a positive scale factor related to the variance as described in **eq. 3.1**. To generalize the inconsistency of the PDF with a Gaussian shape a Lillietest is performed. The Lillietest evaluates whether a time-series is Gaussian distributed or not. I start by testing each individual time series on the satellite track. The time series have not been normalized by their standard deviation before using the Lillietest. The global distribution of the Lillietest is shown in **Fig. 3.2** as percentage, i.e. at 0 % the distribution is not Gaussian and at 100 % it is Gaussian. As it can be seen the test rejects the null-hypothesis (the distribution comes from a distribution in
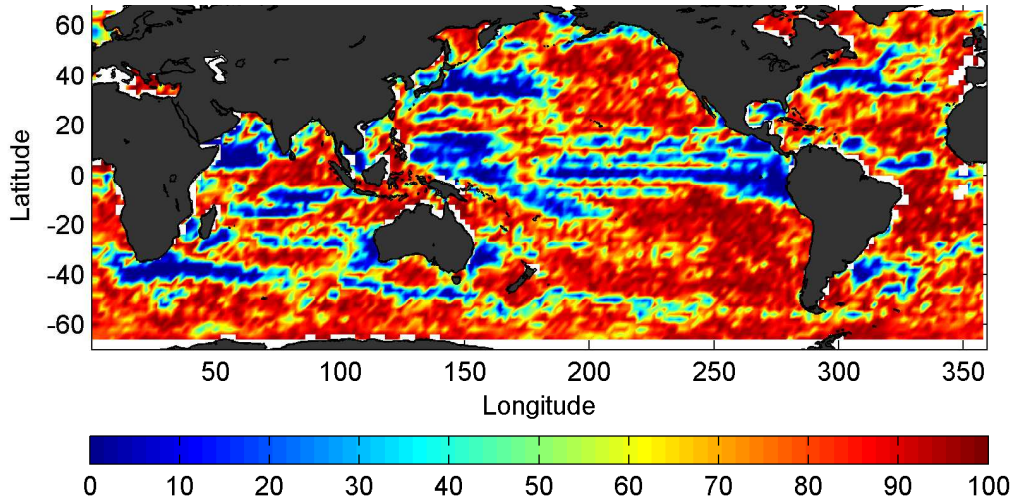
Figure 3.2: Lillietest applied to Sea surface height in %.

the normal family) in the vicinity of high energetic regions and boundary currents. In more detail, these regions are the Gulf Stream, the Kuroshio, the Agulhas retroflection, the Brazil-Malvinas confluence, the Somali current, the east Australia current and extended filaments of the Antarctic Circumpolar Current (ACC) which are characterized by non-normality. The regions where non-normality is acquainted can be associated with more frequent extreme events that enhance the tails of a PDF and rendering it more peaked. The deviation from the Gaussian in regard to velocity PDFs was attributed to inhomogeneities in the ocean by Llewellyn Smith and Gille [1998]. Spatial inhomogeneities, as an essential part of ocean mesoscale turbulent flow in the ocean, are due to mechanisms such as baroclinic instability that lead to regions of strong variability [Llewellyn Smith and Gille, 1998]. In addition, previous studies have indicated that the distribution in western boundary current regions is more appropriately described by bimodal patterns of variability, e.g. Sura and Gille [2010] and reference therein. The latter showed (their Fig. 7) that the distributions of SSH at the Kuroshio, the Gulf Stream, the Agulhas and the Loop current follow bimodal PDFs.

3.3 Skewness and Kurtosis

The ocean is characterised by motions constrained by rapid rotation and strong stratification. Zonal jets are the result of an interplay between the inverse energy cascade in

the barotropic mode and the planetary potential vorticity gradient [Vallis, 2006]. When the inverse cascade is nearly arrested meridionally by angular momentum constraints but proceeds in the zonal direction, results in oblongated eddies and eventually in alternating jets [Ferrari and Wunsch, 2009]. Skewness distribution of SSH can provide a statistical tool for identifying meandering jets, frontal areas and regions of changing variability in the global ocean [Thompson and Demirov, 2006].

The basic principle of the application of this tool is that "sea level distribution is skewed in regions populated by intense eddies with the same sense of rotation. When one of the eddies sits over a fixed location it will cause an anomalously large change in sea level, negative skewness for cyclonic eddies and positive skewness for anticyclonic eddies" [Thompson and Demirov, 2006]. A description of the pattern of skewness and kurtosis following stochastic theory is also given by Hughes et al. [2010] stating that "if a jet meanders then sea level within the region which it meanders will always be at one of two values. Along some line the jet will spend equal amounts of time to the left and to the right of that line, there kurtosis takes its minimum value. Off the line the fraction of time spent in each state varies becoming more asymmetrical with distance from the center line until beyond the limit of the meander where sea level becomes constant". The non-Gaussianity of the distribution of sea surface height anomaly can shed light into physical processes that take place in the ocean [Sura and Gille, 2010].

Skewness by definition is a measure of the asymmetry of a probability distribution; if it is zero the distribution is symmetric, when it is positive the distribution is said to be positively skewed or skewed to the right and when it is negative the distribution is said to be negatively skewed or skewed to the left [von Storch and Zwiers, 1999]. By definition a Gaussian distribution is symmetric and thus has zero skewness.

The skewness of SSH anomaly (**Fig. 3.3**) forms a dipole in regions that correspond to meandering jets and regions where oceanic fronts are located, with positive values poleward and negative values equatorward of the 'central axis' of the jet which is defined by zero skewness as previously described by Thompson and Demirov [2006]. Skewness depends on the proportion of time eddies appear at a certain location of interest and the shorter this time is the larger the skewness. Zero skewness can also be found in regions where on average the same number of positive and negative variations from the mean SSH are acquainted. For the Gulf Stream region anticyclonic eddies with a positive SSH signature can be found north of the central axis and cyclonic eddies with a negative SSH signature south of it, resulting in negative skewness for cyclonic eddies and positive skewness for anticyclonic eddies. Regions with positive skewness are observed in the North Atlantic ocean at the location of the Loop Current
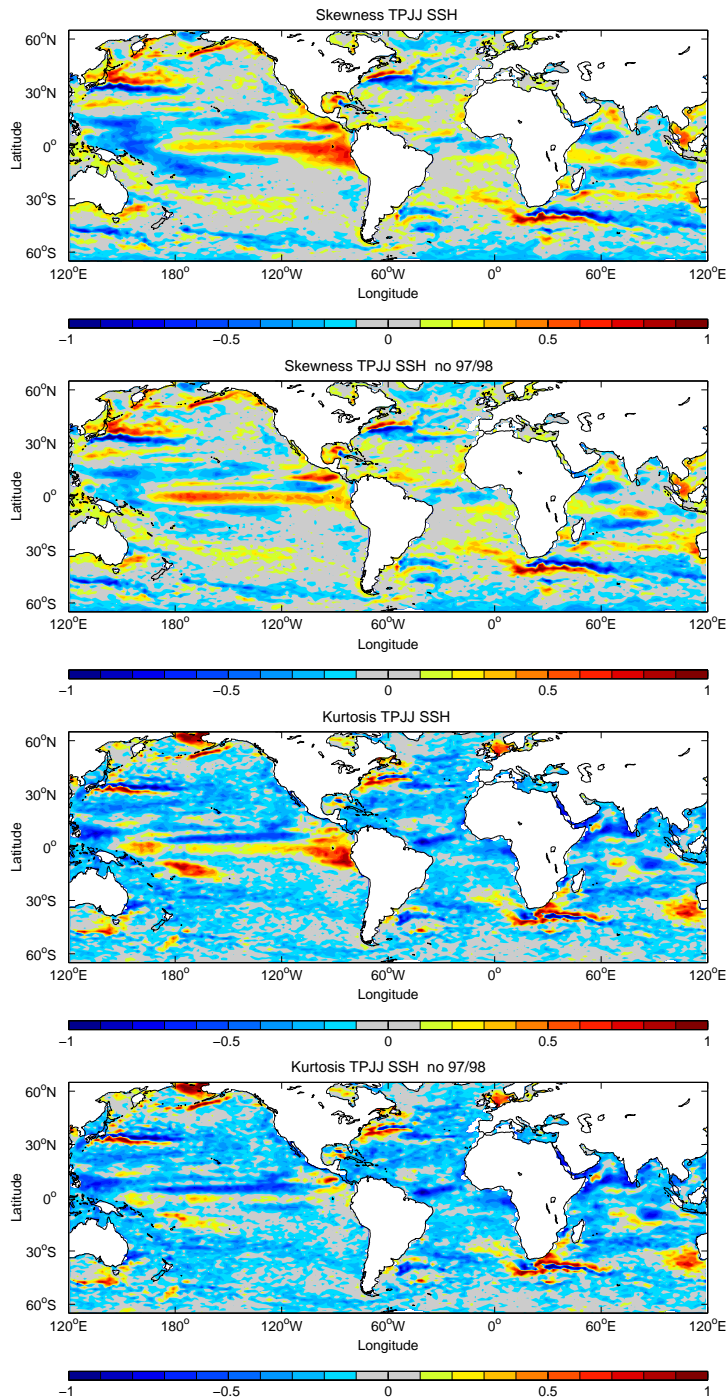
Figure 3.3: Sea Surface Height (SSH) anomaly statistics (top two) Skewness and (bottom two) Kurtosis, with and without the 1997-1998 respectively, plotted in $2° \times 1°$ grid.

and the Gulf Stream, in the Pacific ocean at the Kuroshio and in the tropical Pacific, at the East Australian current, the Agulhas retroflection and at several locations in the Indian ocean. Surprising is the approximately zero skewness at the vicinity of the Brazil–Malvinas confluence zone.

An interesting pattern in the skewness distribution is the positive 'tongue' in the tropical east Pacific, which is associated with the extreme El Niño year 1997–1998 as stated before by Thompson and Demirov [2006] and Sura and Gille [2010]. When the statistics are computed without taking into account the 1997–1998 year, as expected the equatorial Pacific region is affected, confining values of positive skewness in a narrow band at the equatorial Pacific. However, the subtraction of 1997–1998 year does not affect the distribution of skewness elsewhere.

Kurtosis on the other hand, represents the peakedness of a distribution. Platykurtic distributions have negative kurtosis and are less peaked than the normal distribution. Distributions with positive kurtosis are said to be leptokurtic and are more peaked than the normal distribution [von Storch and Zwiers, 1999]. The SSH anomaly data were filtered for outliers, since kurtosis is sensitive to the appearance of large values, which could distort its distribution. High kurtosis can be associated with the variance that lies in infrequent extreme deviations, and as shown in **Fig. 3.3** kurtosis has positive values in areas characterised by intense western boundary currents. However, as pointed out by Sura and Gille [2010] even a system with essentially Gaussian PDFs can exhibit high kurtosis if it switches over time between low and high variance conditions, hence the width of the distribution changes. Kurtosis computed ignoring the 1997–1998 year, results in mostly negative values in the equatorial Pacific. The distribution of kurtosis (**Fig. 3.3**), depicts the same general pattern described by Sura [2011], i.e. kurtosis takes minimum values along the core of a jet and increases on both sides of the current. However, the increase of kurtosis sideways of a meandering jet is not always symmetric. For example, this is the case in the Kuroshio or the Agulhas Retroflection region, as opposed to a more symmetric kurtosis distribution at the Gulf Stream/North Atlantic Current (NAC).

In previous studies [Hughes et al., 2010; Sura, 2011; Sura and Gille, 2010], an empirical relation between moments ($K \geq 1.5S^2 - 1.5$) was established and it was suggested that the non-Gaussianity of sea surface height variability can be explained through stochastic dynamics. The theoretically derived constraint $K \geq (3/2)S^2 - r$ is induced by correlated additive and multiplicative (CAM) noise, indicating the relevance of multiplicative noise in producing non-Gaussian statistics in the ocean [Sura, 2011]. The relation between skewness and kurtosis for sea surface height of 18.5 years
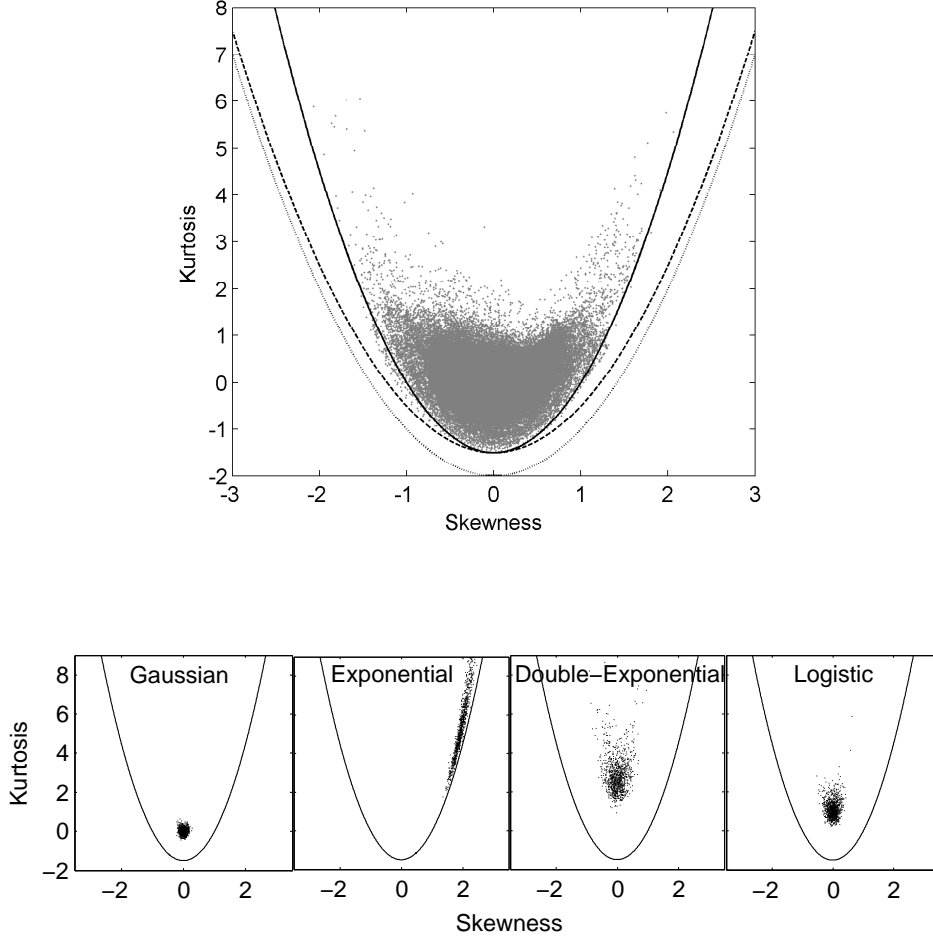
Figure 3.4: (top) SSH anomaly skewness vs kurtosis scatterplot. The dotted line indicates the theoretical lower bound for any pdf $K = S^2 - 2$, the dashed line indicates the theoretical lower bound for a unimodal pdf $K = S^2 - 1.5$ and the solid line indicates the empirical lower bound $K = 1.5S^2 - 1.5$ suggested by Sura and Gille [2010], (bottom) skewness vs. kurtosis scatterplots of theoretical distributions derived from 1000 random variables.

is shown in **Fig. 3.4** (top) which compared with **Fig. 3** in Sura and Gille [2010] is more concentrated to the center and the parabolic shape in our case is less visible. It is already known that this relation changes with latitude indicating processes which vary geographically. This structure is not consistent neither with a Gaussian nor an exponential distribution when compared with the corresponding theoretical distributions shown in the bottom panel in **Fig. 3.4**, but could potentially be derived as a

combination of different distributions.

3.4   Seasonality of SSH Moments

Skewness and kurtosis were computed seasonally, without taking into account the 1997–1998 year and having the mean seasonal velocity field overlaid (courtesy of Dr. Martin Scharffenberg). The velocity field was computed applying the parallel track approach on the 3-year long altimetry data during the tandem phase, when TOPEX/Poseidon was shifted westward to cover a new track interleaving its previous track which was continued by Jason-1, further details on the methodology can be found in Scharffenberg and Stammer [2010]. The seasonal variations of skewness and kurtosis globally are shown in **Fig. 3.5**, and **Fig. 3.6** respectively.

Regarding skewness, it can be observed that the main features of meandering jets - the formation of the dipole - is evident in the location of major currents and frontal areas throughout the year, however their intensity varies seasonally. To a first approach the seasonal variations in the global distribution of skewness and kurtosis can be indicative of the seasonality of ocean surface circulation processes, since skewness provides a measure of the amount of cyclonic and anticyclonic eddies dominating regionally and kurtosis is indicative of how frequent an event is. For example, in the equatorial Pacific, characterised by alternating bands of eastward (North Equatorial Counter Current) and westward (North and South equatorial currents) flowing currents [Philander et al., 1987], skewness is positive in the eastern section of the region during October-December, this structure extends to the west during January-March when the velocity field is in phase and tilted northwards. The pattern is dissolved during April-June and starts to reconstruct with the 'western pole' more intensified during July-September when the velocity is again in phase and tilted southwards. Positive and negative skewness in the northern and southern eastern Pacific equatorial region give rise to diverging currents. This has been reported before by Scharffenberg and Stammer [2010, see Fig. 17b] in the annually varying zonal mean geostrophic flow field anomalies, where a clear seasonal convergence/divergence on the equator was observed that led to enhanced downwelling on the equator in January-March and enhanced upwelling 6 months later.

Similar patterns (dipoles) of skewness are apparent in the North Pacific, North Atlantic oceans and the Agulhas retroflection region. In the latter the seasonal intensification of the meandering jet, the dominance of cyclonic or anticyclonic eddies can be observed through the seasonal variations of skewness. At the location of the retroflection of the Agulhas current, an eddy is released periodically into the South Atlantic
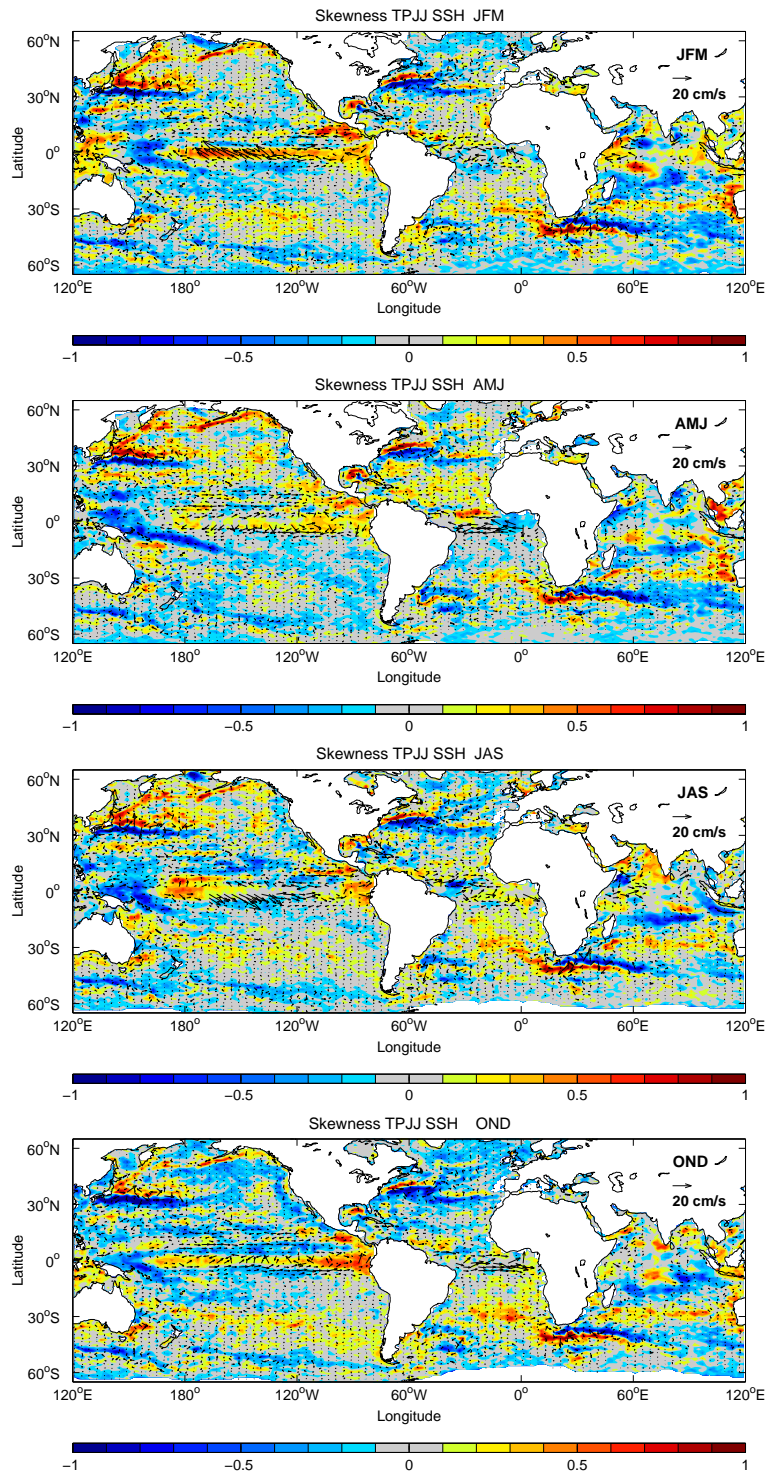
Figure 3.5: Seasonal skewness of sea surface height with mean velocity overlaid, plotted in $2° \times 1°$ grid.
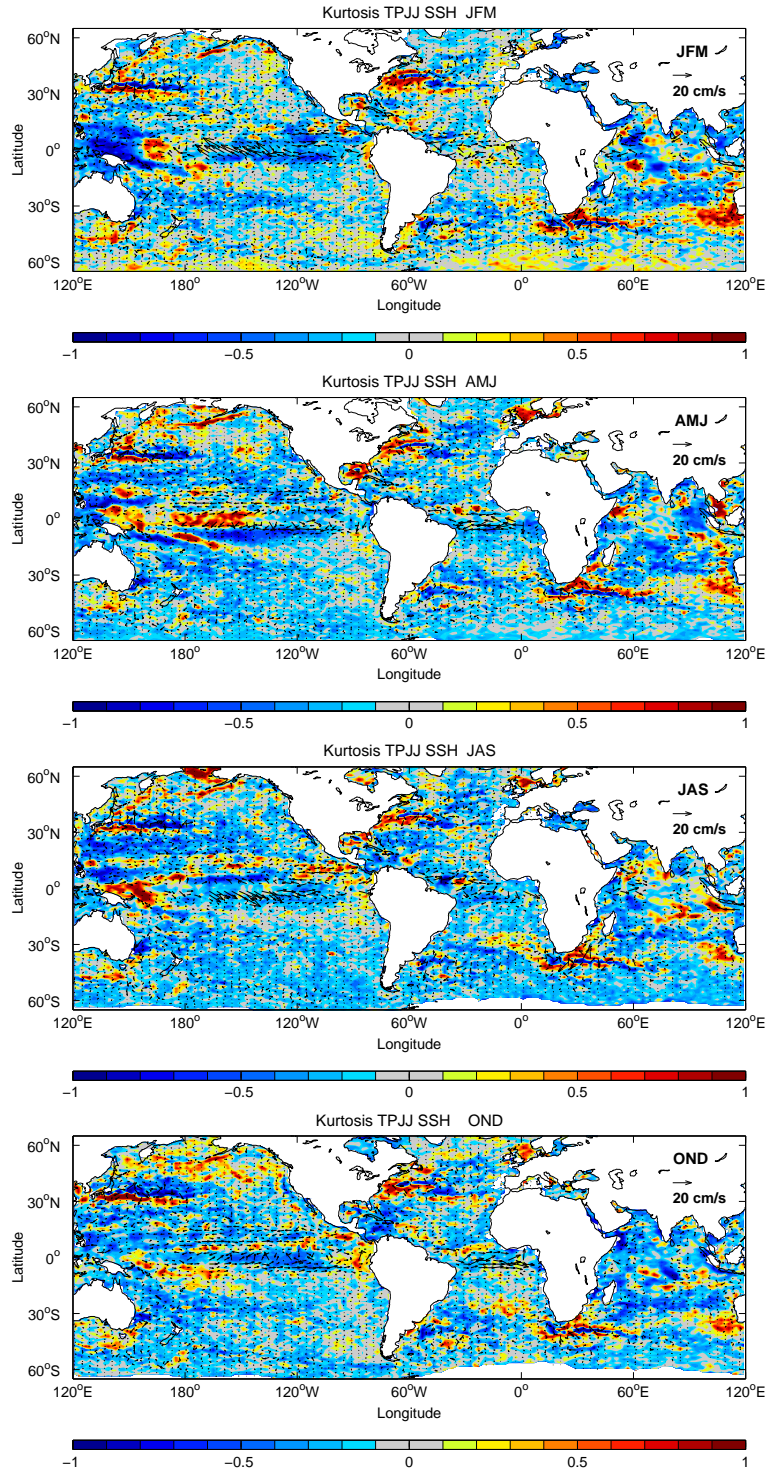
Figure 3.6: Seasonal kurtosis of sea surface height with mean velocity overlaid, plotted in $2° \times 1°$ grid.

gyre. After the eddy is released it either enters the flow of the Benguela current or is advected northwestward across the South Atlantic where it joins the South Equatorial Current, these anticyclonic warm core rings can be identified in the skewness distribution at a band between around $30\,^{\circ}$ S to $40\,^{\circ}$ S. Most intense seasonal variations of skewness are observed in the Indian Ocean, South Pacific and the Atlantic Oceans.

Kurtosis distribution also shows seasonal variations in the vicinity of large currents, where the pattern of kurtosis described above changes in (a)symmetry and/or intensity. The pattern of seasonal kurtosis distribution in the Indian Ocean is highly variable. In the southeast Indian Ocean (around $25\,^{\circ}$ S extending westward from the Australian coast) where the shallow eastward-flowing South Indian Ocean Counter Current (SICC) is situated [Jia et al., 2011] kurtosis forms a narrow band of low values which is centered around $30\,^{\circ}$ S during October-March, while during April-September shifts and extends northwards. This structure is consistent with the seasonal intensification of the local EKE which maximizes in November-January and minimizes in May-July as indicated by Jia et al. [2011]. They attribute the seasonality to baroclinic instability associated with the surface eastward-flowing SICC and the underlying westward flowing South Equatorial Current (SEC) system.

3.5 Regional Considerations

In this section the information that can be inferred through the seasonal interrelation between skewness and kurtosis focusing on high energy regions will be investigated. Regional considerations are of importance since as seen previously [e.g. Sura and Gille [2010]] the relation of skewness and kurtosis differs with latitude in the global ocean. This is also the case for the velocity PDFs in the global ocean. As Gille and Llewellyn Smith [2000] pointed out the shape of the PDFs changed with the size of the area for which they were calculated. So, small domains had Gaussian distributions while the PDFs of large areas resembled exponential distributions. Thus, keeping in mind that higher order statistics are indicative of the deviation from a Gaussian, the seasonal distribution of skewness versus kurtosis in various energetic regions of the world ocean with different characteristics are presented in the following sections.

3.5.1 Agulhas Retroflection

The first region to be investigated is the Agulhas retroflection region ($0\,^{\circ}:60\,^{\circ}$ E,$30\,^{\circ}:50\,^{\circ}$ S), where warm and saline waters originating from the Indian Ocean interact with cold and fresh waters from the Atlantic. The Agulhas region is highly energetic. Inter-ocean

exchange in this region is considered to be an important component of the global thermohaline circulation [Thompson and Demirov, 2006]. Agulhas retroflection is the only place in the ocean where cyclones and anticyclones, shed from a major western boundary current, enter the eastern part of the south Atlantic and translate long distances westward [Richardson, 2007].

Skewness is positive polewards to the core of the meandering jet which is defined by zero skewness, and negative values appear on the equatorward side (**Fig. 3.7**, top).
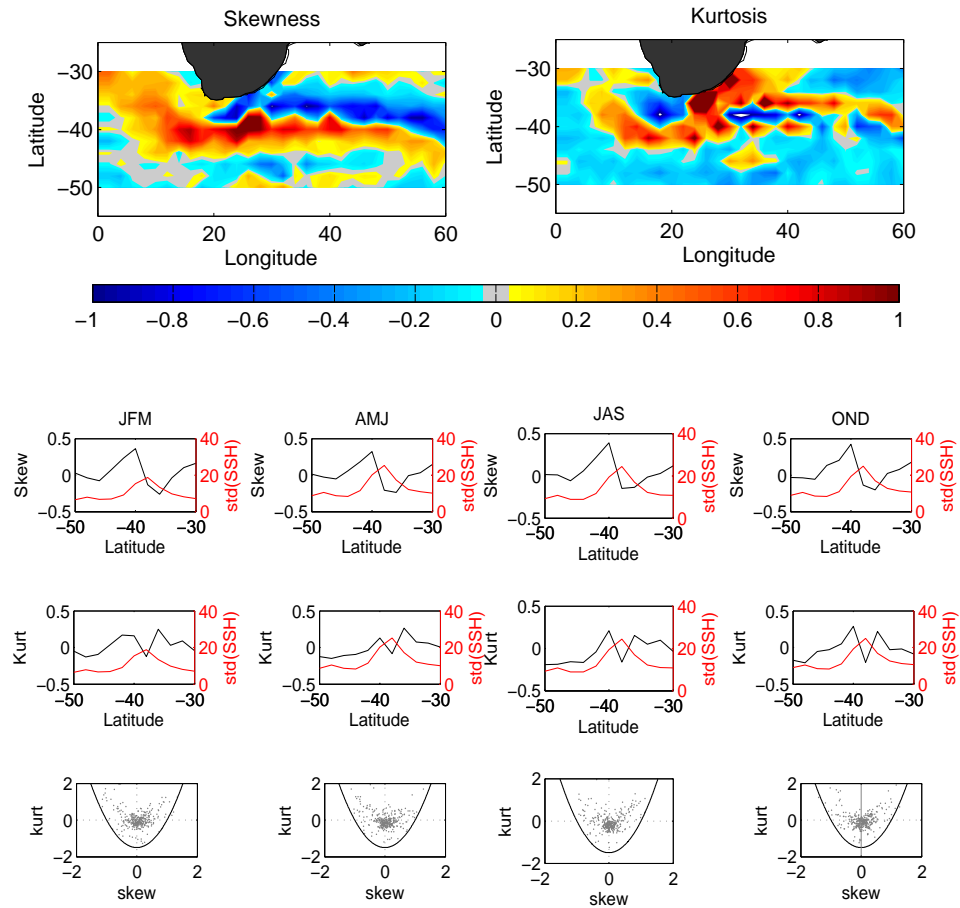
Figure 3.7: Sea surface height statistics at the Agulhas Retroflection (top) skewness and kurtosis (upper middle) seasonal skewness of sea surface height zonal averages, the standard deviation is overlaid (lower middle) seasonal kurtosis of sea surface height zonal averages, the standard deviation is overlaid (bottom) seasonal scatterplots of skewness vs kurtosis.

3. HIGHER ORDER STATISTICS OF SEA SURFACE HEIGHT

The kurtosis distribution is minimized in the center of the jet and increases on either side but not symmetrically. Positive values of kurtosis are observed in the vicinity of the western Indian ocean boundary. This general structure is also evident in **Fig. 3.7** middle panels, where the seasonal variations of skewness and kurtosis at the Agulhas region are shown as zonal averages. The SSH standard deviation (STD) is plotted complementary to the higher moments, since its maximum value signify the center of a high variable region. It can be noted that sea surface height variability is slightly weaker during January-March.

Throughout the year, skewness is asymmetrically higher at the poleward side of the jet, which means that the region is dominated by anticyclonic eddies southwards. The number of anticyclonic eddies increases during October-December when skewness is having two closely located maxima ($40\,°$S and $44\,°$S). The gradual increase of skewness from April to December could be associated partially with the time the Agulhas rings need to become more circular in shape and detach northwestward at around $41\,°$S, with an annual formation rate of 8.25 rings/year [Schouten et al., 2000]. The pattern of positive/negative skewness, towards the south Atlantic, is consistent with the observations of [Richardson, 2007] using drifters and floats. He suggests that the Agulhas current sheds large anticyclonic rings and somewhat smaller cyclones, which drift westward into the South Atlantic. The anticyclonic rings translate northwestward directly into the Benguela Current.

Kurtosis is almost slightly higher on the equatorward side of the jet during January to June and higher polewards during July to December. The seasonal asymmetry of kurtosis around the maximum sea surface height STD affects the shape of the scatter-plot of kurtosis versus skewness (S-K) (**Fig. 3.7** bottom panels). In the latter, kurtosis remains within the lower bound of $K \geq 1.5S^2 - 1.5$ imposed by stochastic theory. The larger vertical offset from the S-K bound the stronger the impact of non-local effects as indicated by Sura [2013]. The overall S-K shape does not agree explicitly with any of the theoretical shapes defined in **Fig. 3.4**. The bimodal PDF previously attributed to this regions by Sura and Gille [2010] appears to arise during October-March when S-K becomes less centered. For the October-March sub-period the center of the scatterplots is wider and rather elliptical, signifying two closely located focus points most likely related to a bimodal structure.

The seasonal scatterplots are similar to the corresponding in Hughes et al. [2010] (their Fig. 8), where they considered that there is a sharp step in sea level across the jet and random sea level variability producing a Gaussian PDF either side of the step. In their description, the resulting PDF consisted of the sum of two Gaussian PDFs with

centers separated by a certain distance. For small distance, the resulting PDF had a flatter center region than a single Gaussian. For distance greater than two the PDF became bimodal and kurtosis became smaller, dropping towards its minimum as the separation of Gaussians became larger. Their description even though is theoretical can provide a basis for estimating the seasonal variation of the width of a meandering jet. In a non-theoretical basis the PDF either side of the step are not necessarily Gaussian.

3.5.2 Pacific Ocean

For the Pacific Ocean two regions are examined, one in the equatorial Pacific ($120\,^{\circ}:270\,^{\circ}\,\mathrm{E}$, $20\,^{\circ}\,\mathrm{S}:10\,^{\circ}\,\mathrm{N}$) and the other in the North Pacific ($130\,^{\circ}:240\,^{\circ}\,\mathrm{E}$, $20\,^{\circ}:60\,^{\circ}\,\mathrm{N}$).

3.5.2.1 Equatorial Pacific

The equatorial Pacific is of interest since it is affected by climate modes, i.e. ENSO, as it is seen in **Fig. 3.3** where the statistics are computed both including the 1997–1998 year and without. The exclusion of the intense El Niño year changes the pattern of the equatorial Pacific, except for the western section of the examined region where the effect of the monsoons is more prominent. The pattern seen in the SSH skewness/kurtosis distribution is consistent with the description by Reverdin et al. [1994] for the equatorial Pacific. They state that "a zonal and meridional redistribution of equatorial Pacific surface water takes place on seasonal and interannual timescales. The zonally averaged equatorial divergence is concentrated in a narrow band centered on the equator and experiences a semiannual variability in phase with the local zonal wind. The average currents are largely zonal and their zonal scale is very large so that the major currents extend across most of the basin". The aforementioned narrow zonal band centered at the equator can be identified in the skewness/kurtosis distribution (**Fig. 3.8**, a). Thus, there is some indication that higher order statistics can be used locally to infer information about mixing properties.

The seasonal variations of SSH in the equatorial Pacific (**Fig. 3.8**, b) are generally skewed to the left (negative values), denoting that the region is dominated by cyclonic features. Cyclonic rotation is to be expected since the largest part of the considered region is located in the southern hemisphere. The seasonal variations of the north equatorial countercurrent (NECC) (around $8\,^{\circ}\,\mathrm{N}$) are captured in the distribution of skewness and kurtosis of this region. The strength of the anticyclonic circulation at the NECC is characterised by positive skewness during October to March accompanied by low values of kurtosis. During April to September the features of the south equatorial
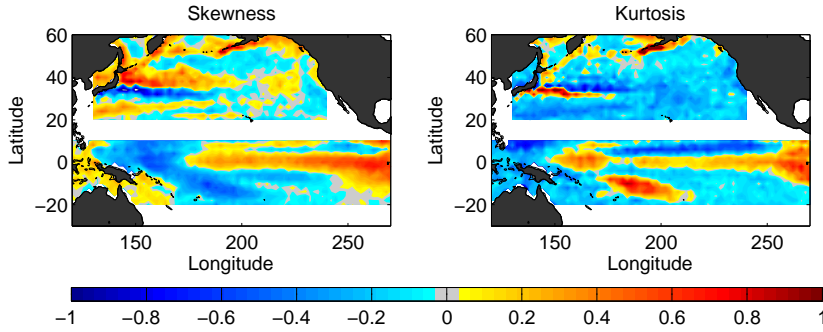
(a) skewness and kurtosis
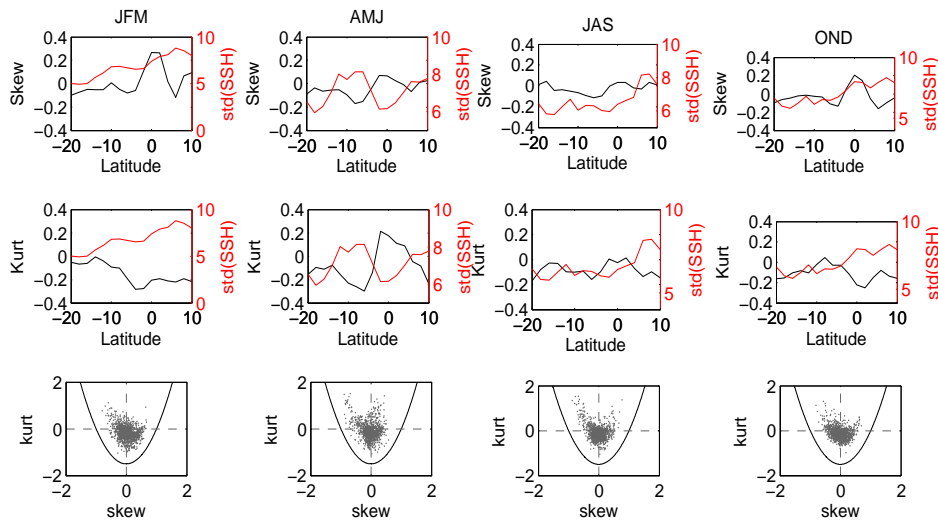
(b) 120°:270°E,-20°:10°N
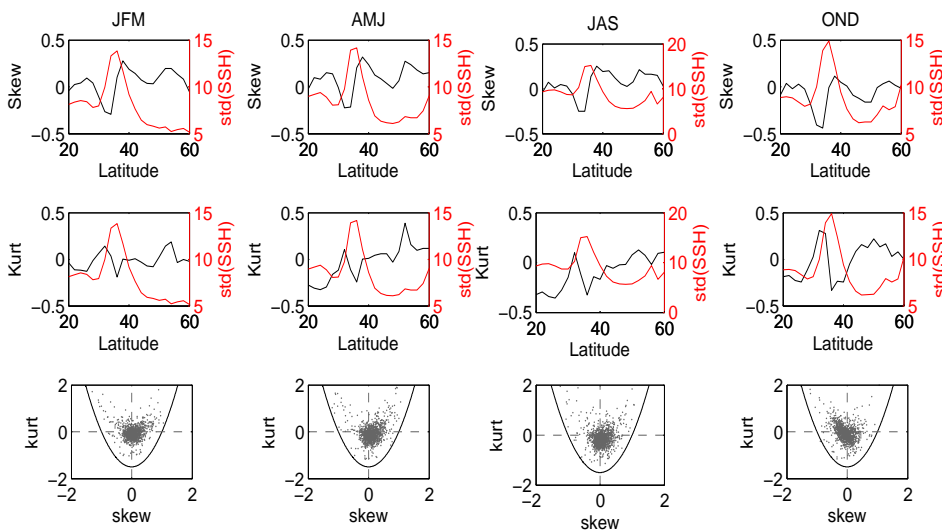
(c) 130°:240°E,20°:60°N

Figure 3.8: Same as **Fig. 3.7** but for the Pacific.

current (SEC) (around 8 °S) dominate the statistics. The presented results are consistent with the seasonal cycle of the Pacific region described by Reverdin et al. [1994], where January had the strongest NECC, while in April NECC was weakest. In April, the strongest eastward south equatorial countercurrent (SECC) was also observed.

Scharffenberg and Stammer [2010] found enhanced seasonal changes of the meridional velocity component at the eastern Pacific upwelling region of the Equatorial Undercurrent (EUC), feeding the South Equatorial Current (SEC). Their findings can be associated with positive skewness distribution in the same location in the current results. They also found seasonal changes in the western Pacific, at the Halmahera Eddy north of New Guinea. The maximum of skewness from October to March is consistent with the maximum of eastward velocity of the NECC, found in November [Scharffenberg and Stammer, 2010]. The kurtosis minimum at 6 °S during April-September coincides with the maximum upwelling at the Peruvian coast (August-September) responding to the maximum southwesterly winds in June [Scharffenberg and Stammer, 2010].

The distribution of the equatorial Pacific closely resembles a double-exponential from January to June. A more parabolic shape as described by Hughes et al. [2010]; Sura and Gille [2010] appears during July-September, and during October-December the distributions resemble a combination of Logistic and exponential.

3.5.2.2   North Pacific – Kuroshio

The northern Pacific surface currents are dominated by an anticyclonic gyre. The North Equatorial Current (NEC), is driven to the west along 15 °N under the effect of the trade winds. The NEC turns to the north to become the Kuroshio Current. At 45 °N the Kuroshio current turns eastward and in the eastern part of the basin it separates into a northward part that becomes the Alaska Current, while the other part turns southward to meet the NEC.

The distribution of skewness and kurtosis (**Fig. 3.8c**) in the North Pacific highly resembles the Kuroshio current. It is strongest from July to December, during which the standard deviation of SSH is higher. Kurtosis always reaches its minimum at the center of the jet around 36 °N, however it does not increase symmetrically around the center, taking higher values at the equatorward side. This asymmetry differs seasonally, being mostly asymmetric during October-December. The skewness is also asymmetrically distributed around the center of the jet signified by zero skewness, at the maximum of sea surface height STD. In October-December and January-March the negative section of the dipole pattern is intensified, the opposite is true in April-June, while symmetry

is accomplished in July-September. The asymmetry translates into the number of cyclonic (negative skewness) or anticyclonic (positive skewness) eddies that contribute to the formation of the dipole associated with a meandering jet.

The seasonal transport variations, maximized in July and August [Qiu, 1992] coincide with the strongest asymmetry in skewness and kurtosis from July-September. The seasonal pattern described above, is also represented in the changes visible in the S-K panels, which are close to a combination of Gaussian distributions in January-March and July-December, while during April-June resembles a combination of Gaussian and exponential distribution. Finally during October-December the distribution is highly shifted towards positive skewness/kurtosis.

3.5.3 North Atlantic

In the North Atlantic $(270\,°:330\,°\,\mathrm{E}, 20\,°:60\,°\,\mathrm{N})$, the distribution of skewness forms an asymmetric dipole in the Gulf stream/North Atlantic Current (NAC) with anticyclonic eddies northward and cyclonic eddies southward from the center of the jet (**Fig. 3.9**, top). As noted in Sura [2011] the asymmetry is due to the fact that on average, there are more cyclonic than anticyclonic eddies present in the Gulf stream. The negative skewness (cyclonic) section is more pronounced throughout the year apart from April-June when the anticyclonic section of the dipole prevails.

From the seasonal variations of the standard deviation of SSH, it can be noted that the jet has a maximum in July-September and a minimum in January-March, in agreement with Scharffenberg and Stammer [2010] (their Fig. 9). This observation is in disagreement regarding the occurrence of the maximum with Fu et al. [1987] that indicated that the Gulf Stream in the region off Cape Hatteras has a pronounced seasonal variability, with a maximum in April and a minimum in December.

The center of the Gulf Stream should be collocated with a minimum in the kurtosis distribution, however this is not apparent in **Fig. 3.9, lower middle**. This disagreement might be associated with the seasonal shift of the stream that is displaced to the north in October-December and to the south in April-June [Frankignoul et al., 2001, and reference therein]. Another possible explanation is the seasonal change in curvature of the Gulf Stream eastward of $310\,°\,\mathrm{E}$, where the Gulf stream is divided in several filaments. The seasonality of curvature in the Gulf Stream can be described as having a minimum curvature - straight path - in late summer, while the seasonal cycle is most pronounced upstream [Kelly et al., 1999]. The high values of kurtosis can be associated with the effect of the North Atlantic Oscillation (NAO), since there is a correlation
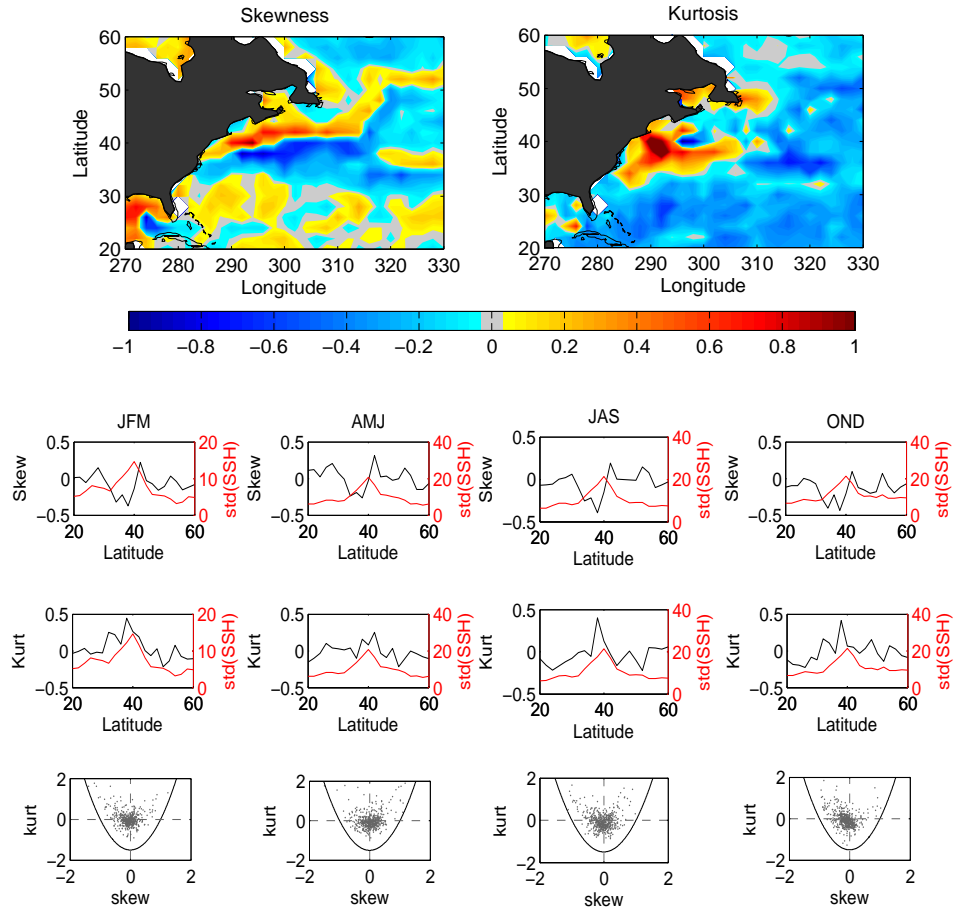
Figure 3.9: Same as **Fig. 3.7** but for the North Atlantic .

of the seasonal cycle of this region and the seasonality of NAO with a lag of one year [Frankignoul et al., 2001].

The relation of skewness and kurtosis has a parabolic shape, which indicates the non-Gaussianity of this region. The S-K is close to a Gaussian in January-March, becomes wider in April-June and more parabolic in July-September and seasonal asymmetry towards negative skewness in October-December.

3.5.4   Indian Ocean

The Indian Ocean is of interest since its surface circulation displays the largest seasonal variations due to the reversal of the monsoon [Lee and Marotzke, 1998]. The formation
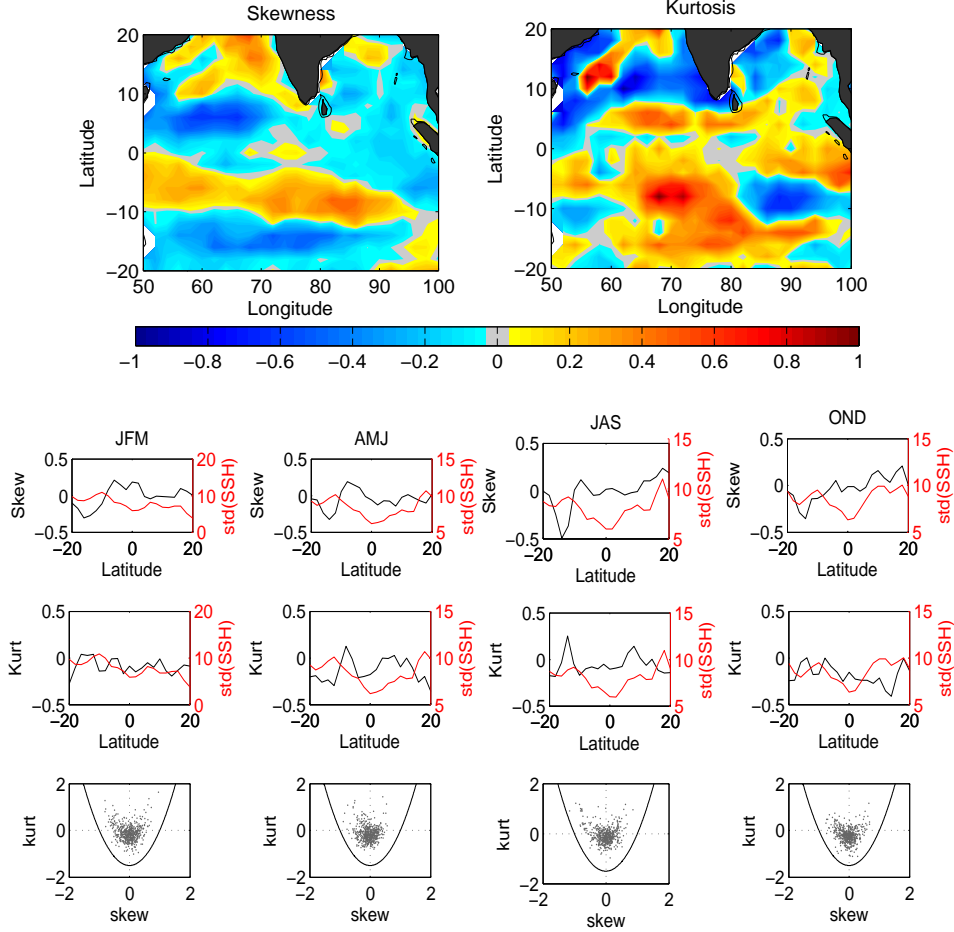
Figure 3.10: Same as **Fig. 3.7** but for the Indian Ocean.

of the dipole in the skewness distribution is observed in the north (Somali current) and south (at the convergence of the equatorial counter current and the south equatorial current) Indian Ocean (50 ° : 100 ° E, 20 ° S : 20 ° N, **Fig. 3.10** (top)), as described for other regions of interest previously. The dominant features of the Indian Ocean circulation, which were described by [Lee and Marotzke, 1998] as reproduced using a global circulation model, consist of the reversal of the surface Somali Current off the African coast and the Monsoon Current south of Sri Lanka, the semiannual equatorial jet during transition periods between the two monsoons; the North Equatorial Current and the Equatorial Counter current (ECC) during the northeast monsoon, and the South Equatorial Current that persists throughout the year. The most prominent me-

andering jet, as seen in **Fig. 3.10** middle panels, is located at $10\,^{\circ}\mathrm{S}$, its center shifts by $2\,^{\circ}$ south in April-June and in July-September, as indicated by a maximum in the standard deviation of SSH, the changing sign of skewness in either side of that maximum and the minimum in kurtosis. The seasonality of the ECC is influenced by two types of waves: non-equatorial low-latitude Rossby waves crossing the Bay of Bengal from the eastern boundary and coastal-trapped waves travelling around the perimeter of the Bay of Bengal [Schott and McCreary Jr, 2001]. The positive skewness at the zonal band between $0\,^{\circ}\mathrm{S}$ and $10\,^{\circ}\mathrm{S}$ and the negative band just southward of that, could be associated to instability mechanisms of the zonal monsoon circulation. The instability mechanisms are closely related to the generation of mixed Rossby-gravity waves in the interior of the tropical Indian Ocean [Pedlosky, 2003]. The positive values of kurtosis are not as high as seen in other regions. However, it is evident that in the larger part of the Indian Ocean extreme events are present denoted by positive kurtosis.

The seasonality of Indian ocean is displayed in the scatterplots of S-K, where the shape and the distance from the lower bound, defined by $K \geq 1.5S^2 - 1.5$, of the distributions demonstrate seasonal changes and the influence of non-local effects. During July-September, S-K is concentrated close to a Gaussian distribution. During October to June the S-K plots are centered to negative values.

3.5.5 Antarctic Circumpolar Current

The Antarctic Circumpolar Current (ACC) as reproduced in Sokolov and Rintoul [2007, 2009a] consists of multiple jets or filaments, their description is different from the traditional view where the ACC was made up of three continuous circumpolar fronts. As they state "the association between the jets and particular streamlines persists despite strong topographic and eddy–mean flow interactions, which cause the jets to merge, diverge, and fluctuate in intensity along their path. The 'meander envelopes' of the fronts are narrow on the northern slope of topographic ridges, where the sloping topography reinforces the effect, and broader over abyssal plains". This description of the ACC as a compilation of narrow, meandering jets is also suggested by Thompson [2010] using a doubly periodic, forced-dissipative, two-layer quasigeostrophic model. Sokolov and Rintoul [2009b] argue that the intensity of the SSH fronts varies with location but not with time. In this case the structure of ACC filaments can not be easily identified in the skewness distribution, since by definition the longer the time an eddy spends at a certain location the smaller the skewness. Langlais et al. [2011] using several ocean general circulation models, with resolution adequate to capture the

development of baroclinic eddies, propose a hybrid method between the one described in Sokolov and Rintoul [2007] and their own.

However, skewness and kurtosis distribution can be applied to identify instabilities along the Antarctic Circumpolar Current (ACC), and thus baroclinic eddies that are of leading-order importance in the dynamics of the ACC [Vallis, 2006]. Due to the complexity of the ACC, it is separated into three sections $((0\,^\circ:160\,^\circ\,E, 45\,^\circ:66\,^\circ\,S), (160\,^\circ:285\,^\circ\,E, 45\,^\circ:66\,^\circ\,S), (285\,^\circ:360\,^\circ\,E, 45\,^\circ:66\,^\circ\,S))$ (**Fig. 3.11**).

The distribution of sea surface height at the Indian ocean section (**Fig. 3.11**, b) is skewed to the left (negative values) throughout the year. Only in the region between $52\,^\circ\,S$ to $56\,^\circ\,S$ skewness takes values close to zero or slightly positive (during July-September). The kurtosis is positive only during January-March signifying some rare events taking place at that period. The rest of the year kurtosis is negative without any strong fluctuations. The relation between skewness and kurtosis presents the non-Gaussianity of this section of the ACC. The seasonal variations in the statistics possibly are related to the two main factors that influence the circulation at the ACC: the strong, eastward winds and the buoyancy forcing associated with the meridional gradient of atmospheric temperature and radiative effects [Vallis, 2006].

The statistics of the Pacific section (**Fig. 3.11**, c) are indicative of the existence of a distinguishable filament at $56\,^\circ\,S$, close to the Antarctic convergence $(60\,^\circ\,S)$ [Pickard, 1975]. The general characteristics of the seasonal variations in the S-K plots described for the Indian ocean section, apply here as well. However, the relation of skewness and kurtosis is more concentrated, with a more pronounced center which fluctuates seasonally, compared to that of the Indian ocean section.

The Atlantic ocean section (**Fig. 3.11**, d) statistics indicate the existence of two jet-like features at $46\,^\circ\,S$ (in the vicinity of the Antarctic convergence at $50\,^\circ\,S$ [Pickard, 1975]) and $56\,^\circ\,S$. The scatterplot of skewness versus kurtosis is indicative of the seasonal change in their relation, which in January to June is relatively centered but from July to December becomes parabolic.

In contrast to the northern and tropical regions examined in the former sections for the ACC not many conclusions about its dynamics can be derived from higher order statistics, mostly due to its complexity. The lack of continental boundaries to the north of the Southern ocean, render at the surface a grand eastward circulation.
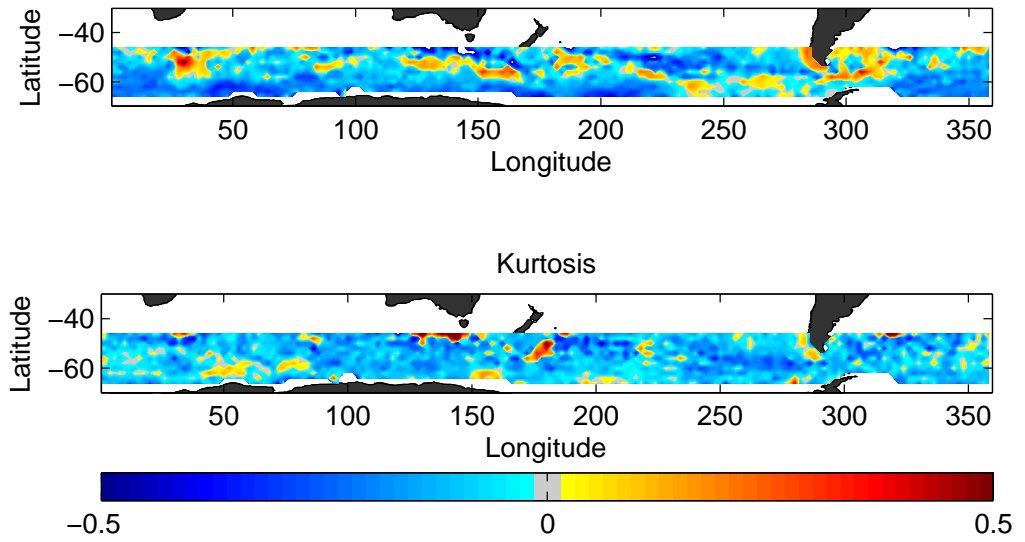
(a) skewness and kurtosis
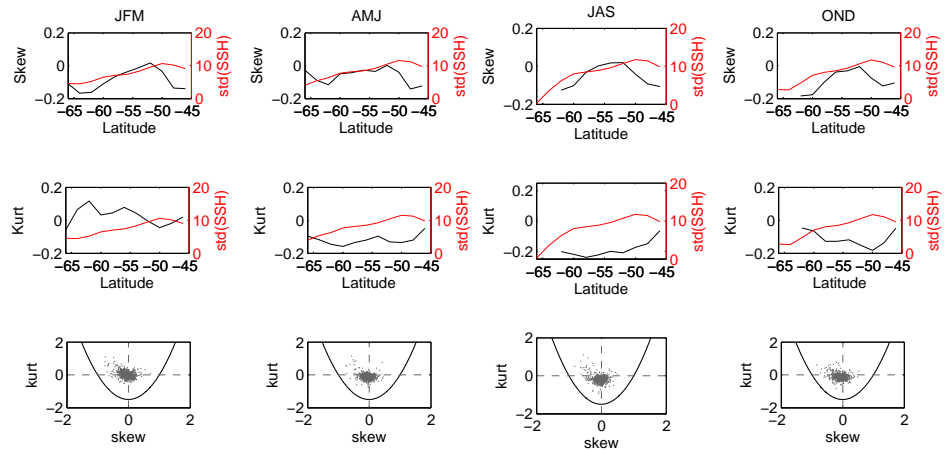
(b) $0\,^{\circ}:160\,^{\circ}$ E$,45\,^{\circ}:66\,^{\circ}$ S
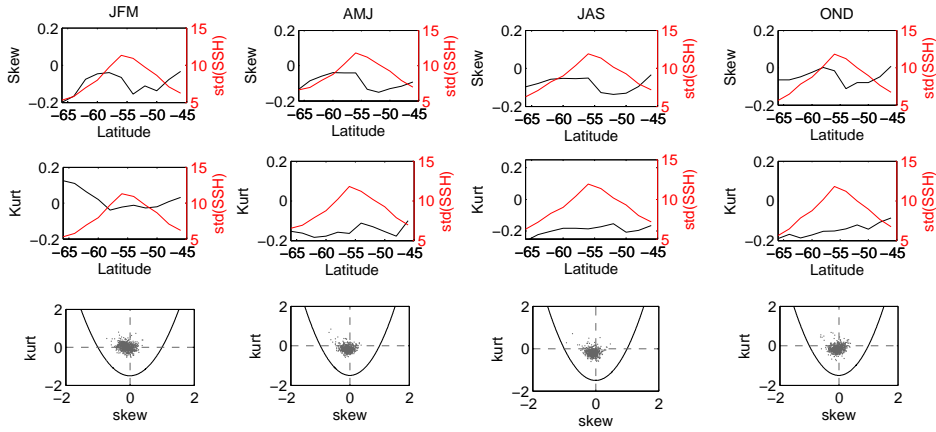
(c) $160\,^{\circ}:285\,^{\circ}$ E,$45\,^{\circ}:66\,^{\circ}$ S
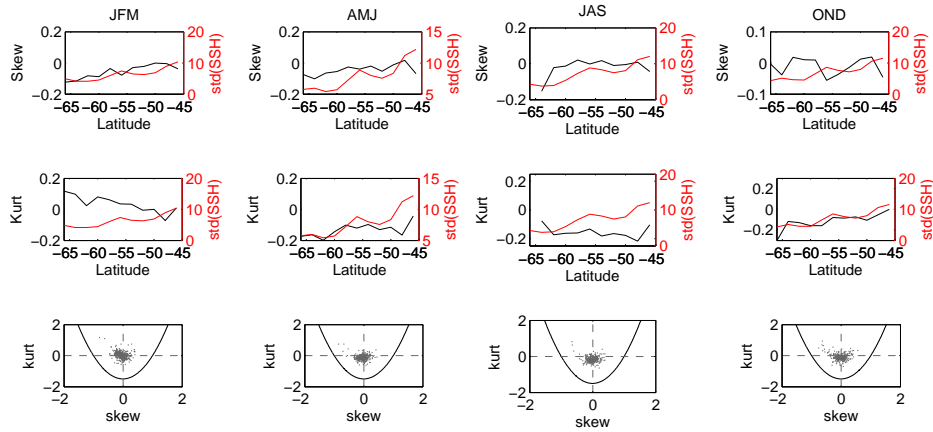
(d) $285\,^{\circ}:360\,^{\circ}$ E,$45\,^{\circ}:66\,^{\circ}$ S

Figure 3.11: Same as **Fig. 3.7** but for the ACC.

3.6   Conclusions and Discussion

A 18.5 year long data set of sea surface height anomaly from the global ocean topography experiment TOPEX/Poseidon, Jason-1 and Jason-2 satellite series was used, to investigate information about ocean dynamics derived from higher order statistics of sea surface height leading to the observed eddy variability and its changes on the seasonal cycle. To a first degree, I re-approach the question of the shape of SSH probability density function. My results, indicate that on a global average the PDF shape is best fitted by a theoretical hyperbolic Logistic distribution which can be simplified as an ensemble of Gaussian distributions. The deviation from the Gaussian on a global average applying a Lillietest appears to arise mainly from the high energetic regions of western boundary currents. The global pattern of non-normality is located in regions where extreme events are more frequent enhancing the tails of a PDF and rendering it more peaked. This pattern strengthens the idea that the deviation from normality is due to inhomogeneities in the ocean [Llewellyn Smith and Gille, 1998] due to mechanisms such as baroclinic instability.

The global distributions of higher order statistics are consistent with previous studies. The location of meandering jets can be identified by the formation of a dipole in skewness geographical distribution with positive values poleward and negative values equatorward of the ' central axis' of the jet, which is defined by zero skewness [Thompson and Demirov, 2006] accompanied with a minimum in kurtosis at the center of the jet increasing sideways.

The global relation between skewness and kurtosis of sea surface height has a structure not consistent with a Gaussian nor an exponential distribution when compared with the corresponding theoretical distributions, but could potentially be derived as a combination of different distributions. Skewness and kurtosis can be used to examine the seasonal variations of meandering jets and ocean surface circulation processes. Possibly the shedding of eddies can be observed through the seasonal variations of skewness. Kurtosis geographical distribution also shows seasonal variations in the vicinity of large currents, where the pattern of kurtosis changes in (a)symmetry and/or intensity. The relation of skewness and kurtosis differs with latitude in the global ocean as suggested previously [Gille and Llewellyn Smith, 2000; Sura and Gille, 2010] but also seasonally.

The zonal average of higher order statistics can potentially provide an estimate of the rotational regime at different latitudes and its seasonal variations. The examination of several regions of interest regarding their seasonal variation of higher order statistics led to the conclusion that skewness and kurtosis can be used to identify the main

features of the circulation at the corresponding regions and how these shift or change seasonally. However for extended regions or regions with complex circulation pattern as the Antarctic Circumpolar Current it is not easy to draw conclusions partially due to the coarse resolution of $2° \times 2°$.

As a future step, the relation of skewness and kurtosis can be used inverting the methodology described in Hughes et al. [2010] in order to infer information about the width of a meandering jet and its seasonal variations from the shape of the scatterplots.

Chapter 4

Causes for Temporal Variations of Eddy Kinetic Energy in the Ocean

4.1 Introduction

The ocean is a turbulent fluid and dominated by a vigorous mesoscale eddy field. The geostrophic eddies (ranging in spatial scales from 50 to 500 km and time scales from a few days to several months) account for a large part of the total kinetic energy of the oceans, and stir tracers and momentum in the world's oceans. Much progress has been achieved in observing and understanding the dynamics of the mesoscale eddy field during the last decades, especially with respect to the geographic distribution of eddy energy (e.g., see Fu and Le Traon [2006]; Morrow and Le Traon [2011]), and underlying dynamical principles [Fu et al., 2010; Lapeyre and Klein, 2006; Niiler et al., 2003; Tulloch and Smith, 2009; Yuan and Wang, 2010]. Satellite altimetry was essential in providing new information about the mesoscale eddy field since it is the only means to provide data with space–time coverage, sufficient to study the ocean variability, globally. Nevertheless, many questions remain open, especially regarding the generation and dissipation mechanism of eddy energy [Ferrari and Wunsch, 2009]. "Sea level, as a sensitive dynamical parameter, integrating ocean variations from the surface to the bottom, is also affected by large scale climate variability and consequently spatial and temporal variability of sea level should be expected" [Zhang and Church, 2012].

   Stammer and Wunsch [1999] investigated interannual to decadal changes in eddy kinetic energy (EKE) as a mean to unveil the sources of eddy energy in the ocean. The

4. CAUSES FOR TEMPORAL VARIATIONS OF EDDY KINETIC ENERGY IN THE OCEAN

authors concluded that the pattern of eddy kinetic energy as seen in relation to the wind stress field was globally very variable and intricate. The effect of the wind forcing in generating eddy kinetic energy in the North Atlantic was investigated again by Stammer et al. [2001] and was picked up by Fu [2007] who, based on altimetry, studied intra-seasonal variations of sea surface height in the Indian Ocean due to the wind forcing, specifically the monsoon effect. Scharffenberg and Stammer [2010] analysed the annual variations of the eddy kinetic energy globally, using altimetric sea surface height and velocity data obtained from the TOPEX-JASON-1 tandem mission, during which both satellites were flying next to each other on parallel tracks. The analysis revealed annual changes of EKE in all major current systems.

Meredith and Hogg [2006] investigated the circumpolar response of the Southern Ocean eddy activity to a change in the Southern Annular Mode (SAM). Their analysis of satellite altimeter data revealed anomalously high EKE in the Antarctic Circumpolar Current (ACC) during the period 2000-2002, which the authors associated the enhanced EKE amplitudes with the peak in the circumpolar eastward wind stress which occurred around 2-3 years earlier (1998). A corollary of this would be that together with an increase of winds over the Southern Ocean, an increased poleward heat flux associated with enhanced eddy variability may have played a significant role in the observed warming of the Southern Ocean during the last decade. This postulation was picked up by Böning et al. [2008] who investigated the response of the Antarctic Circumpolar Current to recent wind changes there. While observations show a significant intensification of the Southern Hemisphere westerlies between the latitudes of $30\,^\circ$ S and $60\,^\circ$ S, the authors did not detect an increase in the baroclinic transport of the ACC as suggested by the temporally invariant tilt of isopycnals across the ACC. This finding is in contrast to results obtained with a coarse-resolution model. The authors postulated that in the presence of a mesoscale eddy field, the transport in the ACC and meridional overturning in the Southern Ocean are insensitive to decadal changes in the wind stress, because with increasing wind stress the eddy energy, and with it the cross-frontal transport of heat would increase and would thereby lead to an eddy saturation of the frontal structure.

Studies of the energetics of the general ocean circulation [Wunsch, 1998; Wunsch and Ferrari, 2004] confirm that the circulation is mostly driven by the wind forcing. However, the extent to which wind forcing is directly responsible for the generation of eddies, and the underlying mechanisms remain an open question. Given that most of the mesoscale eddies appear to be baroclinic in nature and should then be generated through instability processes of the general circulation.

The pathway of eddy energy was addressed by Zhai et al. [2010], who used a simple reduced-gravity model along with satellite altimetry data to argue that the western boundary acts as a sink for the westward-propagating baroclinic ocean eddies. The authors estimate a convergence of eddy energy near the western boundary of approximately $0.1 - 0.3\,\mathrm{TW}$, poleward of $10\,^{\circ}$ in latitude and suggest that this energy is most probably scattered into high wavenumber vertical modes, resulting in energy dissipation and diapycnal mixing. The hypothesis remains to be confirmed, however. The full Lorenz energy cycle in the ocean was addressed recently by von Storch et al. [2012a], based on an eddy-resolving global model driven by NCEP reanalysis-1 [Kalnay et al., 1996] forcing fields. In the model, about 2/3 of rate of energy is generated by wind forcing and the rest through surface buoyancy flux. The energy exchange between reservoirs - though small - is dominated by the baroclinic pathway, converting mean available potential energy to eddy available potential energy and finally to eddy kinetic energy. The baroclinic pathway in the model is facilitated not only by the surface buoyancy flux but especially by the wind via the conversion of the mean kinetic energy to the mean available potential energy.

The goal of this chapter is to revisit the question of temporal variations of observed eddy kinetic energy in the oceans and their underlying causes. To this end, I will use the 18.5 year long altimeter time series of sea surface height data to investigate to which extent the eddy field is reacting to changes in the atmospheric forcing, notably interannual to decadal changes of the wind forcing. The study will be aided by the use of the output of the eddy resolving STORM model which was driven by the NCEP reanalysis-1 [Kalnay et al., 1996] forcing fields and which overlaps with the altimeter time series. The model results will be first compared to the observed eddy variability and will be used subsequently to interpret observed changes in kinetic eddy energy.

4.2   Time-mean Eddy Statistics

To set the stage I will first compare mean eddy statistics inferred from altimetry and simulated by the STORM model so as to identify the quality of the STORM model results. A field of the root mean square (RMS) of SSH variability (top panel of **Fig. 4.1**) representing the 18+ years of satellite altimeter data including the missions TOPEX, JASON-1 and JASON-2 (TJJ from hereafter) is overall consistent with earlier results [e.g., Fig.8a by Wunsch and Stammer, 1998]. As before, largest values of SSH variability (up to 45 cm) can be found in the vicinity of major current systems, meandering jets and frontal areas, such as the Gulf Stream, the Agulhas retroflection, the Kuroshio, the

4. CAUSES FOR TEMPORAL VARIATIONS OF EDDY KINETIC ENERGY IN THE OCEAN

Brazil currents and along the ACC. Smallest SSH variability is present in the tropical Pacific, tropical Atlantic and the southern South Ocean.

For a comparison of TJJ and STORM results, **Fig. 4.1** shows in its middle panel the difference in RMS SSH variabilities of the STORM_NCEP run minus the RMS TJJ, SSH variability, both computed for the same period. The figure reveals that over large areas, the STORM_NCEP simulation shows lower SSH variability compared to altimetry. This holds especially along the North Atlantic Current, the Agulhas, the north-equatorial currents in the Pacific and Atlantic. In contrast, and somewhat surprising, some regions show higher variability than the altimeter observations. These regions are notably the sub-polar North Pacific and the subtropical oceans. Differences in the North Atlantic result from a shift of the North Atlantic Current southward. Other areas showing differences between altimetry and STORM_NCEP include the ACC, the subtropical Pacific and Atlantic as well as the extensions of the Kuroshio and the Gulf Stream currents.

To demonstrate the amount of SSH variability originating from temporal variations in the surface forcing (as opposed to just the climatological seasonal cycle in the forcing and internal variability of the ocean), it is shown in the bottom panel of the figure the difference in RMS SSH variability as it originated from STORM_NCEP minus the climatology run STORM_C (although STORM_C and STORM_NCEP runs do not cover the same period, results seem to be insensitive on the details of the chosen period). Obviously, the STORM_NCEP run results show higher SSH variability over most parts of the ocean. However, this does not hold everywhere. In particular, the NCEP run has the North Atlantic current shifted southward. Moreover, the climatological forcing leads to more variability over parts of south of the ACC and Arabian Sea.

From the zonal averages of SSH RMS variability (**Fig. 4.2**, top) we can assess a good quantitative agreement in SSH variability between altimetry (red curve) and STORM_NCEP results (blue curve), both in terms of general variability level and regional enhancements. Both curves show enhanced amplitudes in the ACC area and a maximum around $40°$ N (Gulf Stream, Kuroshio current). Less well established in the STORM_NCEP run is the secondary maximum around $40°$ S associated with the Agulhas retroflection; also clearly under-represented in the STORM_NCEP run are the enhanced values of variability north of $50°$ N, representing SSH variability of the high-latitude Atlantic. A respective curve but from the STORM_C run (black curve) agrees essentially in its regional variations of SSH variability. However, overall the STORM_C run shows substantially smaller amplitudes of SSH variability except in the ACC area, highlighting the importance of interannual changes in the forcing fields for enhancing
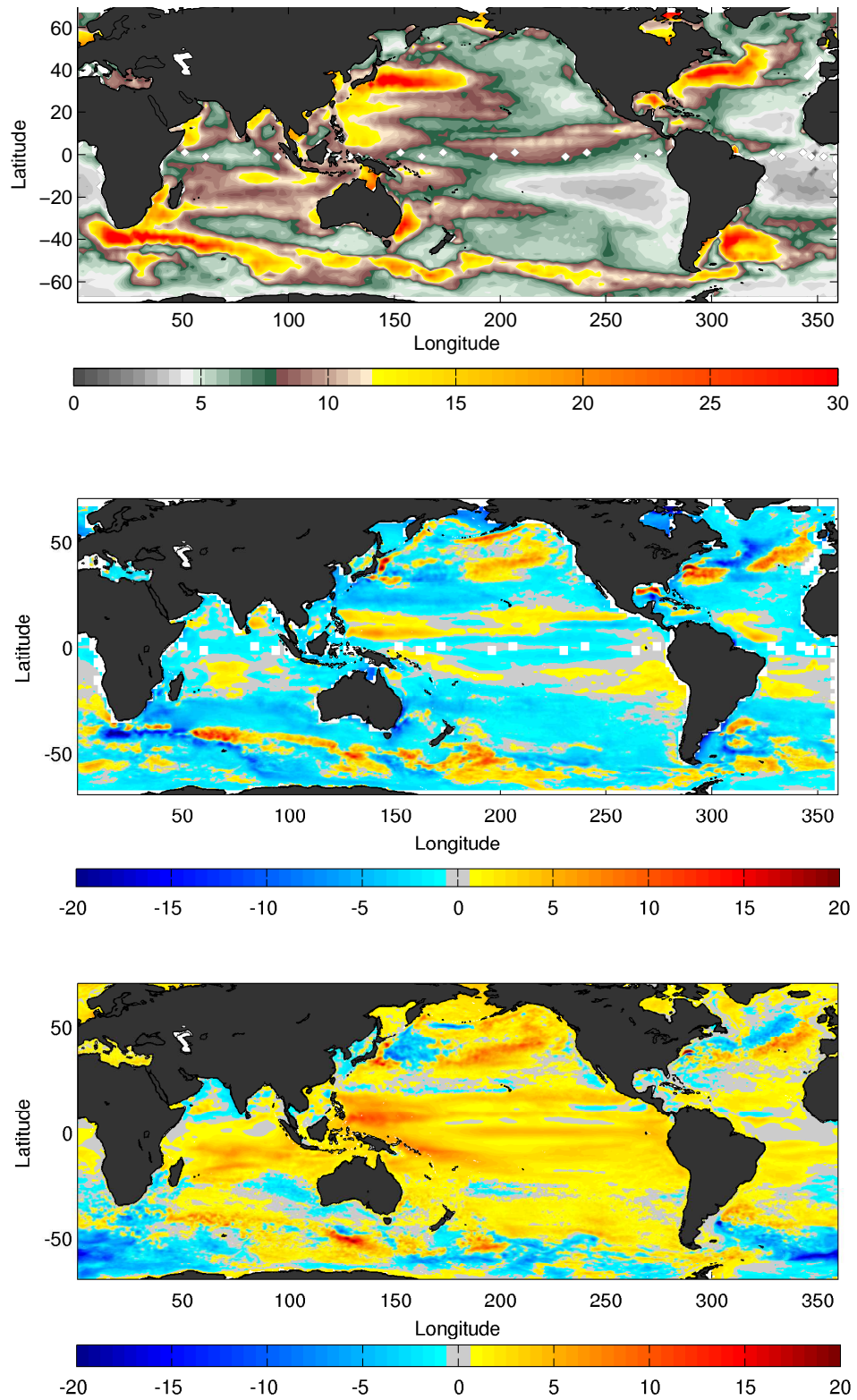
Figure 4.1: Root mean square of sea surface height anomaly in *cm* (top) from altimetry (middle) difference SSH rms STORM_NCEP minus TJJ and (bottom) difference SSH rms STORM_NCEP minus STORM_C.
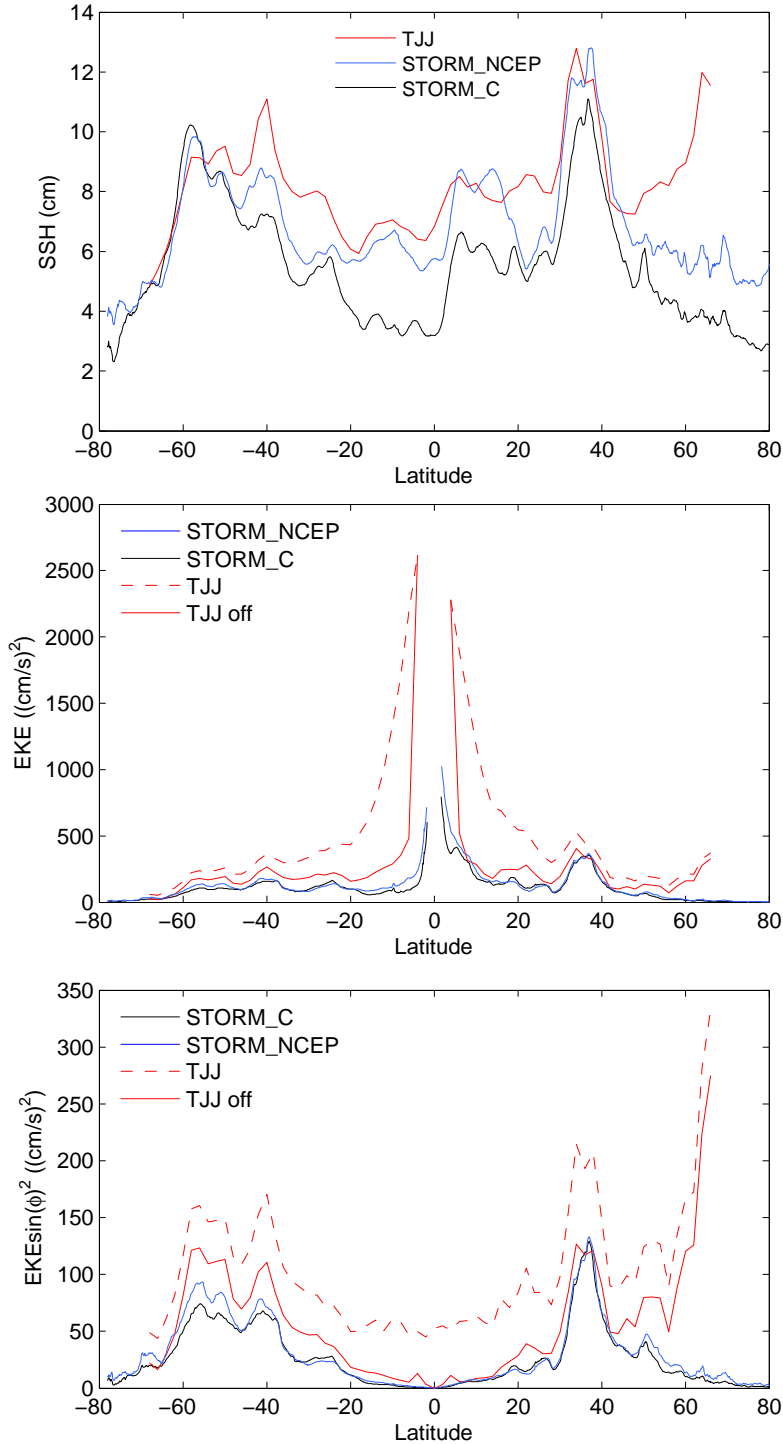
Figure 4.2: Zonal averages from TJJ , STORM_NCEP and STORM_C (top) SSH root mean square in cm (middle) EKE in $(cm/s)^2$, TJJ is off-set by $-40/sin^2(\phi)$ (bottom) EKE $sin^2(\phi)$ in $(cm/s)^2$.

eddy variability in the ocean.

Shown in the bottom panel of **Fig. 4.2** are zonal averages of $EKE \cdot \sin(\phi)^2$, essentially a slope variability not influenced by the geographical changes of the Coriolis parameter. The zonally averaged slope of EKE again reveals a good agreement between altimetry and the STORM simulation in terms of spatial variations depicting three discrete peaks at $56\,^{\circ}$S (most intense filaments of the ACC), $40\,^{\circ}$S (Agulhas Retroflection, East Australian current, Brazil-Malvinas current confluence) and $38\,^{\circ}$N (Gulf Stream, Kuroshio current) and several minor peaks at $28\,^{\circ}$S, $24\,^{\circ}$N (smaller western boundary currents, e.g. Loop current) and $50\,^{\circ}$N for example. In terms of EKE from STORM_NCEP and STORM_C, there is a surprising agreement in the slope-variability between both (much closer than the SSH variability), with STORM_NCEP showing slightly higher EKE in the southern oceans and somewhat less variability in the sub-polar northern hemisphere. This supports the hypothesis that near ocean fronts eddy variability is generated to a large extent through internal (baroclinic) instability processes.

However, the figure also reveals an overall off-set of the altimetric slope variability by about $40\,cm^2/s^2$, equivalent to an unidentified geographically uniform small-scale noise contribution in altimetric velocity estimates of $6\,cm/s$ that is not present in the model results. The extent to which this offset-is due to data noise or unresolved processes in the model is not clear. Subtracting this off-set leads to a much better overall agreement between zonally averaged EKE estimates from altimetry (solid curve) and the STORM_NCEP run. All subsequent TJJ EKE estimates will be reduced by this amount. Shown in the lower panel are resulting zonal averages of EKE values corresponding to all four curves shown in the middle panel.

Fields, similar to those shown in Fig. 4.1, but now for EKE are given in **Fig. 4.3**. In its top panel, the figure shows results from 18 years of altimetry (after a reduction by $40/sin^2(\phi)\,(cm/s)^2$). Results are consistent with recent studies from Scharffenberg and Stammer [2010] based on the three-year lasting TOPEX/JASON-1 tandem mission velocity estimates and [Stammer et al., 2006] from 11 year record of altimetric data. Both previous results also reveal less energetic regions in the North and South Pacific while the most energetic coincide with regions of major currents, such as the Gulf Stream, the Kuroshio, the Agulhas, the Brazil current and along the Antarctic Circumpolar Current (ACC).

The difference between the STORM_NCEP EKE distribution minus that from altimetry, shown in the middle panel of **Fig. 4.3**, confirms essentially the differences in eddy pattern already revealed by SSH and suggests that the model develops less
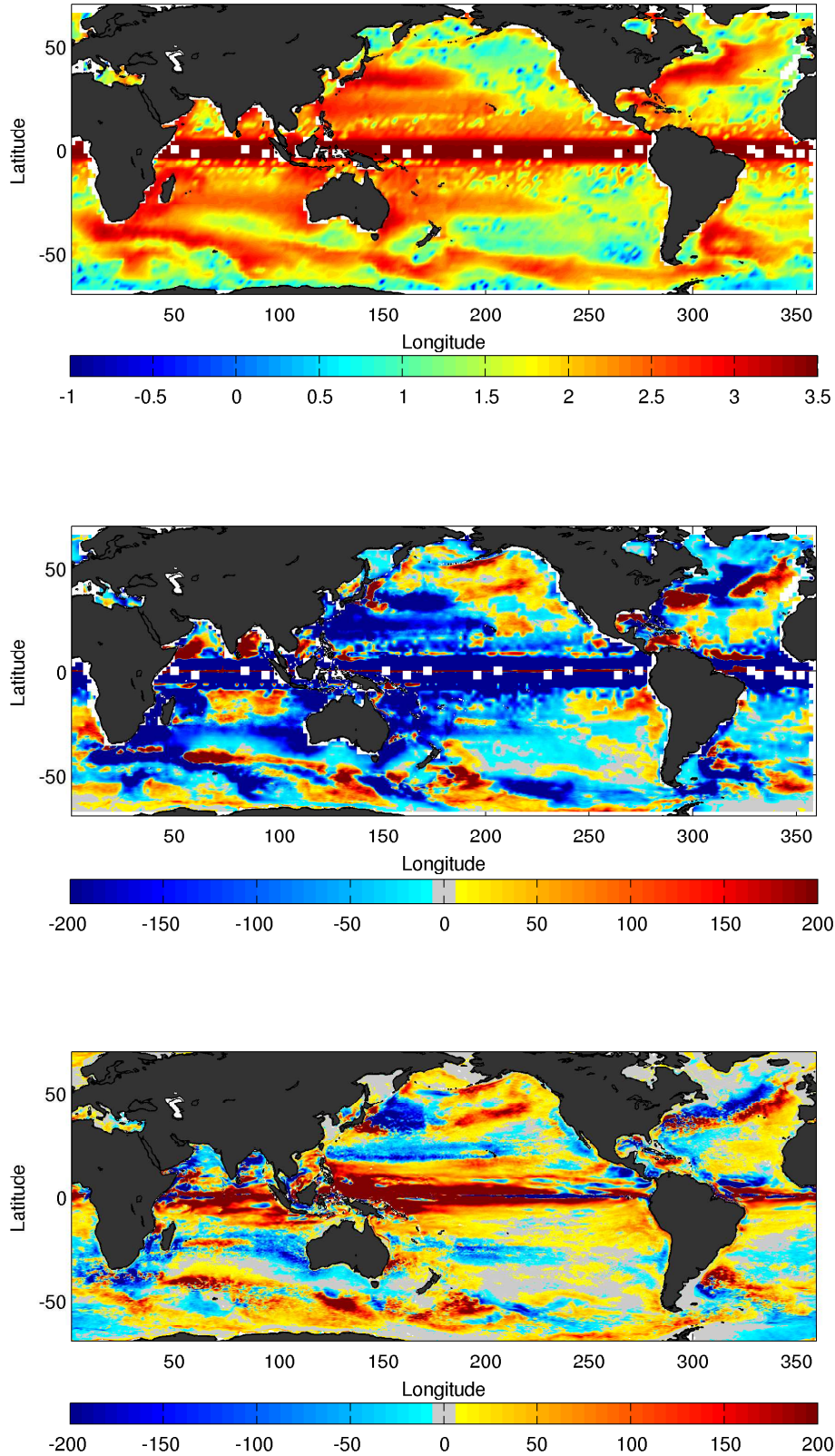
Figure 4.3: EKE in $(cm/s)^2$ (top) from TJJ offset filtered (plotted in logarithmic scale) (middle) difference from STORM_NCEP minus TJJ offset in $(cm/s)^2$ (bottom) difference STORM_NCEP minus STORM_C in $(cm/s)^2$.

EKE in major current systems. It confirms once again a southward shift of the North Atlantic Current, leading to enhanced EKE south of the observed current axis in the STORM_NCEP results. The latter, shows again enhanced eddy variability in the subpolar North Pacific and at several locations along the ACC. Those two features also show up in the EKE difference between the STORM_NCEP and STORM_C runs (bottom panel of **Fig. 4.3**). The differences between TJJ and STORM_NCEP could arise due to various reasons as the sensitivity of the model to high frequency forcing, geographical effects (better resolved in the model due to its higher resolution) or seasonal shifts of current's axis. The latter is supported by the distribution shown in the bottom panel, which suggests that a changing wind forcing is the primary forcing of EKE as expected in tropical and subtropical regions as well as in parts of the southern ocean, North Pacific and North Atlantic oceans. In extended areas in the South Pacific, wind forcing and climatology demonstrate a balanced effect in EKE, while climatology seems to prevail in certain filaments along the ACC and in South Atlantic.

To demonstrate how much kinetic energy resides on the seasonal cycle, the difference in RMS SSH variability and EKE as it results from the STORM_C run is shown in **Fig. 4.4** . The reconstructed field using the annual and semiannual components derived from harmonic analysis is subtracted from the original field, the output was normalized by the mean. The result thus represents the contribution from the seasonal cycle and higher frequencies. Regarding the SSH distribution the seasonal variations appear significant as stated before in the vicinity of major current systems as the North Atlantic Current which demonstrates a southward shift, the Kuroshio, the ACC and the Brazil-Malvinas confluence. This result strengthens the hypothesis that the differences between STROM_NCEP and TJJ in **Fig. 4.3** to some extent are caused by the seasonal shift of the currents.

Regarding the corresponding difference for the EKE field, it is shown that seasonality affects mid and high latitude regions, it is also a dominating factor on basin-scale as in the case of the Indian Ocean. Seasonal changes appear to be more effective in the northern than in the southern Hemisphere.
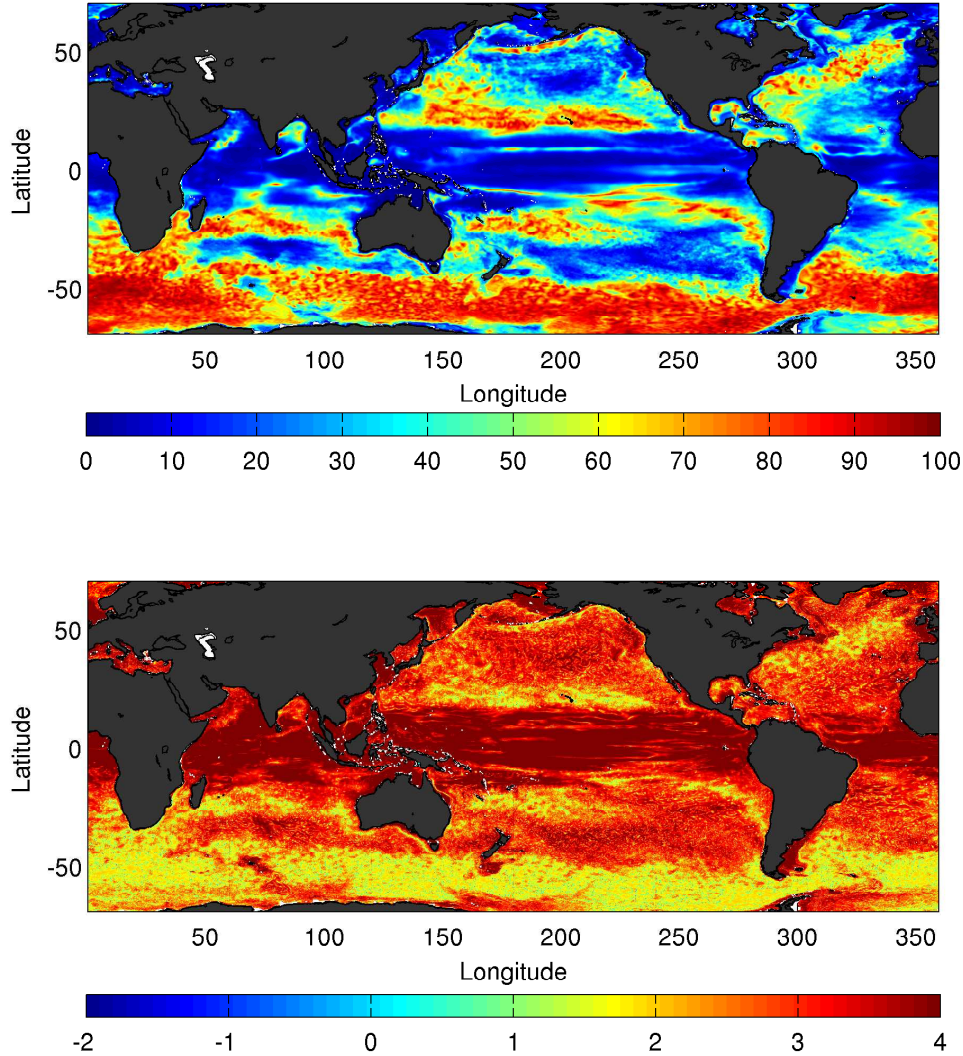
Figure 4.4: Difference STORM_C minus STORM_C filtered by harmonic analysis (top) SSH normalized by the mean in %, (bottom) log10(EKE) normalized by the mean in %

4.3 Temporal Changes of Eddy Variability

To start the discussion of temporal changes of eddy statistics and their dynamical causes, I show in **Fig. 4.5** in its top panel time series of the SSH variance analysed over yearly segments of the TJJ altimetry and from the STORM_NCEP run. In both cases, fields were evaluated in the geographical range between $70\,^\circ$S to $70\,^\circ$N and $0\,^\circ$ to $360\,^\circ$E; in the bottom panel similar results are presented, but for EKE (with the low-
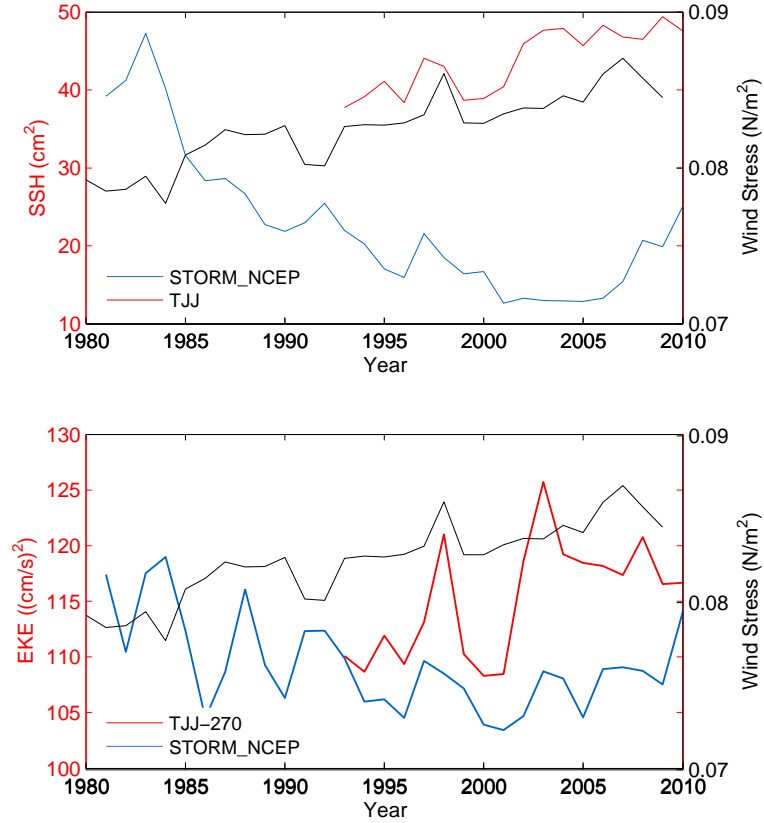
Figure 4.5: Time series of annual (top) SSH variance in cm^2 where TJJ was corrected by an offset of $42\,cm^2$ and (bottom) EKE variability in $(cm/s)^2$ from STORM and altimetry. Wind stress (black line) computed from NCEP reanalysis-1 [Kalnay et al., 1996] is overlaid.

latitudes excluded $\pm 4\,°$). Also shown in both panels is the time-series of the globally averaged wind stress as it results form the NCEP reanalysis-1 [Kalnay et al., 1996] wind for the period 1981 to 2009.

In terms of the SSH variance time-series, both time series show an increase in SSH variability with time (after 2000), superimposed on temporal event-like fluctuations. Most obvious in this respect is an increase in SSH variability during the 1997/98 ENSO event which occurs simultaneously to an increase of the globally averaged wind stress. The increase in altimetric SSH variability after 2002 is not as obvious in the STORM_NCEP results; nevertheless, both STORM and altimetry share an upward tendency (though with different amounts) in variability that is also visible in the wind stress

magnitude. The correlation coefficient between time-series of TJJ and STORM_NCEP of 0.52 is statistically significant; the correlation between SSH variance and wind stress is even higher (~ 0.7) for TJJ, while for STORM_NCEP it is anti-correlated (-0.82).

The time series of annual EKE is also in good agreement between the observed and the modeled fields, especially with respect to temporal fluctuations. As before, the tendency of the EKE values for TJJ and STORM_NCEP agrees with the sign of the tendency in wind stress magnitude increase on global average, suggesting that eddy variability increases in relation to wind stress forcing. The time series of annual EKE derived from TJJ and STORM_NCEP appear well correlated (0.61). The global EKE from TJJ correlates well with the wind stress (coefficient 0.74), while the EKE from STORM_NCEP appears less correlated with a correlation coefficient of -0.6.

For a more detailed consideration of changes in EKE and their relation to atmospheric forcing, a regional consideration is required. For this purpose I show in **Fig. 4.6** changes in EKE as they result from altimetry and the STORM_NCEP run, analysed again over annual segments, but plotted now for individual ocean basins, notably the North Pacific and North Atlantic, the tropical basins between $25°$N and $20°$S, and the individual basins of the southern hemisphere south of $26°$S. Also included in the figure are time series of wind stress magnitude and climate modes for a comparison of changes in eddy variability with changes in the wind forcing and with major climate variability modes. The Pacific Decadal Oscillation (PDO) index was provided by $http://jisao.washington.edu/pdo/PDO.latest$. The North Atlantic Oscillation index (NAO) was obtained from $http://www.cpc.ncep.noaa.gov/products/precip/CWlink/pna/nao\_index.html$. The Southern Annular Mode index (SAM) was provided by $http://www.lasg.ac.cn/staff/ljp/data-NAM-SAM-NAO/SAMI1948-2011.ascii$. The Indian Ocean Dipole Mode index (IOD) was obtained from $http://www.jamstec.go.jp/frcgc/research/d1/iod/DATA/dmi\_HadISST.txt$. The Southern Oscillation index (SOI), provided by $http://www.cpc.ncep.noaa.gov/data/indices/soi$.

In the North Pacific ($120°:250°$E,$20°:66°$N) the correlation between EKE and wind stress is 0.45 with a zero year lag for TJJ and -0.4 with -2 year lag for STORM_NCEP, while the correlation with the PDO index is significant for TJJ (0.55 for 1993 to 2010, 0.80 for 2002 to 2010) but insignificant for STORM_NCEP (0.42 lag 1 year). The response of TJJ EKE to the climate mode is consistent with the one found previously by Chen and Qiu [2010] focusing though to the Hawaiian Archipelago interannual variations of EKE using SSH data of the past 16 years. EKE variations based on their research appear to also be well correlated to the PDO index.
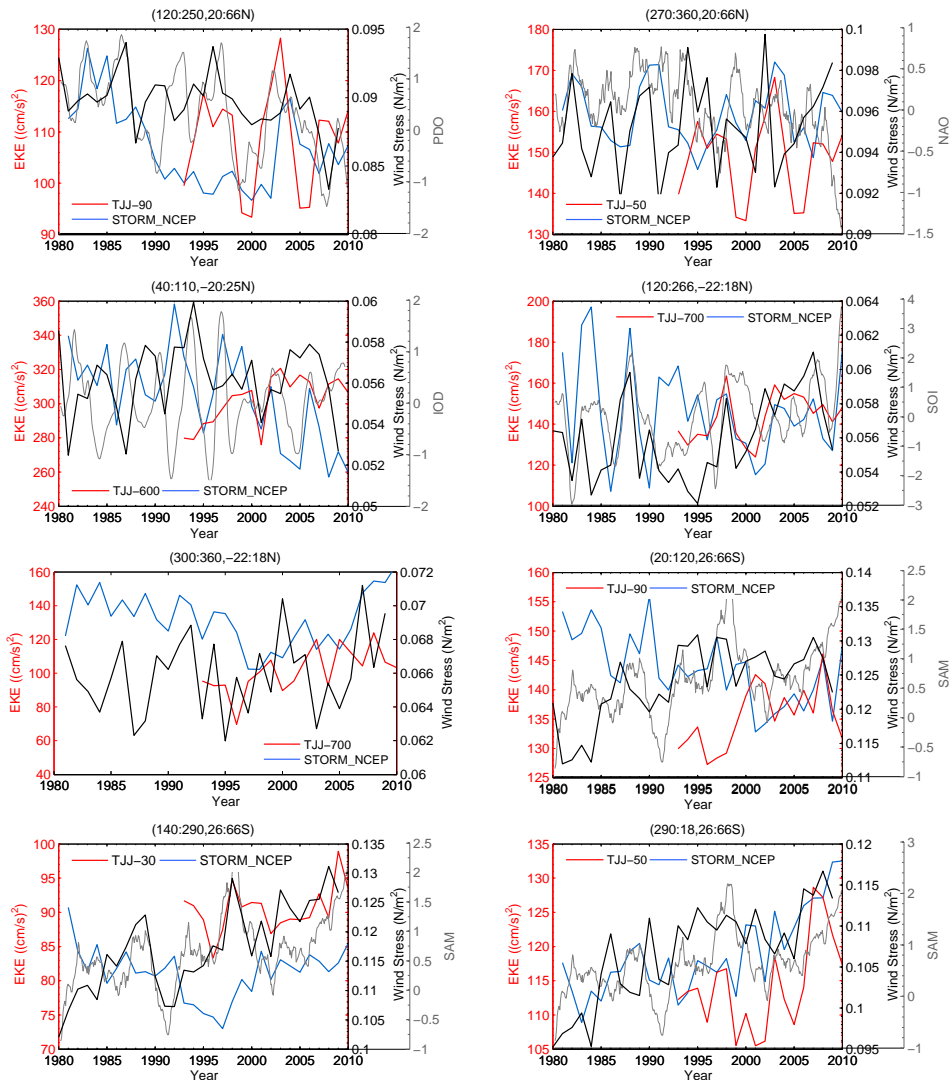
Figure 4.6: Regional time series of EKE from altimetry (red line) and STORM_NCEP (blue line), and the according Wind Stress (black line). The wind velocity product was provided by NCEP Reanalysis. Climate indices (grey line) are overlaid.

In the North Atlantic ($270\,^\circ:360\,^\circ\,\mathrm{E},20\,^\circ:66\,^\circ\,\mathrm{N}$) the correlation between EKE and wind stress is 0.33 with 1 year lag for TJJ and -0.4 with a -2 year lag for STORM_NCEP. The correlation with the NAO index is 0.6 with a four year lag for TJJ, and 0.30 with a one year lag for STORM_NCEP. Once again for altimetry the climate modes correlate better to the time evolution of EKE.

The ACC is one of the most complex parts of the world ocean. As reproduced

4. CAUSES FOR TEMPORAL VARIATIONS OF EDDY KINETIC ENERGY IN THE OCEAN

by Sokolov and Rintoul [2007, 2009a] it consists of multiple jets or filaments, "the association between the jets and particular streamlines persists despite strong topographic and eddy–mean flow interactions, which cause the jets to merge, diverge, and fluctuate in intensity along their path. The path, width, and intensity of the frontal branches are influenced strongly by the bathymetry. The 'meander envelopes' of the fronts are narrow on the northern slope of topographic ridges, where the sloping topography reinforces the effect, and broader over abyssal plains". Sokolov and Rintoul [2009b] argue that the changes in sea surface height in the ACC fronts are mostly the result of changes in the ocean circulation rather than changes in atmospheric heat fluxes. The regional trends and variability in SSH can be associated with the shifts of the ACC fronts. The intensity of the SSH fronts varies with location but not over time. Langlais et al. [2011] also argue that topography controls both the pathways of the ACC fronts as well as their variability. Thompson [2010] suggests that the two processes that effect the dynamic nature of the Southern ocean jets is the topography which can modify the gradients of local potential vorticity as well as the mean flow. More recently Morrow et al. [2010] after investigating the interannual variations in Southern Ocean EKE using 16 years of altimetric data, compared to the Southern Annular Mode (SAM) and El Niño Southern Oscillation (ENSO) index, found that the EKE response depends on the interplay between wind forcing, topography, and mean flow and produces a strongly heterogeneous distribution in the Southern Ocean. They observed that the EKE response varies regionally and the strongest EKE appears in the Pacific. They indicate that when strong positive SAM events coincide with La Niña periods, as in 1999, anomalous meridional wind forcing is enhanced in the South Pacific Ocean, which concludes to an increase in EKE with a lag of 2-3 years. On the other hand when positive SAM events coincide with El Niño periods, as in 1993, the climate modes are in opposition in the South Pacific, leading to a weak EKE response during the mid–1990s.

In the southern ocean the results presented here show that the correlation between EKE and wind stress is 0.33 in the Indian Ocean section of the ACC ($20°:120°$E, $26°:66°$S) with a -6 year lag for TJJ, and -0.58 with no lag for STORM_NCEP. The correlation with the SAM index is 0.4 with a -9 year lag for TJJ, and -0.39 with a 3 year lag for STORM_NCEP. Thus, in this part of the Southern ocean altimetry appears to respond equally well to both wind forcing and climate modes, while the modeled EKE variations are better correlated to the wind. The same is true over the Pacific section of the ACC ($140°:290°$E, $26°:66°$S) where the correlation between EKE and wind stress is 0.42 and 1 year lag for TJJ, and -0.58 with a -10 year lag for

STORM_NCEP . The correlation with SAM is 0.45 with -1 year lag for TJJ, and -0.28 with a -10 year lag for STORM_NCEP . At the ACC Atlantic section ($290^{\circ} : 18^{\circ}\,\mathrm{E}$, $26^{\circ} : 66^{\circ}\,\mathrm{S}$) the correlation between EKE and wind stress is 0.58 with a -1 year lag for TJJ, and the same for STORM_NCEP but now with a 2 year lag. The correlation with SAM is 0.51 with a -1 year lag for TJJ, and 0.36 with 2 year lag for STORM_NCEP . Previously Lauderdale et al. [2012] shows that "when the winds are shifted to the north, the ACC appears to align with the position of maximum zonal-mean wind stress generally leading to a good correlation value. When the winds are shifted to the south the ACC responds in a similar way, again aligning with the latitude of zero wind stress curl" .

A correlation between changes in the wind forcing and EKE seems to be less obvious in low latitudes. In the Indian Ocean the correlation between EKE and wind stress is 0.43 with a -8 year lag for TJJ, and 0.49 for STORM_NCEP . The correlation with the Indian Ocean Dipole Mode index (IOD) is 0.32 with a 8 year lag for TJJ, and -0.23 with a -2 year lag for STORM_NCEP . In the Tropical Pacific ($120^{\circ} : 266^{\circ}\,\mathrm{E}, 22^{\circ}\,\mathrm{S} : 18^{\circ}\,\mathrm{N}$) the correlation between EKE and wind stress is 0.65 for TJJ, and 0.31 with a 10 year lag for STORM_NCEP . The correlation with the Southern Oscillation index (SOI) is 0.35 with a 7 year lag for TJJ, and 0.41 with a -1 year lag for STORM_NCEP . Zhang and Church [2012] showed that the decreasing sea levels in the eastern equatorial Pacific is mainly associated with the Pacific Decadal Oscillation. In the Tropical Atlantic ($300^{\circ} : 360^{\circ}\,\mathrm{E}, 22^{\circ}\,\mathrm{S} : 18^{\circ}\,\mathrm{N}$) the correlation between EKE and wind stress is 0.48 with a 1 year lag for TJJ, and 0.36 for STORM_NCEP .

All correlation coefficients and lags are computed for the longest available overlap between respective pairs of time series available. In several regions there are qualitative similarities between changes in EKE between TJJ and STORM_NCEP . Outside the tropics, amplitudes of variations in SSH variability and in EKE do agree as do the general amplitudes (we recall the off-set-correction in TJJ results). In the tropical regions, TJJ is still a factor of approximately $60\,(cm/s)^2$ higher than STORM_NCEP in high and low latitudes and around $600\,(cm/s)^2$ in the tropics. With respect to wind stress changes, we see a pronounced agreement between observed TJJ EKE changes and wind stress variations. This holds especially for the off-equatorial regions. It also holds for STORM_NCEP results. However, in tropical regions this is not always the case, specially in the tropical Atlantic, where STORM_NCEP results seem to decline while wind stress and altimetry show an increase in amplitudes. Nevertheless, EKE variations have a lot in common with variations in wind stress, which in turn have a lot in common with characteristic climate modes of variability present in most of the basins (e.g, PDO,

NA, ENSO, SAM). The correlation between TJJ and STORM_NCEP EKE varies from 0.4 to 0.6 with one exception in the Indian Ocean $(40\,^\circ:110\,^\circ\,\mathrm{E}, 20\,^\circ\,\mathrm{S}:25\,^\circ\,\mathrm{N})$ where a significant correlation is absent.

Focusing on high energetic regions of EKE, the annual EKE time series in relation to time varying wind stress are shown in **Fig. 4.7**. The agreement between TJJ and STORM_NCEP is good, described by a correlation greater than 0.6. The response to the wind forcing as shown in **Table 4.1** varies regionally. The temporal variation of EKE as described from TJJ in the location of major currents appear to have a response between zero to two years to atmospheric forcing with the exception of the Gulf Stream current which decorrelates to the wind stress with a four year lag. The corresponding responses of EKE from STORM_NCEP to wind stress are quite different, describing an EKE field with a much slower response to the external forcing in most regions and also less correlated to it.
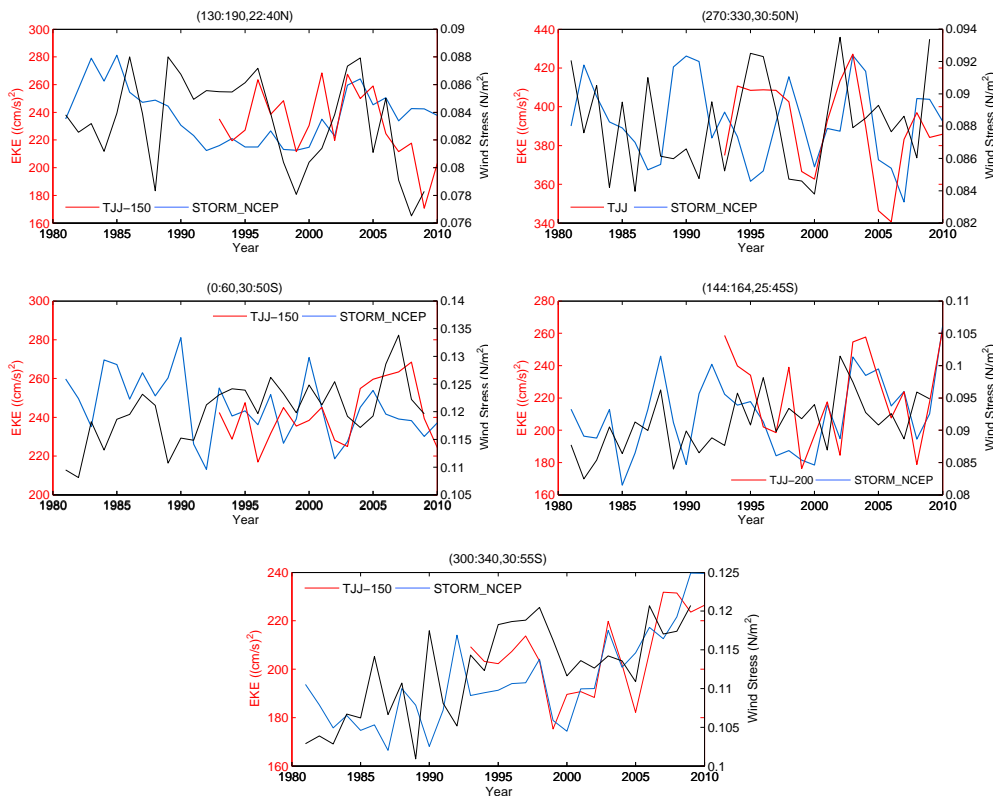
Figure 4.7: Time series of EKE from altimetry and STORM, and Wind Stress in selected western boundary current regions.

$r_tau/lag(yr)$	TJJ	STORM_NCEP
Kuroshio	0.51/1	0.43/-7
Gulf Stream	-0.62/4	-0.41/-9
Agulhas	0.42/-2	-0.34/-4
E. Australia	0.41/1	0.28/1
Malvinas	0.50/0	0.48/2

Table 4.1: Cross Correlation Coefficient EKE and Wind Stress in high energetic regions and lag in years.

4.4 Temporal Trends in Eddy Variability

To isolate decadal trends from shorter-term variations in the time series of the root mean square SSH variability and EKE, in the top panel of **Fig. 4.8** the normalized (with respect to the respective variance) temporal trends for SSH anomaly from 1993 to 2010 are depicted. Shown in the middle and bottom panels of the figure are similar trends, but computed over the shorter periods 1993 to 2001 and 2002 to 2010. In all cases, results are structured showing TJJ in the left and STORM_NCEP in the right columns, respectively. In all the fields a 60 % significance layer is shaded, values with p-values greater than 0.6 are considered insignificant. For more details, the methodology followed for the calculation of the p-values is given in Chapter 2, section 2.3.2.

Sea level changes are spatially non-uniform, many regions experience a higher or lower rate of sea level change than the global average up to five times the global average value [Zhang and Church, 2012, and reference therein]. The spatial distribution of temporal trends of SSH for the full 18 year period indicates an overall positive trend of 1.28 % per year in the TJJ results. The corresponding distribution derived from STORM_NCEP depicts more negative trends regionally compared to that of TJJ. The overall positive global trend is 0.059 % per year, i.e., that is less than half of the observed increase. The main differences between TJJ and STORM_NCEP trends are located in the Indian Ocean, tropical Pacific, North Atlantic and along the ACC (compare also Fig. 4.6).

Geographically, temporal trends of SSH are highly variable. In the case of TJJ results, they are positive in the Indian Ocean, in the extra tropical Atlantic and in parts of the northeast and southeast Pacific, while the west Pacific has negative trends. If we move away from the tropics where the signal to noise ratio renders TJJ data problematic, there are similarities between the temporal trends described by TJJ and STORM_NCEP especially in the North/South Pacific and Atlantic.
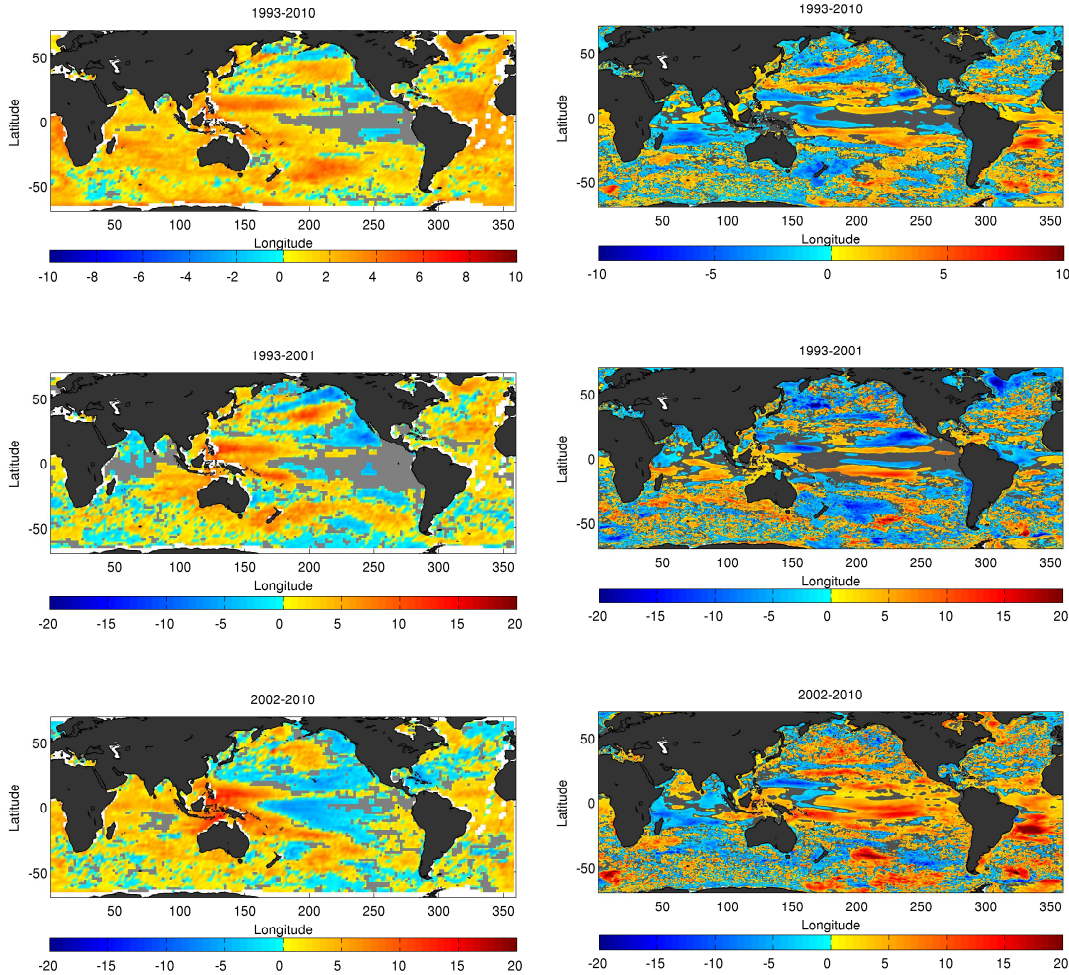
Figure 4.8: Normalized temporal trend of SSH root mean square $\%/yr$ (left) TJJ, (right) STORM_NCEP .

Most of the discrepancies between the two data sets arise from the 1993 to 2001 subperiod. A previous study of SSH changes in the extraequatorial South Pacific Ocean using satellite altimetry data by Qiu and Chen [2006] also indicated that the decadal trends in the 1990s were positive in the $30\,^\circ$S–$50\,^\circ$S band and negative poleward of $50\,^\circ$S, this picture was inverted since 2002. They suggested that this pattern and the reversal is due to the accumulation of the wind-forced SSH anomalies along Rossby wave characteristics.

For the 1993 to 2001 as well as for the 2002 to 2010 subperiod for TJJ, the distribu-

tion of positive and negative trends becomes more distinct. The trends are larger during the former subperiod relative to the latter (2.34 % per year as opposed to 1.14 % per year), indicating main differences at the vicinity of the Somali current and west Indian coast current, the tropical Pacific and North Atlantic, these trends could be related to climate modes that might not be resolved accurately in the STORM experiment. The distributions derived from STORM_NCEP show higher positive trends during 2002 to 2010(1.99 % per year) than during 1993 to 2001 (−0.81 % per year) while the same differences are apparent locally as for the 18 year long trends.
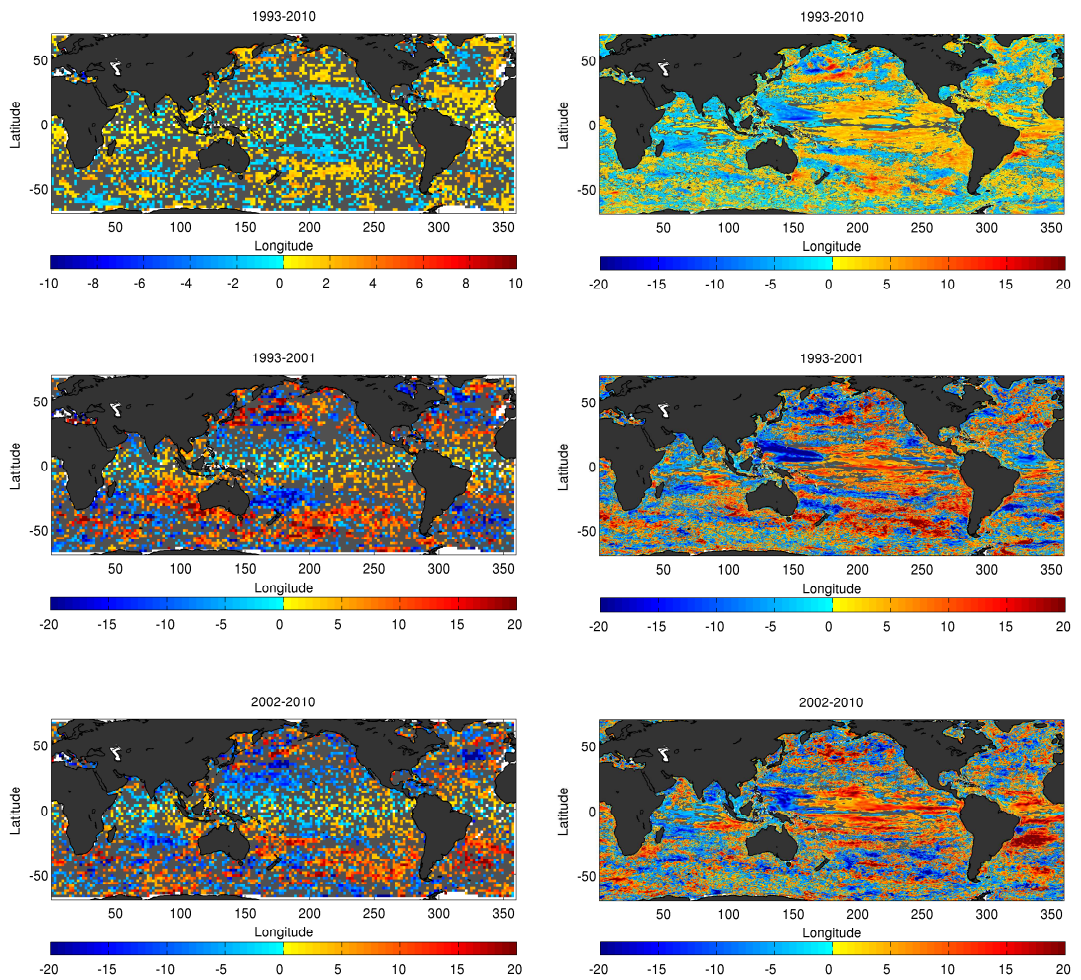
Figure 4.9: Normalized temporal trend of EKE %/yr (left) TJJ, (right) STORM_NCEP .

The spatial distribution of temporal trends of EKE (**Fig. 4.9**, top) is again geographically highly variable, being positive for TJJ in the Indian Ocean, in the extratropical Atlantic and in parts of the northeast and southeast Pacific, while the west Pacific has negative trends. The temporal trends of EKE are mostly positive, with negative trends at mid latitude in the Pacific, the north Atlantic and parts of the South Ocean. The temporal trend of EKE as a global average is positive 0.10 % per year for TJJ while for STORM_NCEP goes up to 0.72 % per year. The trend's distribution during the sub-periods of 1993 to 2001 and 2002 to 2010 leads to a high variable pattern of negative and positive trends with higher positive trend 0.44 % per year for the first sub-period and 0.18 % per year for the second concerning TJJ while the opposite is true for STORM_NCEP (0.51 % per year as opposed to 1.73 % per year).

Previously Polito and Sato [2008] estimated regional variability of SSH anomaly temporal trends, from a 13 year long SSH data record. They observed that in some regions, the variation in amplitude over the 13 years is comparable to the standard deviation of the data, so they suggested that in this case, the energy is transferred from the mean currents to the waves and eddies through barotropic and baroclinic instability processes that are more pronounced in the western boundary current extension regions.

Recently Backeberg et al. [2012] using satellite altimetry observations from 1993 to 2009, argued that mesoscale variability of the Agulhas system has intensified. The authors suggested that the intensification is associated with an increased South Equatorial Current driven by enhanced trade winds over the tropical Indian Ocean, resulting in accelerated eddy propagation. They interrelated the decreasing mean kinetic energy and increasing EKE trends in the region as indicating that the energy contained in the current has shifted from the mean to the eddying component since 1993, rendering the southern Agulhas Current more variable. As seen in **Fig. 4.9** and **Fig. 4.7** EKE has increased form 1993 to 2010, however the correlation to the wind amounts to 0.4 indicating that the conversion of the mean kinetic energy to eddy kinetic energy effects the southern Agulhas Current variability.

4.5   Mechanism for EKE Variability

Sea surface height is an integrated quantity that reflects baroclinic and barotropic variability (e.g.,Stammer et al. [2000]; Vinogradova et al. [2007]). As such it depends on density anomalies of the water column, but also on variations of the external atmospheric forcing. In general terms, the eddy kinetic energy results mostly from instabilities of the large scale circulation, interaction between currents and bathymetry and

the direct forcing of the wind [Ferrari and Wunsch, 2009]. von Storch et al. [2012a] investigated the full Lorenz energy cycle in the STORM_NCEP run; results suggest that the eddy kinetic energy is driven mostly by baroclinic instability processes and by fluctuations of the wind field. Thus, the wind effect is firstly examined here, before moving on to investigate internal variability.

4.5.1 EKE–Wind Relation

The spatial distribution of temporal trends of wind stress magnitude are shown in **Fig. 4.10** for the same periods that are analysed before in Figs.4.8 and 4.9. The figure reveals clear trends that for the period 1993 to 2009 show a decrease in wind stress over the North Pacific and the sub-polar North Atlantic. A decrease over large parts of the Indian Ocean and its SICC sector is also observed. In contrast, increases occur in the tropical and south Pacific, parts of the subtropical North Atlantic and parts of the South Atlantic.

The temporal trend of wind stress (overall trend 2.06 % per year) is positive in the equatorial, south Pacific and Atlantic oceans and in parts of the ACC, while it is negative in the Indian Ocean, the north Pacific and north Atlantic. The time series of annual wind stress suggests that there is a positive global trend with significant maxima in 1997 and 2008. During the sub-period 1993 to 2001 the overall trend is slightly positive 0.012 % per year while in 2002 to 2009 it increases to 2.92 % per year. From comparing the trends of EKE and wind stress there are indications of a direct relation locally, but also the existence of non-local effects.

To further investigate the relation between local wind stress changes and changes in eddy variability I show in the top panels of **Fig. 4.11** and **Fig. 4.12**, for TJJ and STORM_NCEP respectively, the cross correlation coefficient of EKE time series with the global wind stress, the wind velocity was provided by NCEP reanalysis-1 [Kalnay et al., 1996]. A 90% significance level is shaded in both figures, which was computed following the methodology described in section 2.3.2.

In the North Pacific the maximum cross correlation coefficient values are acquainted along the coasts, in the almost zonal band extending from $25\,°\,N$ to $35\,°\,N$ and north of $40\,°\,N$. The distribution in this zonal band could be associated with the generation of Rossby waves at the eastern boundary and their propagation to the western boundaries where they are dissipated, since it corresponds to decadal lags (see below). Along the KurilKamchatka Trenches it is suggested [Itoh and Yasuda, 2010, and reference therein] that the northward movement of anticyclonic eddies is either driven by the image effect
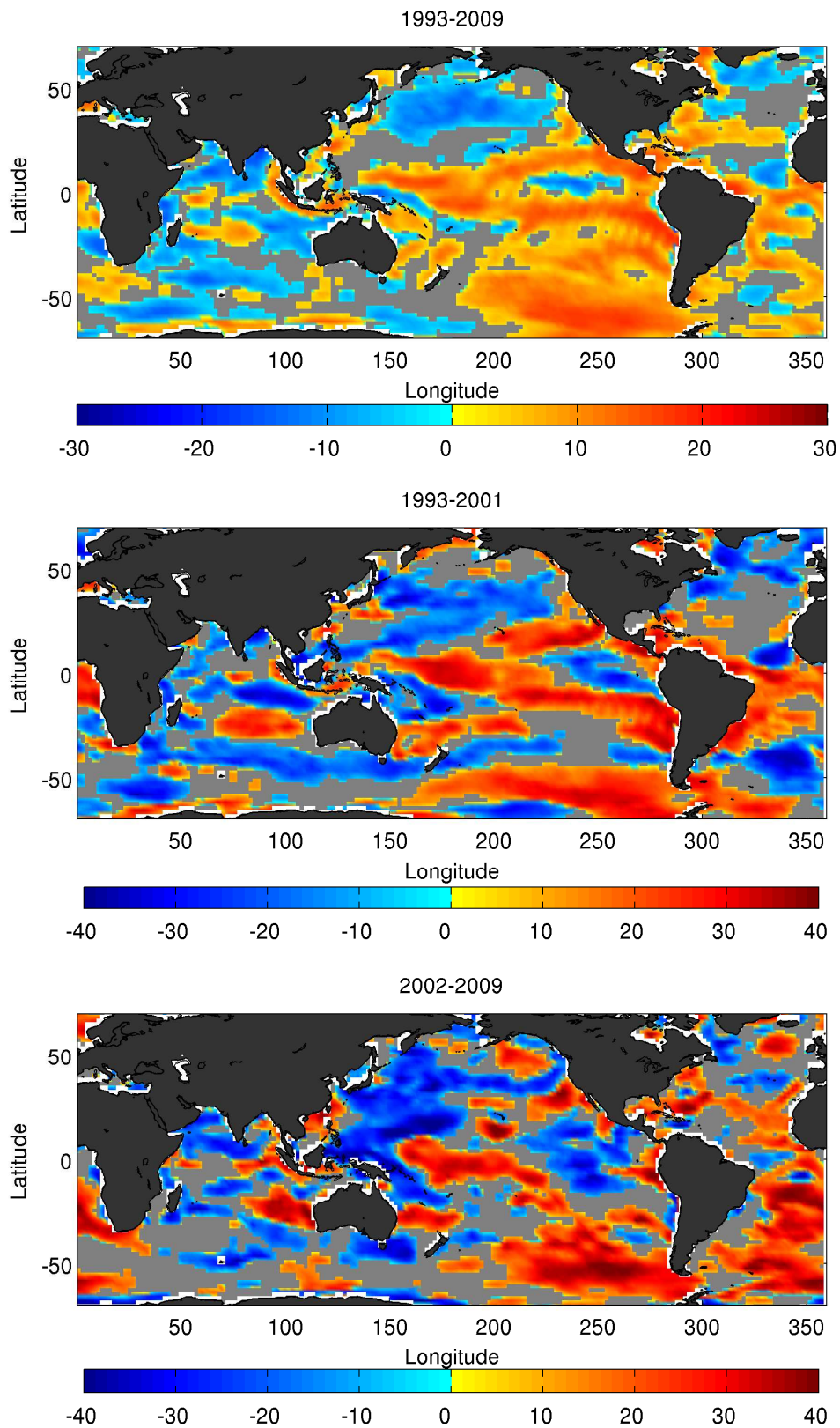
Figure 4.10: Wind Stress normalized (with standard deviation) temporal trend in $\%/yr$.
The wind velocity provided by NCEP Reanalysis.

of a steep slope or the pseudo effect or due to variations in wind-driven transport. In my results the correlation is moderately positive indicating that the wind is not the most important forcing. In the North Atlantic correlations greater than 0.4 are located along the coasts, along the Gulf stream and along part of the Labrador current associated locally with lags greater than 10 years.

In the Indian Ocean the effect of the wind forcing appears to be more direct and significant with correlation greater than 0.6 close to the equator and at the north-west entouraged by lags close to zero. As stated by Fu [2007, and reference therein] due to the small size of the Indian Ocean the wave reflection affects rapidly the entire basin, where "the Kelvin waves generated in the eastern basin are quickly reflected back as Rossby waves, which are reinforced by the wind forcing after moving back to the forcing region because of the synchronized arrival of the waves with respect to the forcing".

In the Tropical Pacific a dipole of positive and negative correlations occur in the west and east respectively associated with lags close to zero. This distribution could be associated with "the seasonal shift of the NECC center west of the dateline that originates in the east of the dateline and is being conveyed westward by Rossby waves. In other words, in the western Pacific, the Rossby wave effect dominates the seasonality of the NECC, with the Ekman pumping only playing a secondary role. In addition to the above mentioned factors, eddies are important in driving and positioning the NECC in the western equatorial Pacific. By strengthening the NECC, eddies can move its center closer to the equator via non-linear effects" [Hsin and Qiu, 2012, and reference therein].

In the Tropical Atlantic, where the southeast and northeast trades converge into the Inter tropical Convergence Zone (ITCZ), a complex pattern of positive and negative correlations between EKE and wind stress signifies the different response north and south of the North Equatorial Counter Current (NECC).

The Southern Ocean and the ACC will be described in three section since they demonstrate different characteristics and responses to the wind forcing. In all three sections (South Indian section, South Pacific section and South Atlantic section) the cross correlation coefficient between wind stress and EKE is negative along the Antarctic Convergence zone. Positive correlations can be observed along the coasts and in the South Pacific mainly concentrated in a zonal band between $40\,^{\circ}$S and $55\,^{\circ}$S at the vicinity of the Peru current, this pattern could be associated with westward propagating Rossby waves.

The lag of maximum absolute cross correlation of EKE and wind stress (bottom panels of **Fig. 4.12** and **Fig. 4.11**, for TJJ and STORM_NCEP respectively) reveals a complex pattern of responses of EKE to the atmospheric forcing. If we focus on
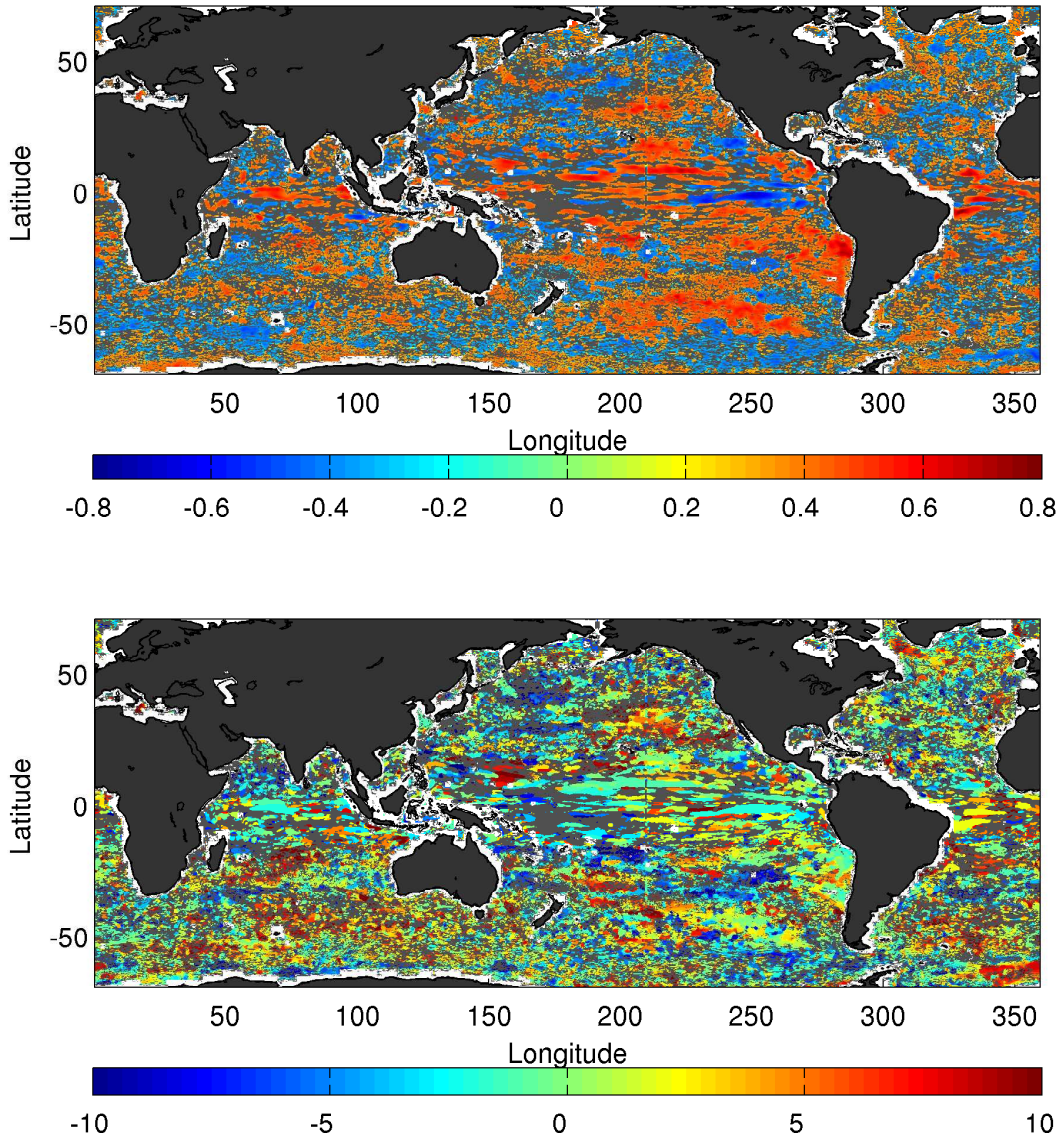
Figure 4.11: (top)Cross correlation coefficient and (bottom) Lag of maximum cross correlation of EKE and Wind Stress, the wind velocity provided by NCEP Reanalysis, for STORM_NCEP .

the parts of the World Ocean where the effect of the wind appears significant (cross correlation coefficient greater than 0.5) we find that these regions do not coincide with regions of high EKE. Regions with lags of ± 2 years can be found at the equatorial regions of the Indian, central Pacific and Atlantic oceans, at the Peru/Chile current
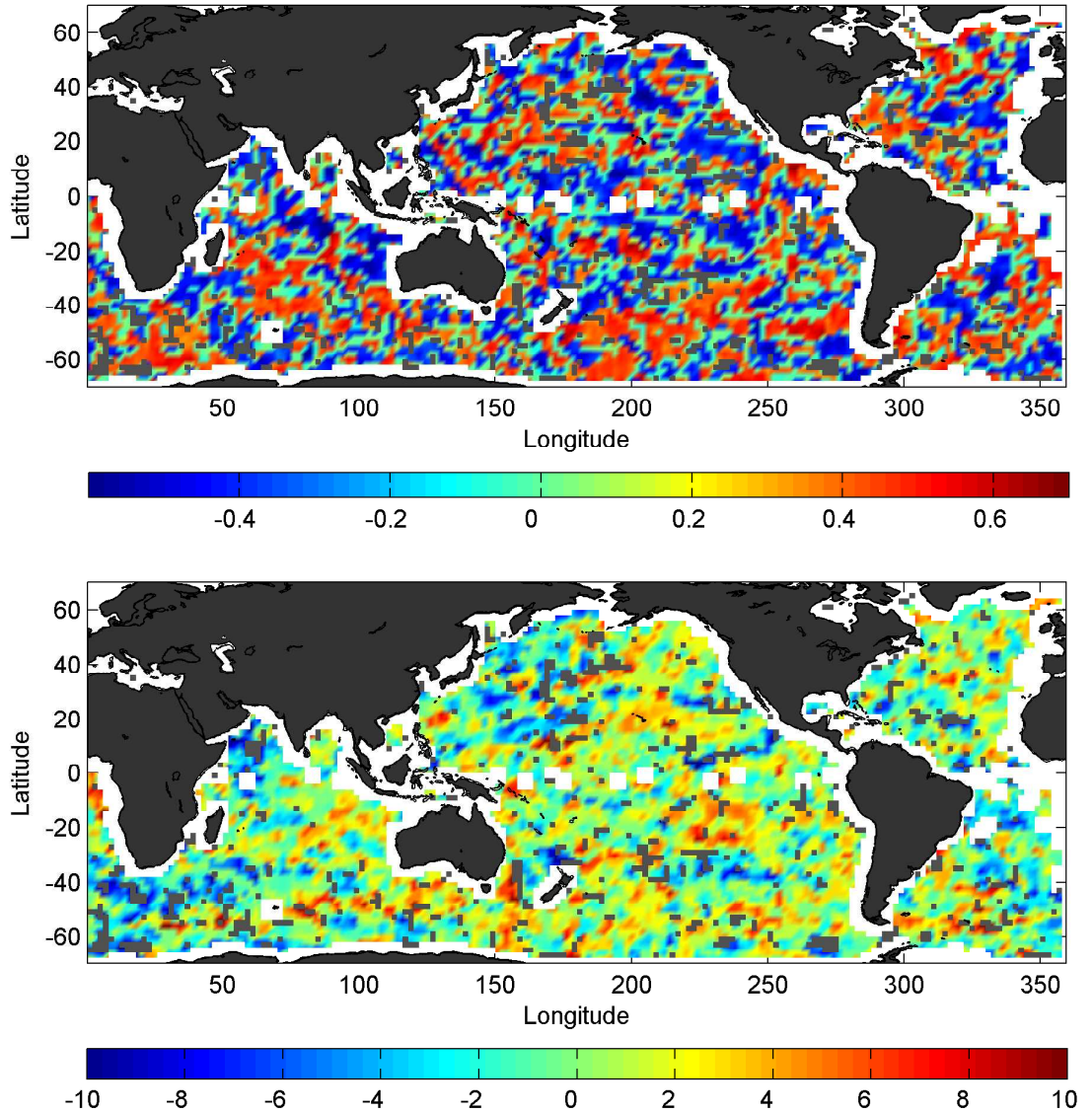
Figure 4.12: (top) Cross correlation coefficient and (bottom) Lag of maximum cross correlation of EKE and Wind Stress, the wind velocity provided by NCEP Reanalysis, for TJJ.

and the Pacific section of the ACC. While lags of approximately ±8 years of significant coefficients are sparse, thus it is difficult to determine a pattern. A study by Meredith and Hogg [2006] using an eddy resolving ocean model to investigate the lag between wind forcing and the response in the eddy field, suggested that the lag is caused by the

time the wind needs to influence the deep circulation of the ACC. Their analysis also suggested that the increase of the winds in the last few decades might be reflected as an increase in eddy activity.

It should be noted, that the negative correlation coefficients which remain even after the application of the significance level filter do not have to my understanding a physical meaning. They could be indicative though of non-local effects of the wind stress. Another possible hypothesis when observed at regions where there is an increase of EKE could be that this increase is due to other dynamical reasons than the effect of the wind forcing.

Results shown before suggest that a simple local relation between wind stress changes and EKE does not exist but does rather reflect basin scale statistics involving local and remote responses to changes in forcing. The question arises whether the term "eddy saturation" introduced by Böning et al. [2008] is valid. Though their suggestion, that stronger westerly winds induce, with a lag of 2–3 years, an increase in eddy activity, is also evident in the time series presented here. Also Mahadevan et al. [2010] used a numerical model and scaling diagnostic to determine whether the effect of eddies or wind dominates under different conditions. They concluded that though the cross-front transport of buoyancy induced by the down-front component of the wind opposes restratification by mixed layer eddies, it becomes diminished as the eddies and growth of the frontal instability disrupt alignment between the wind and frontal axis.

4.5.2 Internal Variability

In principle, eddy energy can vary due to internal variability of the flow field and associated flow instabilities. In order to have a first estimate on how much of the variability in the EKE field is due to the wind forcing I use the STORM run forced solely by climatology as a null hypothesis. The time series of EKE derived by the climatological run regionally (**Fig. 4.13** are superimposed on the corresponding time series computed by the NCEP run shifted in the lag of maximum cross-correlation between the two time series. In some cases the time series follow each other closely, which could depict that internal processes within the ocean are responsible for the variability. In that aspect there is the need to verify that this variability corresponds to a physical process and that it is not an artefact of the statistics.

A straight forward way to test the hypothesis is to use a variance ratio test for random walk, which is based on the very property that the variance of the increments of a random walk is linear to the sampling interval. I run this test under the condition
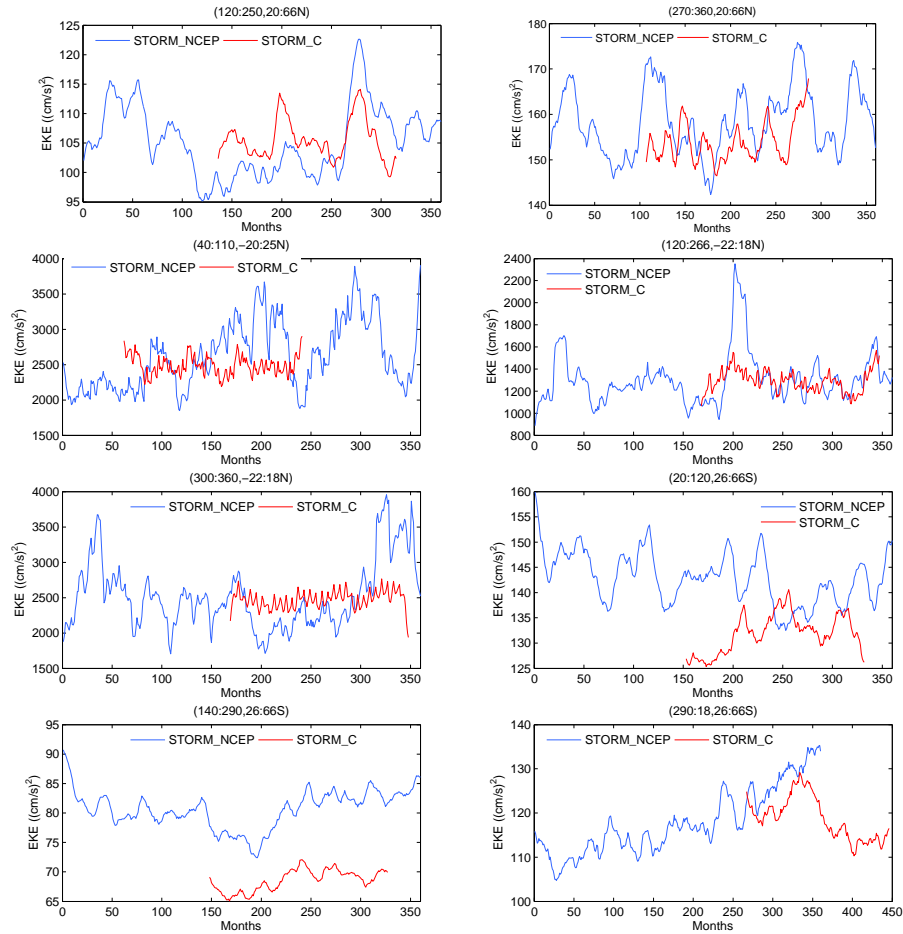
Figure 4.13: Regional time series of monthly EKE, from STORM_NCEP and STORM_C smoothed using a 6month running mean filter.

that the values are independent identically distributed, on a 5 % significance level and for different periods (2,4,8,16 months). The results are summarized in **Table 4.5.2**, where zero means that the test fails to reject the random walk null hypothesis, while the opposite is true when the test returns the value one. There are certain regions where the variability of the climatology is clearly not a random process, while in others my results are inconclusive since I have to estimate why the test succeeds for some periods and fails for others. It is interesting that the three sections of the ACC have different outcomes.

	Periods			
Region	2	4	8	16
(120°:250°E, 20°:66°N)	1	1	0	0
(270°:360°E, 20°:66°N)	1	1	1	1
(40°:110°E, −20°:25°N)	0	1	1	1
(120°:266°E, −22°:18°N)	0	1	1	1
(300°:360°E, −22°:18°N)	0	1	1	1
(20°:120°E, 26°:66°S)	0	0	1	1
(140°:290°E, 26°:66°S)	1	1	1	1
(290°:18°E, 26°:66°S)	1	1	1	1

Table 4.2: Variance ratio test regionally

4.6 Discussion and Conclusions

I identified the highest variability of SSH, located in the vicinity of major current systems, meandering jets and frontal areas from the geographical distribution of root mean square SSH variability over 18+ years of satellite altimeter data. The sea surface height variability pattern is consistent with earlier results. The comparison with the corresponding distribution of STORM_NCEP SSH anomaly reveals that the simulation along the North Atlantic Current, the Agulhas, the north-equatorial currents in the Pacific and Atlantic oceans has lower variability and higher variability at the sub-polar North Pacific and the subtropical oceans. While the amount of SSH variability originating from temporal variations in the surface forcing can be derived from the difference in RMS SSH variability from STORM_NCEP minus STORM_C. The fields of EKE, also consistent with previous results, indicate the less energetic regions in the North and South Pacific and the most energetic regions coincide with regions western boundary currents. The model underestimates the amount of EKE in major current systems. These differences are attributed to the sensitivity of the model to high frequency forcing, geographical effects or seasonal shifts of current's axis. While seasonality affects mid and high latitude regions and is a dominating factor on basin-scale as in the case of the Indian Ocean.

The good quantitative agreement of SSH and EKE between altimetry and model is demonstrated from their zonal averages. Several disagreements are located around $40\,°S$, $50\,°N$. The respective zonal average from the STORM_C run highlights the importance of interannual changes in the forcing fields for enhancing eddy variability in the ocean.

The time series of the SSH variance of the TJJ and the STORM_NCEP run show an increase of SSH variability with time (after 1993), superimposed on temporal event-like fluctuations. Both STORM and altimetry share an upward tendency in variability that is also visible in the wind stress magnitude with a correlation of ~ 0.7 for TJJ, while for STORM_NCEP it is negatively correlated (-0.82). The time series of EKE have the same sign of the tendency in wind stress magnitude increase on global average, suggesting that eddy variability increases in relation to wind stress forcing.

Regional changes in EKE temporal variations in correspondence with wind stress and climate indices, show qualitative similarities between TJJ and STORM_NCEP. A pronounced agreement between observed TJJ EKE changes and wind stress variations is present in the off-equatorial regions, while in tropical regions this is not always the case. EKE variations have a lot in common with variations in wind stress, which in turn have a lot in common with characteristic climate modes of variability present in most of the basins. There are extended parts along the ACC where no local direct relation between changes in wind stress and EKE was found. The same holds in other parts of the ocean, pointing to non-local forcing effects of eddy variability. This implies that regionally no direct relation can be found between changing wind forcing and eddy variability. However, on basin average, changes in eddy energy appear correlated with climate modes.

The normalized 18+ year temporal trends of SSH anomaly, and EKE from TJJ and from STORM_NCEP indicate that both are positive in the last 18 years in most parts of the world's oceans (1.28 % per year for TJJ results and 0.059 % per year for STORM_NCEP respectively). However this increase is not uniform but shows a complex pattern. Away from the tropics similarities between the temporal trends discribed by TJJ and STORM_NCEP were found, especially in the North/South Pacific and Atlantic. The trends are stronger during the 1993-2001 subperiod relative to the 2002-2010 (2.34 % per year as opposed to 1.14 % per year) for SSH. EKE shows higher positive trend 0.44 % per year for the first sub-period and 0.18 % per year for the second concerning TJJ while the opposite is true for STORM_NCEP (0.51 % per year as opposed to 1.73 % per year). The corresponding temporal trends of wind stress decrease over the North Pacific, the sub-polar North Atlantic and over large parts of the Indian Ocean, while it increases at the tropical and south Pacific, parts of the subtropical North Atlantic and parts of the South Atlantic. As a global average wind stress increased at a rate of 2.06 % per year, during the sub-period 1993 to 2001 the overall trend is slightly positive 0.01 % per year while in 2002 to 2009 it increases to 2.92 % per year.

4. CAUSES FOR TEMPORAL VARIATIONS OF EDDY KINETIC ENERGY IN THE OCEAN

The pattern of cross correlation of EKE and wind stress, suggests that a simple local relation between wind stress changes and EKE does not exist but does rather reflect basin scale statistics involving local and remote responses to changes in forcing. The negative correlation coefficients can not be attributed a physical meaning. A possible hypothesis when observed at regions where there is an increase of EKE could be that this increase is due to other dynamical reasons than the effect of the wind forcing.

Chapter 5

Estimation of Frequency and Wavenumber Spectra of SSH

5.1   Introduction

Ocean variability is broadband so in order to understand its characteristics the use of spectral analysis is required [Scharffenberg and Stammer, 2011; Stammer, 1997a]. Global wavenumber spectra of sea surface height and eddy kinetic energy was firstly studied by Fu [1983] introducing a new era of investigating turbulence in the ocean. From that point on spectral analysis was applied extensively on global and on regional scale (e.g., Le Traon and Rouquet [1990]; Provost and Le Traon [1993]; Stammer and Böning [1992]). A detailed description of the global characteristics of ocean variability in the frequency and wavenumber domain for SSH was provided by Stammer [1997a]. As seen before [Ferrari and Wunsch, 2009] all the spectral density estimates of horizontal kinetic energy display a low-frequency, nearly white band at periods shorter than 40 days. As described by Ferrari and Wunsch [2009] this band then falls in an approximate power law of the form σ^{-q} (where σ is the frequency and q the rate of decay), which is called the geostrophic eddy range. Also an inertial peak exists at $\sigma \approx f$, where f is the Coriolis frequency and separates the geostrophic eddy band from higher-frequency non geostrophic motions. The aliasing of the frequency spectra from tidal residuals or high frequency variability even after corrections have been applied to the data, should be addressed. As stated by Ponte and Lyard [2002] the inverted barometer correction reduces high frequency variability aliasing at mid and high latitudes but not at low latitudes. But at periods shorter than 4 months the contamination from high frequency aliasing remains substantial even after multiple-track data averaging,

5. ESTIMATION OF FREQUENCY AND WAVENUMBER SPECTRA OF SSH

especially in coastal areas.

As indicated by Scharffenberg and Stammer [2011] an important issue is the unknown noise level in altimetric observations below wavelengths of 100 km, leaving the question open on whether we can understand the existing SSH and slope spectra in terms of underlying ocean dynamics. In general, the EKE wavenumber spectrum can be retrieved from the SSH spectrum multiplied by k^2 [Sasaki and Klein, 2012] (where k is the wavenumber).

Only a few wavenumber spectral estimates of ocean variability exist (e.g. Le Traon et al. [2008]; Stammer [1997a]; Xu and Fu [2012, 2010]). These spectra tend to be red without the distinctive features seen in the frequency domain [Ferrari and Wunsch, 2009]. Xu and Fu [2010] argued that surface quasi-geostrophic theory can be applied only in the transition zones from the edge to the core of the high energy regions of the major ocean current systems. They identified the spectral slope of sea surface height in the core regions of high eddy energy to be close to k^{-4} in the wavelength range of $70 - 250$ km, an observation consistent with the dominance of fronts that cannot be fully accounted for by the surface quasi-geostrophy theory.

The pattern of spatial variability of the wavenumber spectral slope as shown by Xu and Fu [2010] is similar to the pattern of global distribution of eddy variability. They describe the distribution as having steeper spectral slopes in the location of higher eddy variability, and indicated the consistency with the argument that the steep spectrum is associated with highly non-linear dynamics while the flat spectrum is associated with more linear dynamics. A follow-up paper [Xu and Fu, 2012] revealed that after removing the white noise level of altimetry, which was best estimated from the spectral values at wavelengths of $25 - 35$ km, the spectral slope values changed significantly over most of the oceans.

In this chapter the computation of frequency and wavenumber spectra globally and regionally is revisited, taking advantage of the 18+ year long altimeter data set, results of which are compared against those of MITgcm model outputs for resolutions of $1/3°$, $1/6°$, $1/12°$, $1/24°$ and STORM_NCEP model. The comparison of the altimetry against MITgcm and STORM_NCEP is twofold. On one hand it is useful so as to test the model and on the other hand to identify altimeter data errors and their impact on the estimated frequency and wavenumber spectra, inferred spectral relations and underlying dynamics. I will investigate if such a joint model-data analysis of frequency and wavenumber spectra can be used to identify dynamical principles, leading to observed sea surface height time-series and to separate those from noise effects in the data.

This chapter is structured as follows: in section 5.2 the frequency spectra results on a global and regional scale are presented and discussed. In section 5.3 the wavenumber spectra results are discussed on global and regional scale. While in section 5.4 a summary of the outcomes and a list of concluding remarks is given, derived from the research presented in the current chapter.

5.2 Frequency Spectra

The first to calculate global frequency and wavenumber spectra of sea surface height were Wunsch and Stammer [1995] using two year data of TOPEX/Poseidon. The study was picked up by Stammer [1997a] using three year data of TOPEX/Poseidon to calculate sea surface height, slope and geostrophic velocity spectra in frequency and wavenumber domain. The frequency spectra provide an overview of the frequency characteristics on a global and regional scale. From the frequency spectra the importance of seasonal variations or shorter can be quantified and analysed.

5.2.1 Global

The globally averaged frequency spectra of SSH anomaly (covering $0°$ to $360°$E in longitude and $70°$S to $70°$N in latitude) computed from the along-track TJJ satellite data and STORM_NCEP is shown in **Fig. 5.1**, the tidal alias periods for TOPEX/Poseidon have been overlaid. As a reminder it should be noted here that all model spectra are computed after data was interpolated onto the satellite-tracks (more details were given previously in Chapter 2).

The maximum energy is found as expected at the annual period. At periods longer than 300 days the energy distribution follows a $\sigma^{-0.34}$ relation for TJJ and $\sigma^{-0.46}$ for STORM_NCEP . For timescales shorter than 300 days the rate of decay of the frequency spectra follows a $\sigma^{-0.98}$ relation for TJJ, while STORM_NCEP decays faster following a $\sigma^{-1.36}$ relation. As indicated by Arbic et al. [2012] realistic ocean gcms, and gridded satellite altimeter data "exhibit qualitative similarities, with steeper slopes at higher frequencies and flatter slopes at lower frequencies" . This is the case also for the results presented here computed from the along-track altimeter and model data.

The higher frequencies as seen in the bottom panel of **Fig. 5.1** depict more tidal aliasing, than the lower frequencies. Although since the model does not include tides the peaks at 180.7 days and at 120 days can not be attributed to tidal aliasing, but rather to the seasonal cycle. The TJJ spectra depicts higher peaks in M2 and S2 periods than the ones found previously in Stammer [1997a] (fig. 8a). Also prominent peaks at

5. ESTIMATION OF FREQUENCY AND WAVENUMBER SPECTRA OF SSH
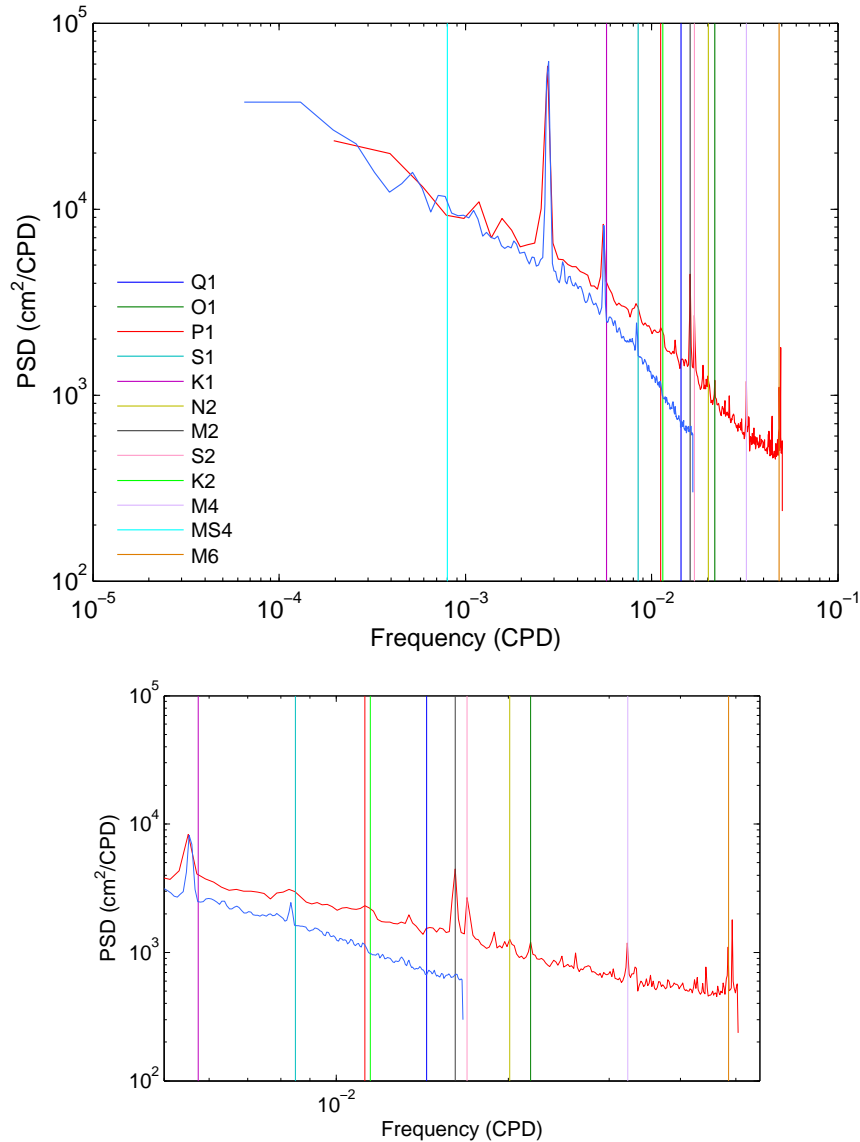
Figure 5.1: Globally averaged Sea Surface Height anomaly frequency spectra (bottom) zoom into high frequencies, derived from TJJ (red) and derived from STORM_NCEP (blue). The TOPEX/Poseidon tidal alias periods are overlaid.

TJJ frequency spectra are centered at the O1 and M4 tidal periods. It should also be noted that though STORM_NCEP is qualitatively close to altimetry at low frequencies, it does not contain the same variability at high frequencies indicating either that the model is lacking the ability to describe submesoscale phenomena or that the altimetry

spectra is dominated by noise at these frequencies.

5.2.2 Regional

The spectra are averaged over a large area that contains different dynamical characteristics. To get a better understanding of how the spectra slopes change regionally and how the latitudinal dependence influences the shape of the spectra, I focus on smaller regions. The frequency spectra is computed for the extended North Atlantic ($260\,^{\circ}$E to $360\,^{\circ}$E in longitude, $30\,^{\circ}$S to $70\,^{\circ}$N in latitude) from TJJ, MITgcm and STORM_NCEP data (**Fig. 5.2**). The frequency spectra for TJJ at timescales longer than 300 days follows relations of $\sigma^{-0.24}$, for timescales shorter than 300 days the rate of decay is $\sigma^{-0.86}$, the power laws are close to the relations seen at the global spectra for the same timescales. The frequency spectra derived from the MITgcm and
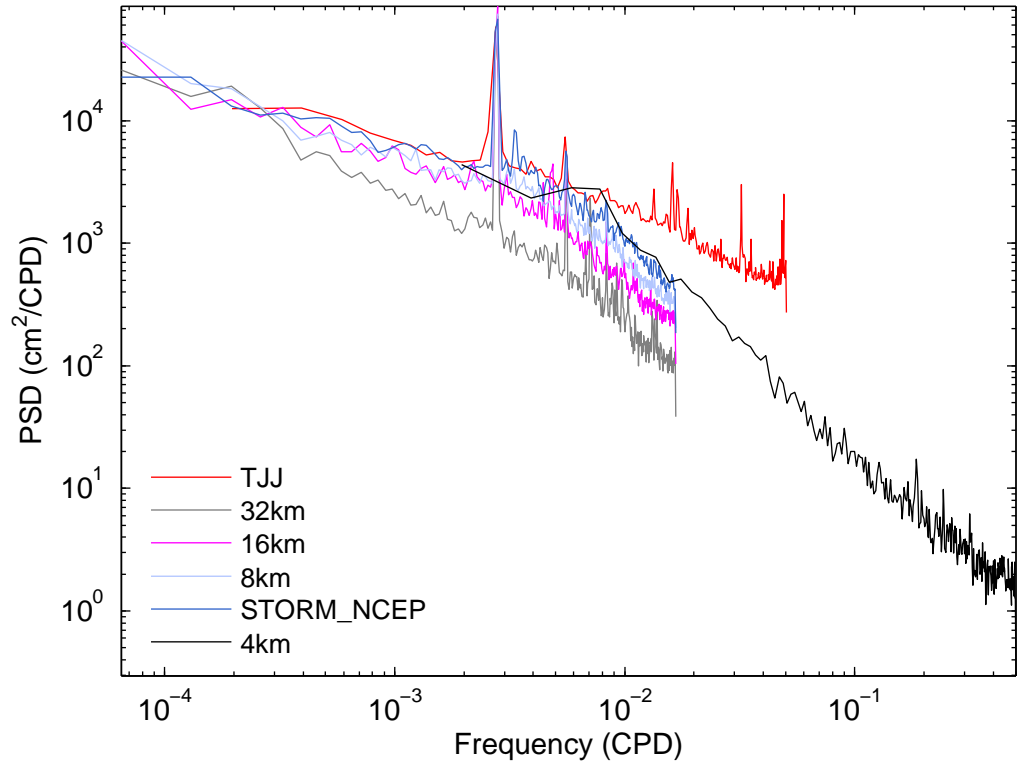
Figure 5.2: Frequency Sea Surface Height spectra from models with different resolutions and altimetry for the extended North Atlantic.

5. ESTIMATION OF FREQUENCY AND WAVENUMBER SPECTRA OF SSH

STORM_NCEP resolve less frequency range, due to the fact that the data is monthly averaged, with the exception of the $1/24\,^\circ$ which is derived from daily SSH output. In **Table 5.1** the power law relations for the different resolutions and different timescales are shown. For timescales longer than 300 days the $1/3\,^\circ$ frequency spectra follows roughly $\sigma^{-2/3}$ relations, while $1/6\,^\circ$, $1/12\,^\circ$ and STORM_NCEP roughly follow $\sigma^{-1/3}$ relations. For timescales shorter than 300 days the frequency spectra for all resolutions are decaying following an approximately $\sigma^{-5/3}$ relation. The $1/24\,^\circ$ frequency spectra follows closely the other model's spectra with decay rate of -1.03 for time scales longer than 57 days, and extends to higher frequencies (time scales shorter than 51 days) following, the same as the other simulated spectra, decay rate around $\sigma^{-5/3}$. It is clear that as the resolution of the model increases the closer it gets to the observed regime, indicated by a shift to higher magnitudes. However, at high frequencies even the highest resolution we have available for this study the spectra fails to describe the same spectral density contained in TJJ, though the spectral slopes tend to be qualitatively close.

Resolution	T > 300 days	T < 300 days
$1/3\,^\circ$	-0.7	-1.6
$1/6\,^\circ$	-0.5	-1.6
$1/12\,^\circ$	-0.5	-1.5
STORM_NCEP	-0.3	-1.6

Table 5.1: MITgcm and STORM_NCEP frequency spectra relations

To get an overview of how the shape of the frequency spectra changes with latitude and in sub-domains characterised by different energetic regimes, the frequency spectra in each $10\,^\circ \times 10\,^\circ$ grid box for TJJ, MITgcm and STORM_NCEP is shown in **Fig. 5.3** to **Fig. 5.5**.

As a general description, the frequency spectra estimated from the different models appear smoother and steeper than the spectra of TJJ in the zonal band between $20\,^\circ$ N and $60\,^\circ$ N, while they are flatter at the vicinity of the Loop current. The highest SSH variability as seen before in SSH root mean square distribution can be found along the Gulf Stream current and its extension towards the North Atlantic Current (NAC) ($20\,^\circ$ N to $50\,^\circ$ N). Along the coast the tidal aliasing of the TJJ frequency spectra is becoming more important even after the corrections, due to the complexity of the tidal dynamics as well as the dynamic response to pressure forcing there, as suggested by Ponte and Lyard [2002]. In the Tropics, the semi-annual frequency peak becomes
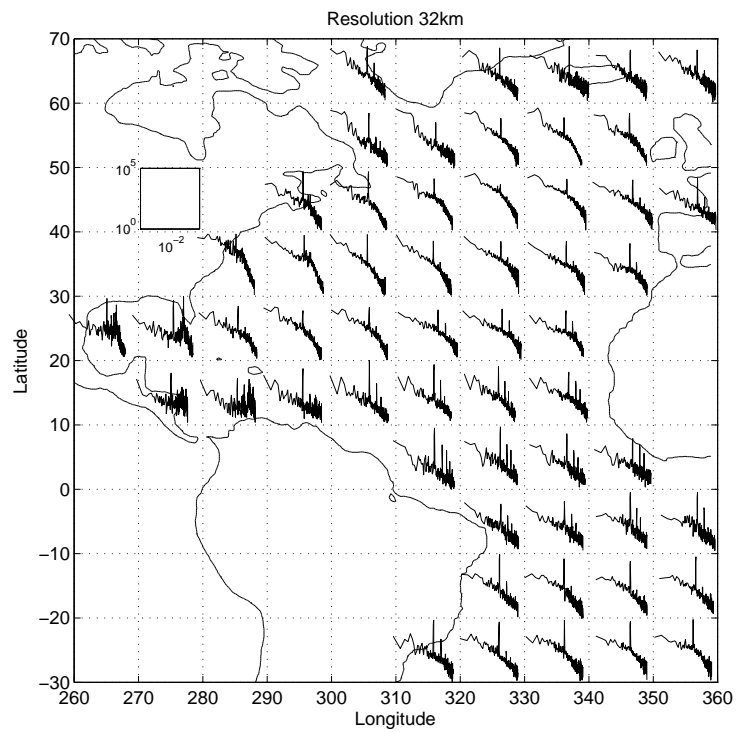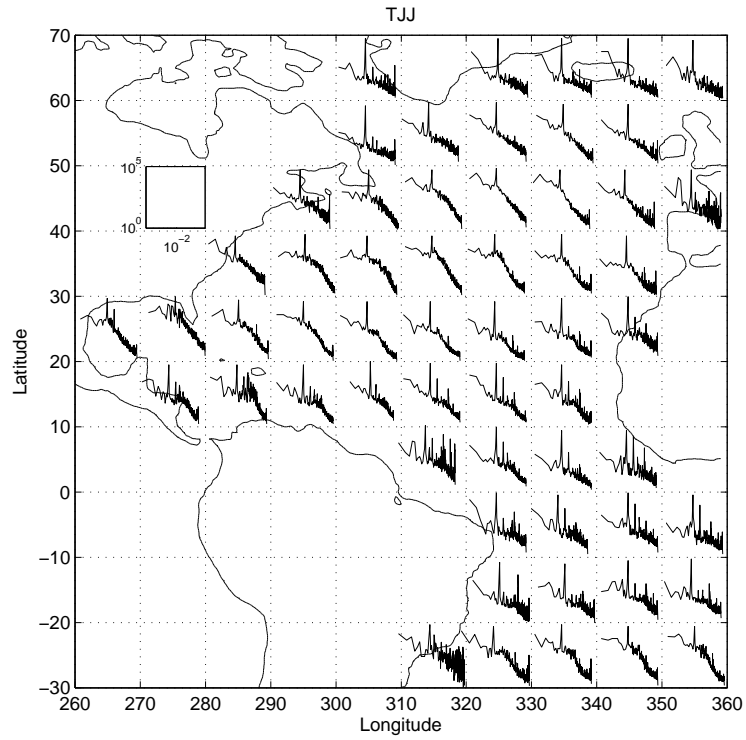
Figure 5.3: Frequency Sea Surface Height spectra from TJJ and MITgcm $1/3°$ in $10° \times 10°$ grid boxes.
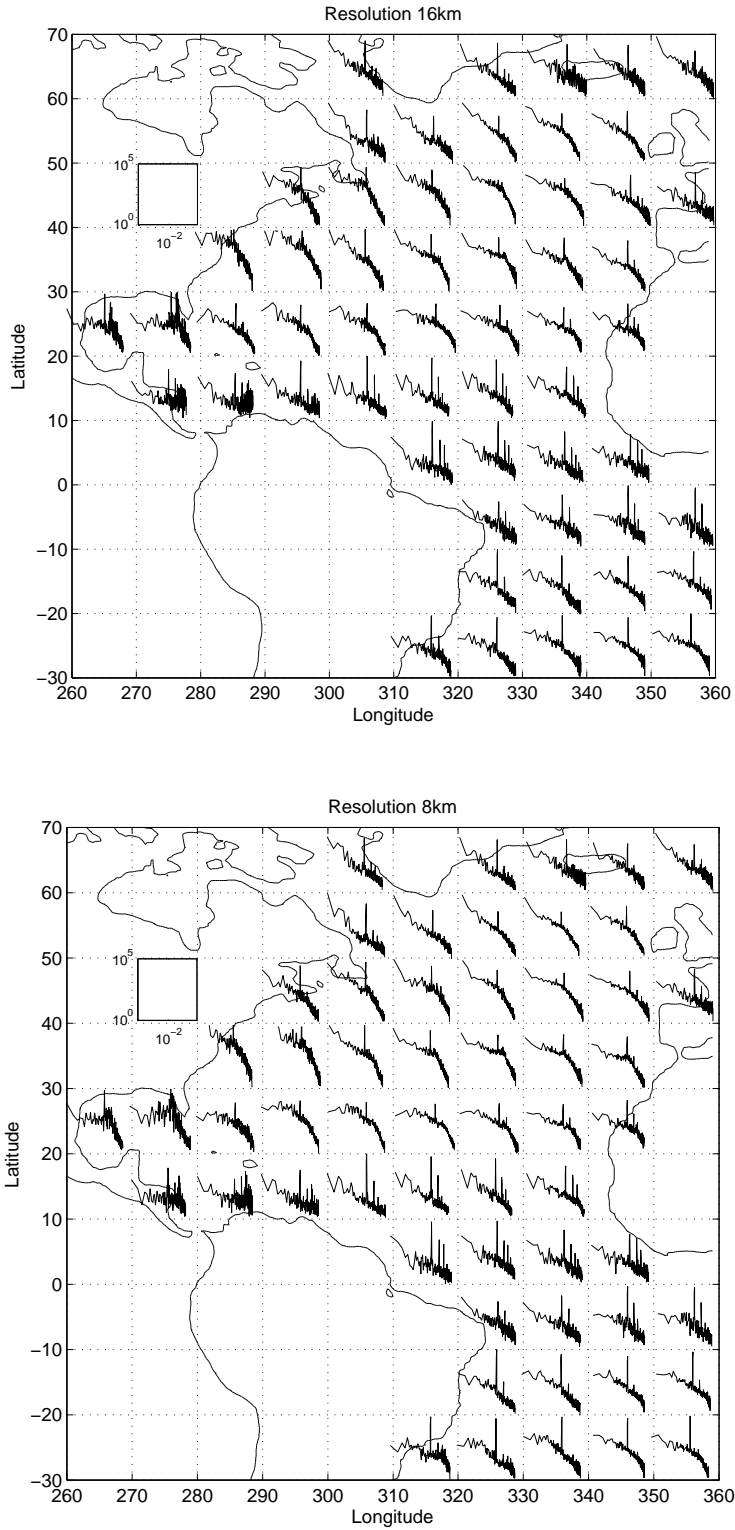
Figure 5.4: Frequency Sea Surface Height spectra from MITgcm $1/6\,^\circ$ and MITgcm
$1/12\,^\circ$ in $10\,^\circ \times 10\,^\circ$ grid boxes.
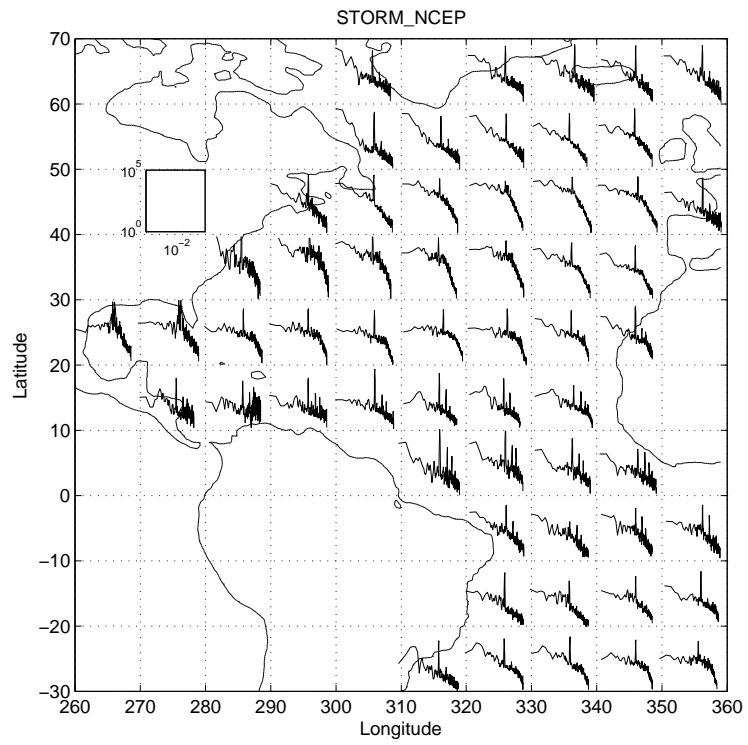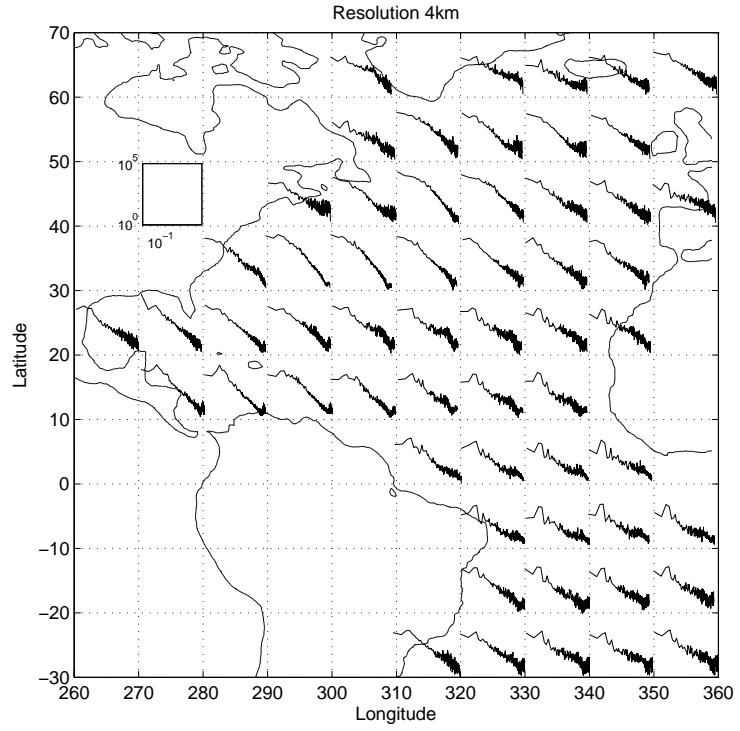
Figure 5.5: Frequency Sea Surface Height spectra from MITgcm $1/24°$ and STORM_NCEP in $10° \times 10°$ grid boxes.

more pronounced even in the models frequency spectra indicating the dominance of the seasonal cycle. In mid latitudes, the shape of the spectra appears to be close to the averaged spectra over the whole region. In high latitudes, the spectra contains less energy and becomes flatter and smoother. We need to get a better understanding of the latitudinal dependence of the power laws governing the frequency spectra as previously done by Scharffenberg and Stammer [2011] who compared frequency spectra for the zonal and meridional velocity components computed for different latitude bands. They found a latitudinal dependence of the cut-off period, "for periods shorter than about 100 days. All spectra had a power law close to σ^{-2} that slightly changed with latitude, and was steeper at low latitudes and less steep at high latitudes".

In order to identify the local differences in dynamics I zoom in several $10°\times 10°$ regions, revealing characteristic spectral shapes as shown in **Fig. 5.6** and **Fig. 5.7**, all frequency spectra were filtered using a sliding average filter. For all the selected regions the models have steeper slopes, estimated as least square fits, than altimetry. The first region $(300°:310°\,\text{E},\ 50°:60°\,\text{N})$ located in the vicinity of the Labrador current, TJJ shows a slight decay of $\sigma^{-0.6}$ for periods longer than roughly 500 days and of $\sigma^{-1/3}$ for periods shorter than 180 days. In the same region the models however show three discrete decay relations for different timescales. The first can be described approximately by a $\sigma^{-5/3}$ relation for $T > 950$ days, leading to an almost white spectra $\sigma^{-0.003}$ for $410 < T < 770$ days and a relation of $\sigma^{-0.8}$ for $T < 307$ days. The $1/24°$ frequency spectra follows closely the decay described by the rest of the models with a rate of σ^{-1} for periods longer than 57 days, but decays faster $(\sigma^{-1.4})$ for $T < 51$ days.

In $330°:340°\,\text{E},\ 40°:50°\,\text{N}$ for timescales longer than 590 days altimetry and models spectra appear to be following roughly the same relation of $\sigma^{-0.3}$, however for timescales shorter than 300 days the models spectra is decaying with a rate of $\sigma^{-7/3}$ thus faster than altimetry which follows a relation of $\sigma^{-4/3}$. The $1/24°$ for $T > 57$ days decays to a rate similar to TJJ $(\sigma^{-0.8})$, while for $T < 51$ days the relation is closer to the model's $\sigma^{-7/3}$.

The power spectral density at the region located in the vicinity of the Loop Current $(270°:280°\,\text{E},\ 20°:30°\,\text{N})$ appears highly variable. Seasonal variations dominate the frequency spectra enhancing different peaks for different resolutions. The semiannual peak is apparent for all derived spectra, while for timescales shorter than 122 days the models spectra is decaying with a rate close to $\sigma^{-2.5}$ and TJJ close to $\sigma^{-4/3}$. Also an internal or external forcing increases the spectral density significantly for periods $169 - 282$ days for TJJ, $120 - 169$ days for $1/3°$, $169 - 284$ days for $1/6°$ and closer to the annual frequency $(248 - 340\ \text{days})$ for $1/12°$. It can not be distinguished whether
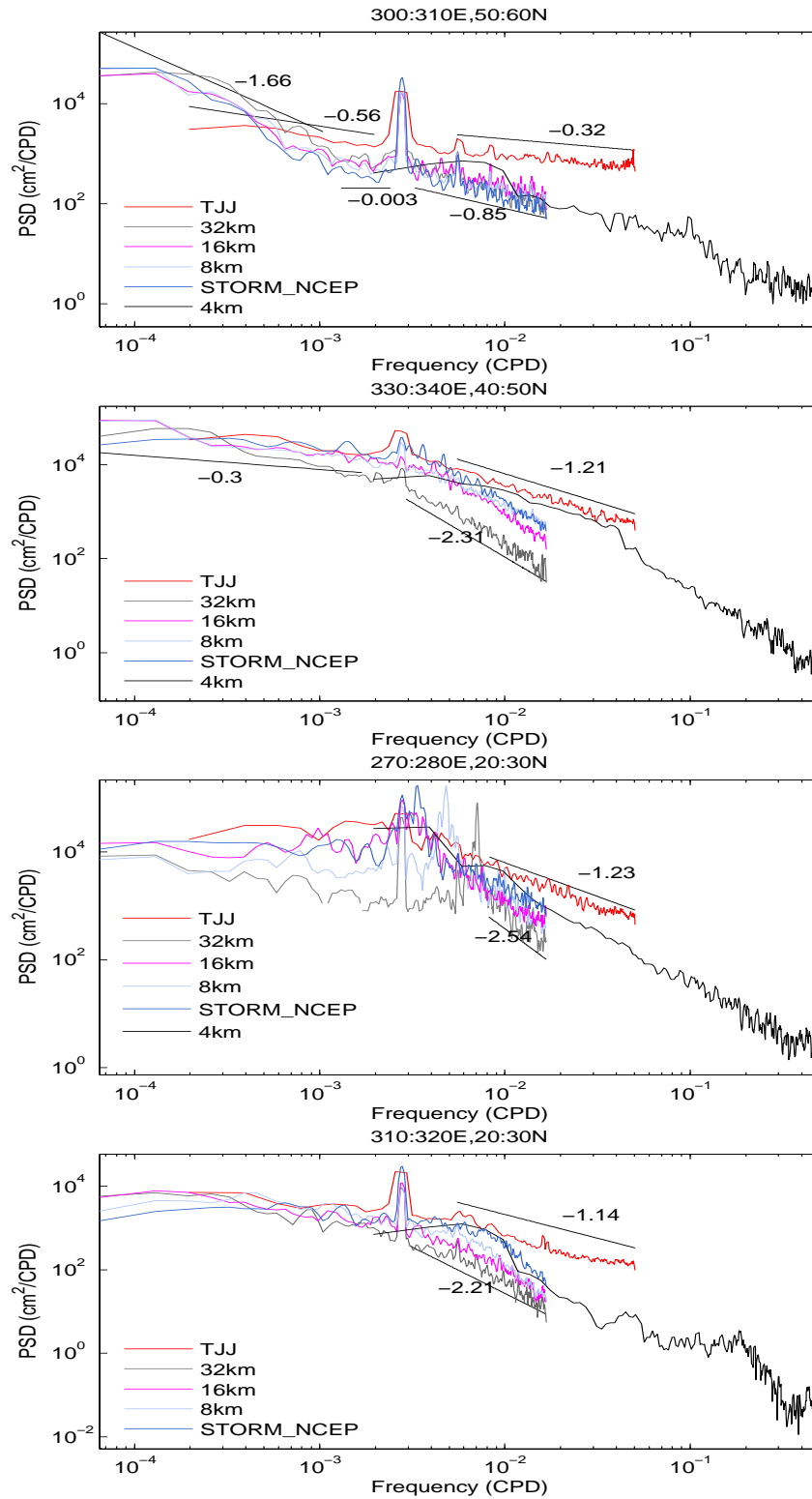
Figure 5.6: Frequency Sea Surface Height spectra from model and TJJ for characteristic $10\,^{\circ} \times 10\,^{\circ}$ grid boxes, smoothed by a sliding average filter.
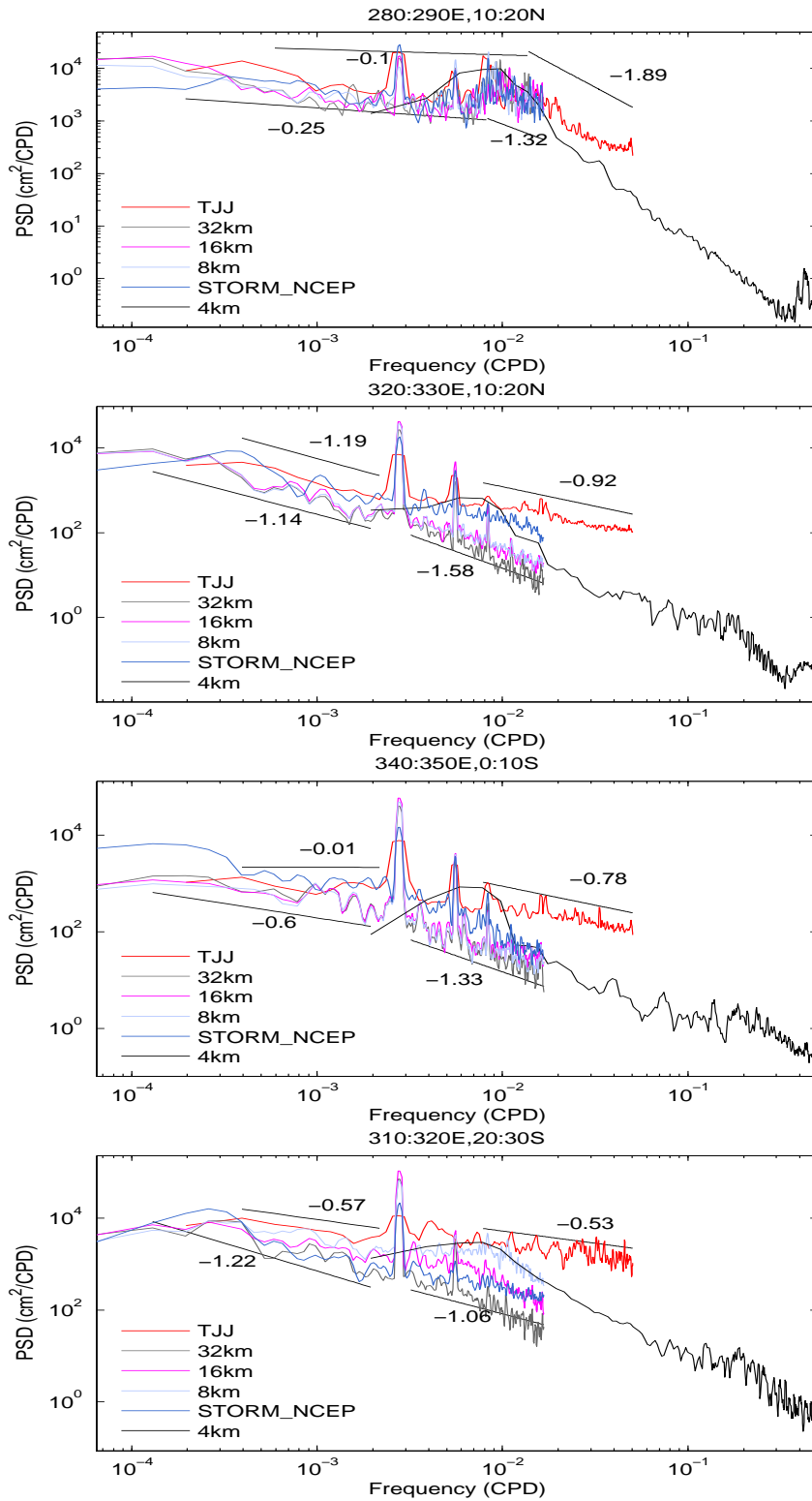
Figure 5.7: Frequency Sea Surface Height spectra from model and TJJ for characteristic $10^\circ \times 10^\circ$ grid boxes, smoothed by a sliding average filter (continued).

that forcing is internal or external or if its an enhancement of seasonal variations. The frequency spectra for the $1/24\,^\circ$ follows a relation that lays in-between the TJJ and the modeled, i.e. for $T > 57$ days $\sigma^{-1.7}$), while for $T < 51$ days $\sigma^{-1.9}$.

In the sub-tropical north Atlantic ($310\,^\circ:320\,^\circ\,\mathrm{E}$, $20\,^\circ:30\,^\circ\,\mathrm{N}$), the main difference in the rate of decay between TJJ and the models can be allocated at periods shorter than 180 days for which TJJ follows $\sigma^{-1.1}$ while the models follow a relation closer to σ^{-2}. The $1/24\,^\circ$ for $30 < T < 170$ days decays to a rate of σ^{-3}, followed by a rather flat spectra ($\sigma^{-0.2}$) for $5 < T < 17$ days and decays at a rate of -3.5 for $T < 5$ days.

The pattern changes significantly at $280\,^\circ:290\,^\circ\,\mathrm{E}$, $10\,^\circ:20\,^\circ\,\mathrm{N}$ where a relative flat spectra (TJJ $\sigma^{-0.1}$, models $\sigma^{-0.25}$) for timescales longer than 120 days is followed by a sharp negative slope (TJJ $\sigma^{-1.9}$, models $\sigma^{-1.3}$) for shorter timescales. At the same location, peaks at the semiannual period and its multiples contain almost the same variability as the annual frequency. The $1/24\,^\circ$ frequency spectra is very similar to the shape of TJJ and modeled for $T > 57$ days and for $T < 51$ days decays fast following σ^{-2}.

Further to the east ($320\,^\circ:330\,^\circ\,\mathrm{E}$, $10\,^\circ:20\,^\circ\,\mathrm{N}$), the rate of decay is almost consistent for all timescales around σ^{-1} which increased for the models to $\sigma^{-1.6}$ for timescales shorter than 310 days. The $1/24\,^\circ$ spectra is rather noisy in this region especially at high frequencies. For periods of $30 < T < 130$ days decays to a rate of $\sigma^{-3.5}$, followed by a relation of $\sigma^{-0.8}$) for $5 < T < 12$ days and decays at a rate of -1.2 for $T < 5$ days.

Moving to the equatorial south Atlantic ($340\,^\circ:350\,^\circ\,\mathrm{E}$, $0\,^\circ:10\,^\circ\,\mathrm{S}$), seasonality appears to be dominating the spectra. The frequency spectra from altimetry is rather flat ($\sigma^{-0.01}$) for timescales longer than 460 days, decaying slowly ($\sigma^{-0.8}$) for timescales shorter than 126 days. The models have a flat slope of $\sigma^{-0.6}$ for $T > 512$ days and a steeper slope of $\sigma^{-4/3}$ for $T < 312$ days. The $1/24\,^\circ$ depicts several secondary peaks at high frequencies while it decays with a rate of -1.1. Further to the south ($310\,^\circ:320\,^\circ\,\mathrm{E}$, $20\,^\circ:30\,^\circ\,\mathrm{S}$), TJJ follows approximately the same relation of $\sigma^{-0.6}$ for all timescales and the same almost describes the models spectra but with a rate of decay close to $\sigma^{-1.1}$. The $1/24\,^\circ$ for $T > 57$ days decays according to $\sigma^{-0.8}$ and for $T < 51$ days the relation is described by $\sigma^{-1.9}$.

Recently Arbic et al. [2012] computed frequency spectra for kinetic energy and streamfunction from AVISO gridded satellite altimeter data and showed that some regions are dominated by an "inverse temporal cascade" while others exhibit a forward temporal cascade. They noted that spectral flux computations are highly susceptible to the smoothing inherent in the construction of gridded altimeter products. This was

the first attempt to address quasi-geostrophic turbulence in the frequency domain. The frequency spectra of streamfunction variance presented by the authors, comparable to the SSH spectra presented here had spectral slopes of -2.6. The spectral slopes shown in **Fig. 5.6** and **Fig. 5.7** are close to the estimates of Arbic et al. [2012] for the MITgcm spectral slopes in high energetic regions, the spectral slopes of TJJ range from -1.1 to -2. The comparison is not absolute since the least square fit depends on the frequency range over which it was estimated. However, the results indicate flatter spectral slopes in the low energetic regions (ranging from -0.3 to -0.9) than the high energy regions.

A clear estimation of the underlying dynamics could not be achieved from the frequency spectra. Geostrophic turbulence is still much better theoretically developed in the wavenumber domain [Ferrari and Wunsch, 2009], which will be addressed in the following section.

5.3 Wavenumber Spectra

Oceanic variability contains all temporal and spatial scales. By applying spectral analysis one can estimate the impact of different scales on the overall variance distribution. Ideally a thorough investigation of ocean variability would arise from studies of long time series sampled at high frequencies with spatial range from millimetres to thousands of kilometers. Since simultaneous high spatial and temporal resolution is not yet available, there is the need to combine different approaches to measure ocean variability.

5.3.1 Global

The global wavenumber spectra of SSH is shown in (**Fig. 5.8**) computed from TJJ and STORM_NCEP. From the shape of the spectra four different regimes can be distinguished, with different drop-off wavelengths for TJJ and STORM_NCEP. Regarding the TJJ wavenumber spectral density for wavelengths longer than 529 km the wavenumber spectra follows relations of $k^{0.3}$, for $99 < \lambda < 265$ km, k^{-3} for $41 < \lambda < 93$ km $k^{-1.1}$ and for wavelengths shorter than 40 km the relation becomes $k^{-1.3}$, where k is the wavenumber and λ is the wavelength. The relations the wavenumber spectrum follows derived from STORM_NCEP can be discribed as follows: for $\lambda > 529$ km $k^{0.3}$, for $66 < \lambda < 198$ km k^{-6}, for $37 < \lambda < 55$ km $k^{-3.3}$ and for $\lambda < 34$ km $k^{-1.1}$. STORM_NCEP depicts steeper wavenumber slopes relative to TJJ at all wavelengths, and especially at the mesoscale and submesoscale between roughly $60 - 200$ km.

The wavenumber spectrum theoretically displays slope values of -5 according to quasi-geostrophic turbulence (QG) and $-11/3$ according to surface quasi-geostrophic
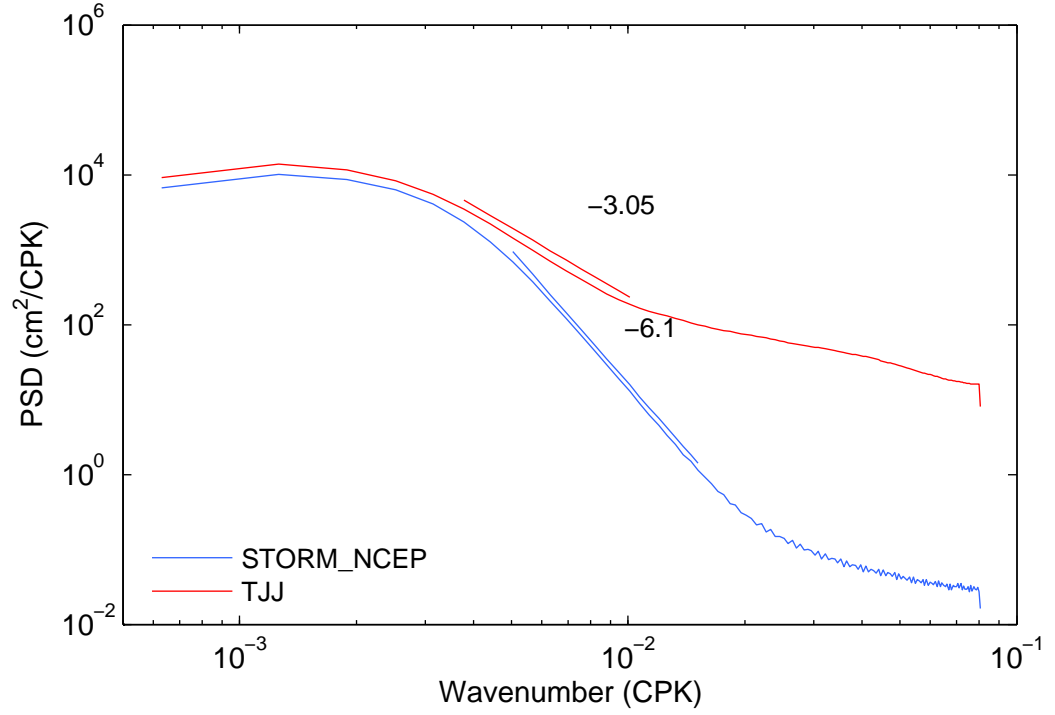
Figure 5.8: Globally averaged Sea Surface Height anomaly wavenumber spectra from TJJ and STORM_NCEP

turbulence (SQG), which describes boundary dynamics not appreciable in QG [Arbic et al., 2012; Vallis, 2006]. Thus, from the theoretical point of view the mesoscale band of TJJ wavenumber spectra is slightly flatter (but close) to SQG, while the corresponding spectra derived from STORM_NCEP is slightly steeper than the slope predicted by QG, indicating that the model underestimates part of the dynamics described by the altimetry.

It needs to be noted that this is a globally averaged spectra and thus contains dynamical characteristics from different regions, however these power laws can be used as reference relations for smaller regions. Due to the along-track resolution of altimeter measurements wavelengths smaller than approximately 70 km was previously thought that can not be accurately estimated in the wavenumber spectra [Le Traon et al., 2008]. More recently Xu and Fu [2012] estimated the noise level from the spectral values at wavelengths of $25 - 35$ km. Also in the global wavenumber spectral results it is shown that model and altimeter data follow approximately the same law for wave-

lengths smaller than 40 km even though the model is noise free, indicating that these
wavelengths might contain also signal apart from the background noise.

5.3.2   Regional

The wavenumber spectra for the extended North Atlantic for TJJ, different resolutions
of MITgcm and STORM_NCEP is shown in **Fig. 5.9**. Altimetry appears to have higher
power spectral density than MITgcm at almost all wavelengths. The wavenumber spec-
tral slopes computed at different wavelengths for TJJ, MITgcm and STORM_NCEP
to best fit their shape are shown in **Table 5.2**. The model's spectra have steeper
slopes than altimetry for all resolutions. Especially for the wavelength band around
$100 < \lambda < 265$ km altimetry follows a decay relation of k^{-3} while the models appears
to be decaying faster following roughly k^{-5}. These results suggest that the models
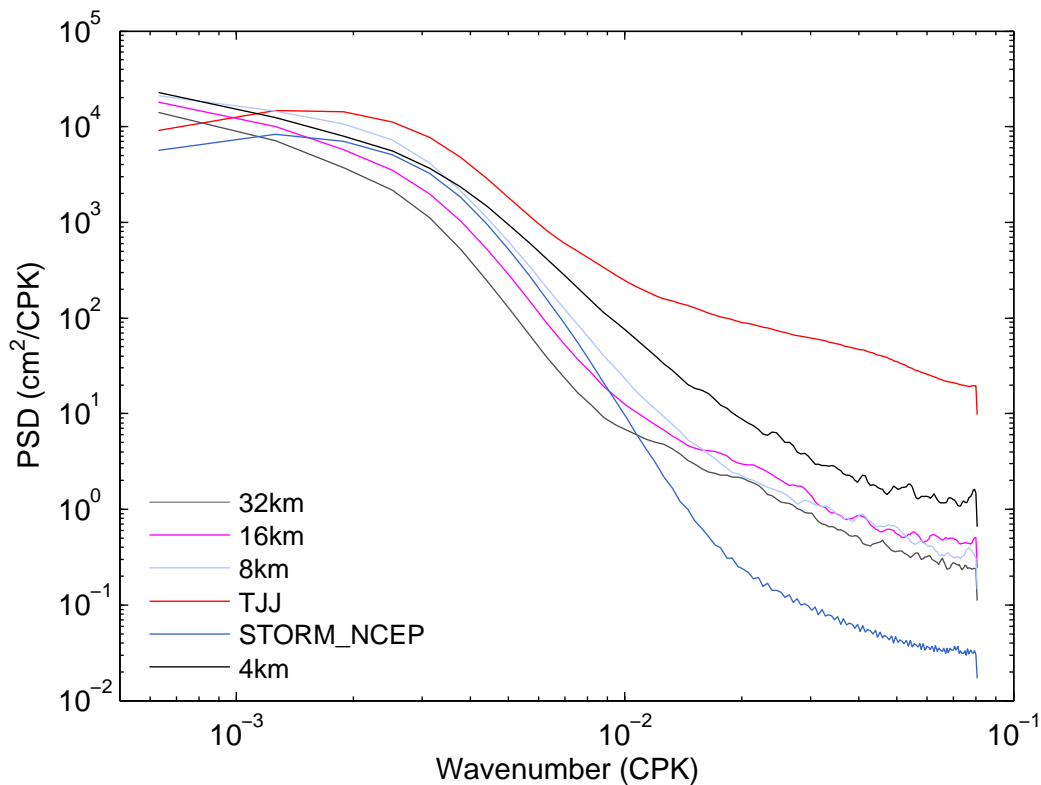
Figure 5.9: Wavenumber Sea Surface Height spectra from model with different resolu-
tions and altimetry.

can be better described by QG, while as the resolution increases and especially at the $1/24°$, SQG becomes more adequate to describe the dynamics. Altimetry is closer to the finite-depth surface quasigeostrophic turbulence theory proposed by Tulloch and Smith [2006], in order to explain the slopes of the order of -3. Their theory takes into account the barotropization of temperature anomalies at large horizontal scales and consequently to a transition scale between -3 and $-5/3$ spectral slopes. This transition according to Tulloch and Smith [2006] theory depends on latitude and the thickness of the fluid. The $-5/3$ slope of wavenumber spectra, which is found at $\lambda < 60\,km$ (see

TJJ	$\lambda > 529\,km$	$99 < \lambda < 265\,km$	$41 < \lambda < 93\,km$	$\lambda < 40\,km$
Slope	0.44	-3.05	-1.22	-1.31
$1/3°$	$\lambda > 317\,km$	$106 < \lambda < 265\,km$	$32 < \lambda < 93\,km$	$\lambda < 32\,km$
Slope	-1.33	-4.72	-1.84	-1.23
$1/6°$	$\lambda > 317\,km$	$99 < \lambda < 265\,km$	$27 < \lambda < 63\,km$	$\lambda < 27\,km$
Slope	-1.16	-4.64	-2.05	-0.82
$1/12°$	$\lambda > 317\,km$	$75 < \lambda < 265\,km$	$26 < \lambda < 53\,km$	$\lambda < 25\,km$
Slope	-0.74	-4.60	-1.60	-1.60
$1/24°$	$\lambda > 317\,km$	$69 < \lambda < 265\,km$	$21 < \lambda < 66\,km$	$\lambda < 21\,km$
Slope	-1.11	-3.60	-2.16	-0.68
STORM_NCEP	$\lambda > 529\,km$	$66 < \lambda < 198\,km$	$37 < \lambda < 55\,km$	$\lambda < 34\,km$
Slope	0.22	-6.07	-2.60	-1.11

Table 5.2: TJJ, MITgcm and STORM_NCEP wavenumber spectra relations

Table 5.2), can theoretically be attributed to three general categories as indicated by Xu and Fu [2010, and reference therein] . These categories include an inverse cascade of small scale energy, the production of gravity waves by unbalanced flows or a direct cascade of energy from the large-scales. However, it is still not clear how the energy of small-scale turbulence affects the large-scale. According to quasi-geostrophy theory, as the forward energy cascade proceeds downscale, if the Rossby number increases, there should be some scale where a breakdown of balance occurs leading to the dominance of highly stratified turbulence instead of quasi-geostrophy. In that case the energy spectrum would have a $-5/3$ due to an ageostrophic forward energy cascade [Xu and Fu, 2010].

The transition from geostrophic to stratified turbulence can occur when the Rossby number approaches 0.4 or larger [Waite and Bartello, 2006]. Xu and Fu [2010] attributed the latitudinal dependence of the spectral slope in the mid-latitudes to the latitudinal variation of the transition wavenumber. While the shallow slope in the
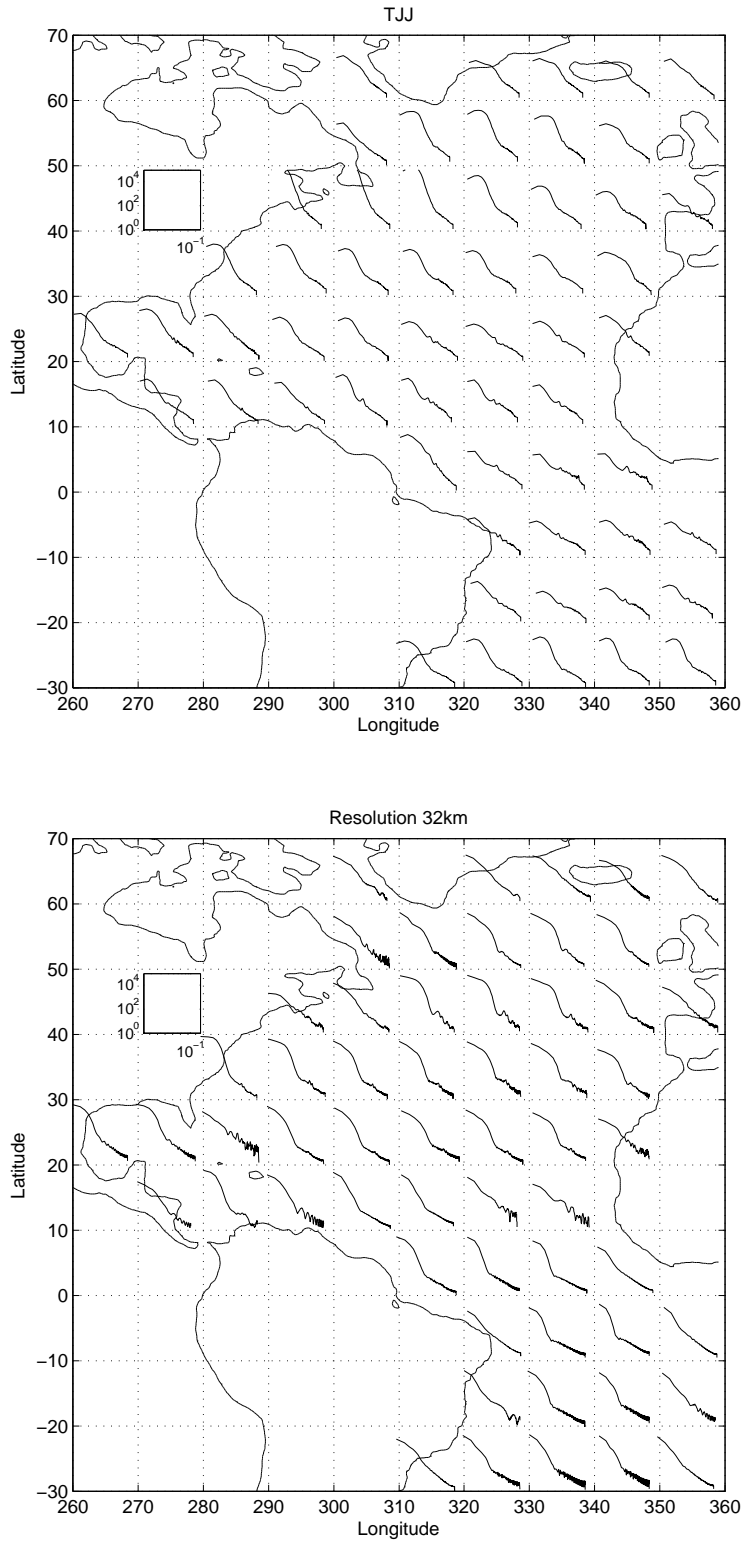
Figure 5.10: Wavenumber Sea Surface Height spectra for TJJ and MITgcm $1/3\,^{\circ}$, $10\,^{\circ} \times 10\,^{\circ}$ grid boxes.
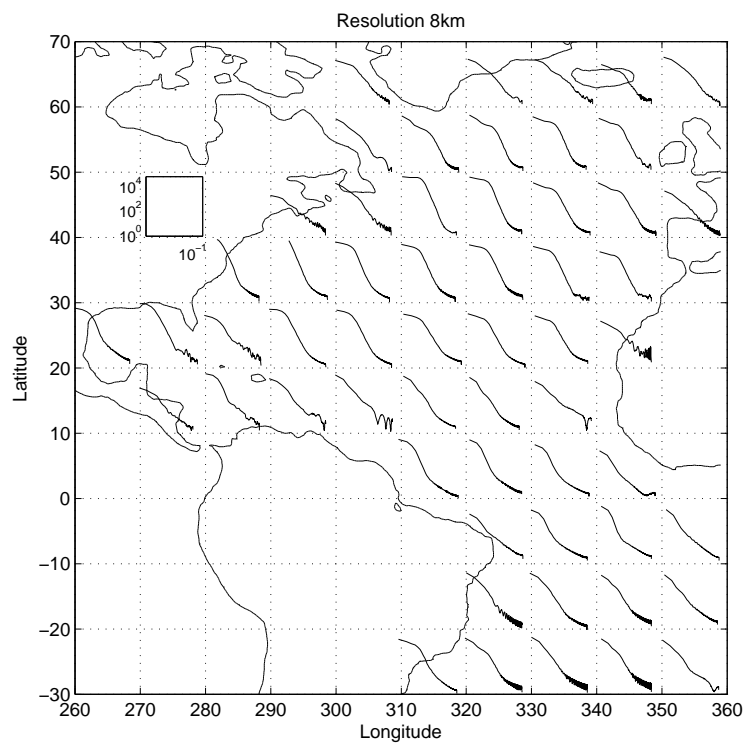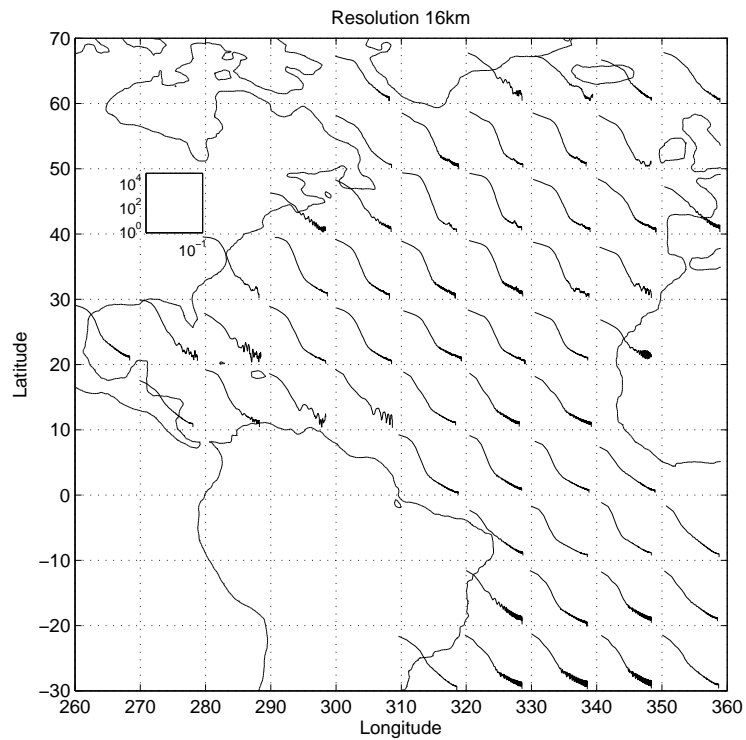
Figure 5.11: Wavenumber Sea Surface Height spectra for MITgcm 1/6 ° and MITgcm 1/12 °, 10 ° × 10 ° grid boxes.
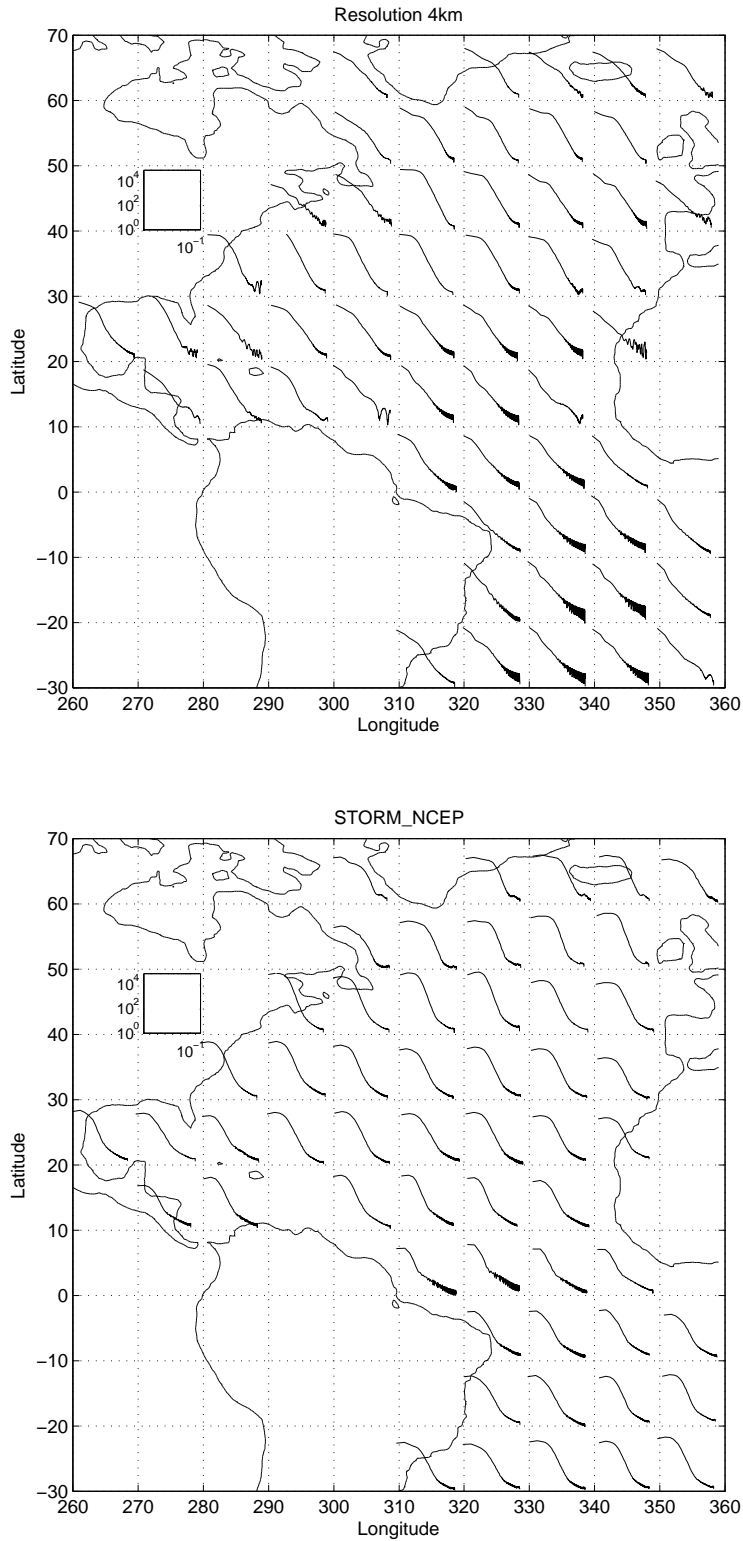
Figure 5.12: Wavenumber Sea Surface Height spectra for MITgcm $1/24°$ and
STORM_NCEP , $10° \times 10°$ grid boxes.

tropical Pacific and the tropical Atlantic oceans were explained by the stratified turbulence theory of Waite and Bartello [2006].

Through the comparison of wavenumber spectra derived by models and altimetry in the Atlantic, it is evident that there is a clear shift towards smaller scales and higher amplitudes as the model resolution increases rendering the spectra much closer to the altimetry. The only exception comes from STORM_NCEP which becomes extremely steep below the sub-mesoscale.

A similar figure as for the frequency spectra (**Fig. 5.3**) but now for wavenumber is shown in **Fig. 5.10** to **Fig. 5.12** for altimetry, MITgcm and STORM_NCEP. Mesoscale eddies range between $100 - 300 \, km$ and are assumed to capture most of the dynamics leading to a k^{-5} spectrum slope for SSH, however if submesoscale is taken into account the wavenumber spectra would lead to a k^{-4} slope [Sasaki and Klein, 2012] shallower than the k^{-5} predicted by quasi-geostrophic turbulence. The latitudinal dependence on the shape of the wavenumber spectra is evident. Previously, Scott and Wang [2005] computing fluxes for grid boxes of $10\,°$, $20\,°$ and $40\,°$ that indicated the importance of sub-domain size in the computation of spectral fluxes in wavenumber space. They attributed the noisy results at $10\,°$ as indicating "the importance of boundary terms relative to interior terms". However, results from all the different sub-domains were qualitatively similar.

A closer look of how the shape of wavenumber spectra changes regionally is shown in **Fig. 5.13** and **Fig. 5.14**. In all regions the wavenumber spectra derived from altimetry is flatter than those derived from MITgcm and STORM_NCEP. It needs to be noted

TJJ	$106 < \lambda \ < 265 \, km$	$\lambda \ < 99 \, km$
	-2.57	-1.01
$1/3\,°$	$106 < \lambda \ < 265 \, km$	$\lambda \ < 99 \, km$
	-5.99	-1.85
$1/6\,°$	$53 < \lambda \ < 265 \, km$	$\lambda \ < 51 \, km$
	-4.39	-0.79
$1/12\,°$	$43 < \lambda \ < 227 \, km$	$\lambda \ < 42 \, km$
	-4.72	-1.61
$1/24\,°$	$33 < \lambda \ < 159 \, km$	$\lambda \ < 24 \, km$
	-3.94	-1.33
STORM_NCEP	$51 < \lambda \ < 198 \, km$	$\lambda \ < 47 \, km$
	-6.89	-1.16

Table 5.3: Wavenumber slopes for $340\,°:350\,°$ E, $50\,°:60\,°$ N
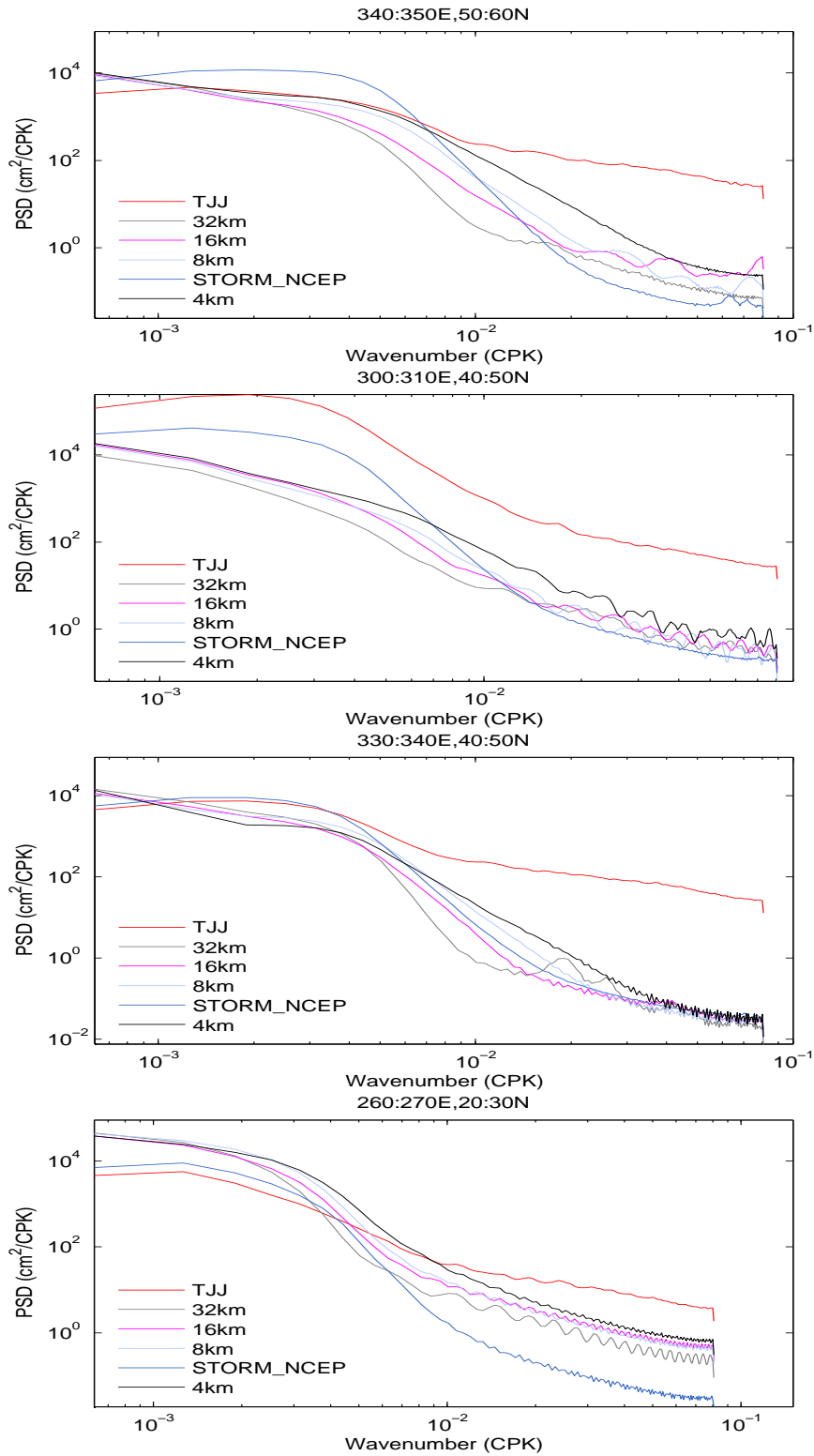
Figure 5.13: Wavenumber Sea Surface Height spectra from model and TJJ for characteristic $10\,^{\circ} \times 10\,^{\circ}$ grid boxes.
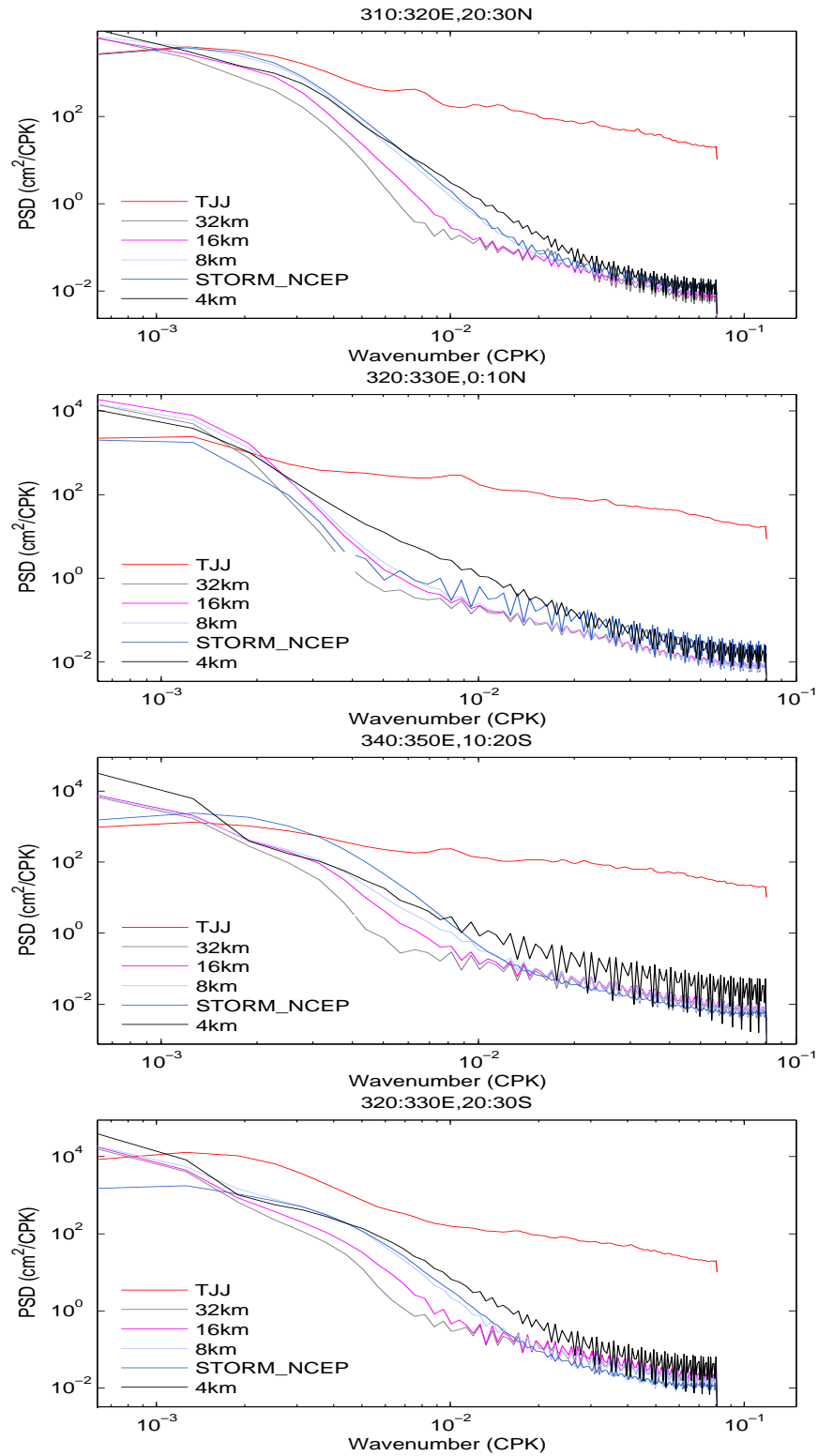
Figure 5.14: Wavenumber Sea Surface Height spectra from model and TJJ for characteristic $10\,^{\circ} \times 10\,^{\circ}$ grid boxes (continued).

that in several sub-domains the wavenumber spectra derived from the model exhibit noisy tails for wavelengths smaller than the sub-mesoscale. This pattern does not correspond to a physical process, but most likely is an artefact of the interpolation.

The first region is located in the subpolar north Atlantic ($340\,^\circ:350\,^\circ$ E, $50\,^\circ:60\,^\circ$ N). The wavenumber slopes derived from the various data sets and for mesoscale wavelengths and shorter are given in **Table 5.3**. For wavelengths within the mesoscale STORM_NCEP has the steeper slope following a relation of the form k^{-7}, followed by the $1/3\,^\circ$ with a decay close to k^{-6}, opposed to approximately k^{-4} for the rest and k^{-3} for TJJ. For the shorter timescales, there are also minor variations between the datasets but all slopes appear to be close to $k^{-4/3}$. As the resolution of the model increases, the wavenumber spectra tends to be closer to the amplitudes captured by the altimetry at the meso and sub-mesoscale.

In $300\,^\circ:310\,^\circ$ E, $40\,^\circ:50\,^\circ$ N (**Table 5.4**) at the sub-polar gyre moving equatorwards convolving with the Labrador current, the altimetry wavenumber spectrum appears to comprise more variance than the simulations. The wavenumber spectral shape of TJJ and MITgcm qualitatively agree, and follow a relation close to k^{-4} but for different cut-off wavelengths, while STORM_NCEP is steeper following k^{-6}. For wavelengths shorter than $65\,km$ all spectra follow approximately $k^{-1/2}$. The wavenumber slopes computed here, for this high energy region, are consistent to the slopes found previously in high energy regions but for the north Pacific by Sasaki and Klein [2012].

TJJ	$69 < \lambda < 317\,km$	$\lambda < 66\,km$
	-4.13	-1.36
$1/3\,^\circ$	$106 < \lambda < 529\,km$	$\lambda < 99\,km$
	-3.50	-1.73
$1/6\,^\circ$	$66 < \lambda < 227\,km$	$\lambda < 63\,km$
	-3.83	-1.53
$1/12\,^\circ$	$58.78 < \lambda < 198\,km$	$\lambda < 57\,km$
	-4.04	-1.58
$1/24\,^\circ$	$59 < \lambda < 198\,km$	$\lambda < 57\,km$
	-3.54	-1.75
STORM_NCEP	$72 < \lambda < 227\,km$	$\lambda < 69\,km$
	-6.22	-1.54

Table 5.4: Wavenumber slopes for $300\,^\circ:310\,^\circ$ E, $40\,^\circ:50\,^\circ$ N

In the same latitudinal band moving further to the east ($330\,^\circ:340\,^\circ$ E, $40\,^\circ:50\,^\circ$ N, still in the vicinity of the North Atlantic Current (NAC) **Table 5.5**) into a slightly

TJJ	$122 < \lambda < 265\,km$	$\lambda < 106\,km$
	-3.11	-1.09
$1/3\,°$	$122 < \lambda < 265\,km$	$\lambda < 106\,km$
	-8.19	-2.10
$1/6\,°$	$76 < \lambda < 265\,km$	$\lambda < 72\,km$
	-6.13	-1.56
$1/12\,°$	$41 < \lambda < 265\,km$	$\lambda < 40\,km$
	-5.32	-1.28
$1/24\,°$	$39 < \lambda < 265\,km$	$\lambda < 38\,km$
	-4.31	-1.92
STORM_NCEP	$72 < \lambda < 265\,km$	$\lambda < 69\,km$
	-6.38	-1.58

Table 5.5: Wavenumber slopes for $330\,° : 340\,°$ E, $40\,° : 50\,°$ N

less energetic region, the TJJ at the mesoscale follows roughly k^{-3} and the models approximately k^{-6} with the exception of the $1/3\,°$ which is steeper than the others at all scales. For shorter scales, the power law that better describes the spectra is $k^{-5/3}$. Quasi geostrophic turbulence appears to be able to describe the altimetry at mesoscale, while closer to the sub-mesoscale ageostrophic forward energy cascade seems to dominate. The models fail to capture the same dynamics, since the spectral slopes for both MITgcm and STORM_NCEP for $122 < \lambda < 265$ km can not be explained physically. However, as the resolution increases the closer the wavenumber spectral slopes gets to a physical meaning, e.g. $1/24\,°$ slope of roughly -4. In the vicinity of the Loop

TJJ	$99 < \lambda < 526\,km$	$\lambda < 93\,km$
	-2.76	-1.15
$1/3\,°$	$122 < \lambda < 317\,km$	¡ 113 km
	-5.48	-1.69
$1/6\,°$	$113 < \lambda < 317\,km$	$\lambda < 106\,km$
	-5.26	-1.60
$1/12\,°$	$106 < \lambda < 317\,km$	$\lambda < 99\,km$
	-5.39	-1.64
$1/24\,°$	$59 < \lambda < 265\,km$	$\lambda < 50\,km$
	-3.88	-1.47
STORM_NCEP	$106 < \lambda < 227\,km$	$\lambda < 99\,km$
	-6.76	-1.69

Table 5.6: Wavenumber slopes for $260\,° : 270\,°$ E, $20\,° : 30\,°$ N

TJJ	$99 < \lambda < 397\,km$	$\lambda < 93\,km$
	-1.76	-1.23
$1/3\,°$	$132 < \lambda < 227\,km$	$\lambda < 122\,km$
	-7.78	-1.73
$1/6\,°$	$99 < \lambda < 317\,km$	$\lambda < 93\,km$
	-6.20	-1.57
$1/12\,°$	$63 < \lambda < 317\,km$	$\lambda < 61\,km$
	-5.36	-1.56
$1/24\,°$	$59 < \lambda < 267\,km$	$\lambda < 41\,km$
	-4.34	-1.63
STORM_NCEP	$76 < \lambda < 317\,km$	$\lambda < 72\,km$
	-5.43	-1.60

Table 5.7: Wavenumber slopes for $310\,° : 320\,°\,E$, $20\,° : 30\,°\,N$.

current ($260\,° : 270\,°\,E$, $20\,° : 30\,°\,N$, **Table 5.6**) the wavenumber spectral shape changes.
For wavelengths close to the mesoscale, the models spectral slopes vary from -4 to -7
much steeper than TJJ's slope of -3. For shorter wavelengths, model's spectra decay
following $k^{-5/3}$, while TJJ is decaying slightly slower following k^{-1}.

In the same zonal band towards the open ocean ($310\,° : 320\,°\,E$, $20\,° : 30\,°\,N$, **Table 5.7**) TJJ wavenumber spectra appears to be decaying almost at the same rate
$k^{-5/3}$ for wavelengths shorter than $396\,km$, rendering the shape of the spectra flat.
This region can be characterised as a low energy region, as can be estimated by the
magnitude of the power spectral density. The models on the other hand, have slopes
ranging from -8 for the $1/3\,°$ to -4 for the $1/24\,°$, shifting to smaller wavelengths as the
resolution increases. For short wavelengths the slopes are around $-4/3$ for altimetry
and $-5/3$ for the models. Though the noisy tails of the models spectra have no physical
meaning, the fact that they converge for all the simulations indicates that probably this
structure arises from the interpolation to the along-track during the pre-processing of
the data.

The wavenumber spectra for an equatorial low energy region ($320\,° : 330\,°\,E$, $0\,° : 10\,°\,N$,
Table 5.8) the spectral slopes for altimetry are almost constant, being around -1.2 for
$144 < \lambda < 794\,km$ and $\lambda < 132\,km$. MITgcm and STORM_NCEP have much steeper
slopes close to -6 for $\lambda > 200\,km$, with the exception of the $1/24\,°$ being best fit-
ted by a -4 slope. For shorter wavelengths ($\lambda < 140\,km$) the wavenumber slopes are
approximately $-5/3$ for all resolutions and models.

In the south Atlantic ($340\,° : 350\,°\,E$, $10\,° : 20\,°\,S$, **Table 5.9**) altimetry has a spectral

slope of -1.45 for $144 < \lambda < 529\,km$ which becomes slightly flatter (-1) for $\lambda < 132\,km$. The models on the other hand have much steeper slopes ranging from $-4\,(1/24\,°)$ to -6 (STORM_NCEP) for wavelengths longer than around $100\,km$, for shorter wavelengths the rate of decay can be described approximately by $k^{-5/3}$ for all simulations, estimated though at extremely noisy tails which contain no physical meaning. Further to the south ($320\,°:330\,°$E, $20\,°:30\,°$S, **Table 5.10**) the spectral shape changes slightly than the previously described. Altimetry has a bit steeper slope (-3) for $122 < \lambda < 396\,km$ while for $\lambda < 113\,km$ the rate of decay is k^{-1}. The wavenumber spectra derived from $1/3\,°$ and $1/6\,°$ MITgcm have a really similar shape following roughly k^{-4} for

TJJ	$144 < \lambda < 794\,km$	$\lambda < 132\,km$
	-1.27	-1.18
$1/3\,°$	$198 < \lambda < 794\,km$	$\lambda < 176\,km$
	-7.07	-1.60
$1/6\,°$	$144 < \lambda < 529\,km$	$\lambda < 132\,km$
	-6.46	-1.60
$1/12\,°$	$176 < \lambda < 529\,km$	$\lambda < 144\,km$
	-6.36	-1.68
$1/24\,°$	$66 < \lambda < 529\,km$	$\lambda < 59\,km$
	-3.70	-1.70
STORM_NCEP	$198 < \lambda < 794\,km$	$\lambda < 159\,km$
	-5.53	-1.61

Table 5.8: Wavenumber slopes for $320\,°:330\,°$E, $0\,°:10\,°$N.

TJJ	$144 < \lambda < 529\,km$	$\lambda < 132\,km$
	-1.45	-1.05
$1/3\,°$	$176 < \lambda < 794\,km$	$\lambda < 159\,km$
	-5.90	-1.61
$1/6\,°$	$122 < \lambda < 794\,km$	$\lambda < 113\,km$
	-4.89	-1.58
$1/12\,°$	$88 < \lambda < 317\,km$	$\lambda < 84\,km$
	-4.91	-1.62
$1/24\,°$	$113 < \lambda < 529\,km$	$\lambda < 106\,km$
	-3.79	-1.90
STORM_NCEP	$79 < \lambda < 317\,km$	$\lambda < 76\,km$
	-6.28	-1.55

Table 5.9: Wavenumber slopes for $340\,°:350\,°$E, $10\,°:20\,°$S.

TJJ	$122 < \lambda < 396\,km$	$\lambda < 113\,km$
	-2.93	-1.10
$1/3°$	$132 < \lambda < 794\,km$	$\lambda < 122\,km$
	-4.79	-1.68
$1/6°$	$113 < \lambda < 794\,km$	$\lambda < 106\,km$
	-4.22	-1.63
$1/12°$	$76 < \lambda < 227\,km$	$\lambda < 72\,km$
	-5.65	-1.70
$1/24°$	$159 < \lambda < 265\,km$	$\lambda < 55\,km$
	-2.99	-1.92
STORM_NCEP	$57 < \lambda < 198\,km$	$\lambda < 55\,km$
	-5.49	-1.45

Table 5.10: Wavenumber slopes for $320°:330°\,E$, $20°:30°\,S$.

$113 < \lambda < 793\,km$ and a power law of the form $k^{-5/3}$ for $\lambda < 100\,km$. The $1/12°$ is similar in shape with STORM_NCEP fitted with a slope approximately -5.5 for $57 < \lambda < 198\,km$ and slopes ranging from -1.7 to -1.45 for $\lambda < 55\,km$. Once again the highest resolution is described by slope extremely close to the altimetry for the wavelengths that fall into the range of physical significance.

The TJJ results regarding the distribution of spectral slopes in high and low energetic regions, are consistent with those presented by Xu and Fu [2010] revealing many regional features. The pattern of the slope variability was related to the energy levels of regional baroclinic activity by Xu and Fu [2010]. Several differences can be indicated between the altimeter and the model's spectral slope distributions. The closest to the altimetry distribution of slopes is the one derived from the $1/12°$ and $1/24°$ resolution although the slopes are steeper in the model by a factor of 2. The $1/3°$ and $1/6°$ resolutions show an expansion of the energetic area of the North Atlantic Current (NAC) even with slopes significantly larger than 5 (as an absolute value), which can not be attributed any physical meaning.

5.4 Discussion and Conclusions

The frequency and wavenumber spectra were computed globally and for the extended North Atlantic from the 18+ year long altimeter data record, and the monthly/daily SSH data available from different resolutions of MITgcm and STORM_NCEP. Through the comparison between altimetry and models, which are free of tides and noise I

addressed the question of the unknown noise level in altimetric observations below wavelengths of 100 km. Dynamical principles through a joint model-data analysis of wavenumber spectra were identified.

The global frequency spectra of SSH from altimetry is aliased by tidal residuals especially at the M2, S2, O1 and M4 frequencies. Other peaks which are significant are related to the seasonal cycle, supported through the comparison with the corresponding spectra derived from STORM_NCEP. The general shape of the frequency spectra described by steeper slopes at higher frequencies and flatter slopes at lower frequencies is consistent with recent results by Arbic et al. [2012] who also pointed out the qualitative similarities between altimetry and gcms. The STORM_NCEP spectra contains less variability at high frequencies, a pattern that can be associated either because the model underestimates submesoscale phenomena or due to the fact that altimetry spectra is dominated by noise at these frequencies.

In the Atlantic region the comparison between altimetry and models is widened with the SSH frequency spectra computed for different resolutions of MITgcm. It is evident that as the resolution increases the model's spectra becomes more similar to the one from the altimetry. Most of the discrepancies arise at high frequencies where the models decay following $\sigma^{-5/3}$ with the exception of the $1/24\,^\circ$ which has -1 spectral slope the same as altimetry for the frequencies they coincide, while for higher frequencies the slope becomes steeper and roughly $-5/3$.

The SSH frequency spectra was estimated in $10\,^\circ \times 10\,^\circ$ sub-domains for all available data-sets covering the overall domain from $260\,^\circ$ E to $360\,^\circ$ E in longitude and $30\,^\circ$ S to $70\,^\circ$ N in latitude. The models have smoother and steeper spectra than TJJ at the zonal band between $20\,^\circ$ N and $60\,^\circ$ N, while it becomes flatter at the vicinity of the Loop current. Along the coast the tidal aliasing of the TJJ frequency spectra is becoming more pronounced even after the corrections, due to the complexity of the tidal dynamics as well as the dynamic response to pressure forcing there, as suggested by Ponte and Lyard [2002]. At mid and high latitudes as indicated previously by Stammer [1997a] SSH variability can be associated with the expansion and contraction of the water column due to seasonal heat flux variations. This could be associated with the intensification of the frequency spectra at frequencies between $120-340$ days at mid latitudes, which are evident especially at high energetic regions and more subtle at low energy regions. In low latitudes the wind stress variations are the primary cause of SSH variations [Stammer, 1997a] resulting in prominent peaks at the annual and semiannual frequencies and a relative flat spectra.

5. ESTIMATION OF FREQUENCY AND WAVENUMBER SPECTRA OF SSH

In high eddy energy regions, where eddies are mainly generated through baroclinic instability dominated by non-linearity, altimeter wavenumber slopes follow a law close to k^{-4} or k^{-3} for the mesoscale range. Surface quasi-geostrophy turbulence which predicts spectral slopes of $-11/3$ appears more appropriate than quasi-geostrophy turbulence which predicts stronger slopes of -5 to provide a dynamical explanation of these spectral slopes. My estimate is consistent with Le Traon et al. [2008] whose spectral slopes significantly differed from a k^{-5} law and therefore disagree with QG turbulence theory. More recently Xu and Fu [2010] argued that surface quasi-geostrophy theory can be applied only in the transition zones from the edge to the core of the high energy regions of the major ocean current systems. They identified the spectrum slope of sea surface height in the core regions of high eddy energy to be close to k^{-4} in the wavelength range of $70 - 250\,\mathrm{km}$, an observation consistent with the dominance of fronts that cannot be fully accounted for by the surface quasi-geostrophy theory. The low energy regions have flatter slopes ranging from -3 to -2 consistent to the one found before [Xu and Fu, 2010]. Thus steep spectrum can be associated with highly non-linear dynamics while the flat spectrum is associated with more linear dynamics.

The wavenumber spectra derived from the models have much stronger slopes than altimetry, even to the extent that they can not attributed physical meaning. This is the case especially for STORM_NCEP. As an overall conclusion it can be said that the models capture more of the dynamics as their resolution increases, shifting gradually to higher wavenumbers and higher amplitudes. In many sub-domains the models fail to capture the dynamics of the sub-mesoscale. Regarding the altimetry I do not have conclusive evidence that for ranges between sub-mesoscale and shorter scales the signal is purely noise.

Chapter 6

Conclusions and Outlook

The goal of this thesis was to investigate eddy variability in the global ocean, focusing on its causes and temporal variations in an effort to study them in combination. We used the longest record available (at the moment) of along-track sea surface height satellite altimetry (comprised by TOPEX/Poseidon, Jason-1 and Jason-2 satellite series) covering the period from 1993 to 2011. Altimetry was compared or complemented to/by two high resolution global circulation models, STORM with global coverage (resolution: $1/10°$) and MITgcm covering most of the Atlantic ocean (resolution: $1/3°$, $1/6°$, $1/12°$ and $1/24°$). The available data-sets provided an ideal basis to apply both statistical and spectral analysis in order to approach the scientific goals of this dissertation as introduced in the first chapter.

The long length of the data-record diminishes even more the uncertainty in the statistical results. This provides the opportunity to re-approach the information that can be derived through the non-gaussianity of sea surface height anomaly. In this study it is found that the probability density function of SSH is best fitted by a theoretical hyperbolic Logistic distribution which can be simplified as an ensemble of Gaussian distributions. The geographical pattern of non-gaussianity is influenced by regions characterised by high energy and no Gauss distributed time series are mostly located in the vicinity of western boundary currents as the Kuroshio and the Gulf Stream. This pattern was confirmed applying a Lillietest. The regions that are far from Gaussian are influenced by more frequent extreme events enhancing the tails of a PDF and rendering it more peaked. The observed pattern strengthens the hypothesis that the deviation from normality is due to inhomogeneities in the ocean [Llewellyn Smith and Gille, 1998] due to mechanisms such as baroclinic instability.

Skewness and kurtosis were investigated before for sea surface height, sea surface temperature and wind stress (e.g. Hughes et al. [2010]; Sura and Gille [2010]; Thompson

and Demirov [2006]). On a global scale the results presented here confirmed that the location of meandering jets can be identified by the formation of a dipole in SSH skewness distribution with positive values poleward and negative values equatorward of the 'central axis' of the jet, which is defined by zero skewness [Thompson and Demirov, 2006] accompanied with a minimum in kurtosis at the center of the jet that is increasing sideways. The next step was taken and studied the seasonal variations of higher order statistics never done previously (to my knowledge).

Seasonal variations of meandering jets and ocean surface circulation processes can be assessed by skewness and kurtosis. The hypothesis is posed that the shedding of eddies can be observed through the seasonal variations of skewness locally, especially in the Agulhas current. Kurtosis distribution also showed seasonal variations in the vicinity of large currents, where the pattern of kurtosis changes in (a)symmetry and/or intensity. The relation of skewness and kurtosis differs with latitude in the global ocean as suggested previously [Gille and Llewellyn Smith, 2000; Sura and Gille, 2010] but also seasonally. The zonal average of higher order statistics can potentially provide an estimate of the rotational regime at different latitudes and its seasonal variations. However, for extended regions or regions with complex circulation as the Antarctic Circumpolar Current it is not easy to draw conclusions partially due to the coarse resolution of $2° \times 2°$.

Regarding the higher order statistics, the outlook is that skewness/kurtosis can be further used to estimate the width of meandering jets (and their seasonal variations) by applying the methodology described by Hughes et al. [2010] to observations. They considered that there is a sharp step in sea level across the jet and random sea level variability producing a Gaussian PDF either side of the step. In their description the resulting PDF consisted of the sum of two Gaussian PDFs with centers separated by a certain distance. For small distance, the resulting PDF had a flatter center region than a single Gaussian. For distance greater than two the PDF became bimodal and kurtosis became smaller, dropping towards its minimum as the separation of Gaussians became larger. Their description even though is theoretical can provide a basis for estimating the seasonal variation of the width of a meandering jet, when applied to altimetry. In a non-theoretical basis the PDF either side of the step are not necessarily Gaussian.

The distribution of root mean square SSH, indicates that the highest values co-incide with major current systems, meandering jets and frontal areas. The inter-comparison between altimetry and STORM_NCEP indicated that the model under-estimates SSH and EKE variability along the North Atlantic Current, the Agulhas, the north-equatorial currents in the Pacific and Atlantic, while higher variability is ac-

quainted at the sub-polar North Pacific and the subtropical oceans. I assume that the differences are due to the sensitivity of the model to high frequency forcing, geographical effects or seasonal shifts of current's axis. While seasonality affects mid and high latitude regions and is a dominating factor on basin-scale as in the case of the Indian Ocean. Despite some differences, it is established that altimetry and STORM_NCEP are in good qualitative agreement in SSH and EKE. The temporal evolution of EKE shared the same sign as the tendency in wind stress magnitude increase on global average, suggesting that eddy variability increases in relation to wind stress forcing.

On a regional scale, I found a pronounced agreement between observed TJJ EKE changes and wind stress variations at the off-equatorial regions, while in tropical regions this is not always the case. EKE variations have a lot in common with variations in wind stress, which in turn have a lot in common with characteristic climate modes of variability present in most of the basins. There are extended parts along the ACC where no local direct relation is found between changes in wind stress and EKE. The same holds in other parts of the ocean, pointing to non-local forcing effects of eddy variability. This implies that regionally no direct relation can be found between changing wind forcing and eddy variability. However, on basin average, changes in eddy energy appear correlated with climate modes.

Eddy kinetic energy has increased over the past 18+ year as estimated in this study by temporal trends amounting to 0.10 % per year for TJJ and 0.72 % per year for STORM_NCEP respectively. The increase is far from uniform but shows a complex pattern. In more detail, away from the tropics similarities are found between the temporal trends discribed by TJJ and STORM_NCEP especially in the North/South Pacific and Atlantic. Wind stress decreased over the period of 1993 to 2009 in the North Pacific, the sub-polar North Atlantic and over large parts of the Indian Ocean, while it increased at the tropical and south Pacific, parts of the subtropical North Atlantic and parts of the South Atlantic.

The pattern of cross correlation of EKE and wind stress, suggests that a simple local relation between wind stress changes and EKE does not exist but does rather reflect basin scale statistics involving local and remote responses to changes in forcing. The causes of increase of EKE are approached with posing some hypothesis. Thus they remain the subject of future research. Since the similarities and differences between TJJ and STORM_NCEP are established, the future outlook is to use STORM_NCEP to estimate the temporal evolution of individual energy conversion terms of the Lorenz cycle and assess their contribution to the overall changes in EKE in order to confirm the hypothesis made.

6. CONCLUSIONS AND OUTLOOK

Ocean variability contains all temporal and spatial scales. By applying spectral analysis one can estimate the impact of different scales on the overall variance distribution. The frequency spectra provide an overview of the frequency characteristics on a global and regional scale. From the frequency spectra the importance of seasonal variations or shorter can be quantified and analysed. I estimated frequency and wavenumber spectra globally and regionally, for both altimetry and models. Through the inter-comparison of data-models the question of the unknown noise level in altimetric observations below wavelengths of 100 km is addressed. Dynamical principles are identified through a joint model-data analysis of and wavenumber spectra.

The investigation of temporal changes in EKE is extended even more through spectral analysis and by including the output of MITgcm with different resolutions. The shape of the frequency spectra of SSH has steeper slopes at higher frequencies and flatter slopes at lower frequencies. The global frequency spectra for altimetry is aliased by tidal residuals especially at the M2, S2, O1 and M4 frequencies. Other peaks are related to the seasonal cycle, supported through the comparison with the corresponding spectra derived from STORM_NCEP. The latter contains less variability at high frequencies, possibly due to underestimation of submesoscale phenomena or due to the fact that altimetry spectra influenced by noise at these frequencies.

In the Atlantic region, through the joint data-model analysis, it is established that as the resolution increases the model's spectra gets closer to the altimetry. Most of the discrepancies arise at high frequencies where the models decay is following $\sigma^{-5/3}$ with the exception of the $1/24\,^{\circ}$ which has a -1 spectral slope the same as altimetry for the frequencies where they coincide. For higher frequencies the slope of MITgcm $1/24\,^{\circ}$ becomes steeper and roughly $-5/3$.

Along the coast the tidal aliasing of the TJJ frequency spectra becomes important due to the complexity of the tidal dynamics as well as the dynamic response to pressure forcing there [Ponte and Lyard, 2002]. Intensification of the frequency spectra at frequencies between $120 - 340$ days at mid latitudes are evident especially at high energy regions and more subtle at low energy regions most likely associated with the expansion and contraction of the water column due to seasonal heat flux variations [Stammer, 1997a]. In low latitudes the wind stress variations are the primary cause of SSH variations resulting in prominent peaks at the annual and semiannual frequencies and a relative flat spectra. A clear estimation of the underlying dynamics could not be achieved from the frequency spectra of SSH. Geostrophic turbulence is still much better theoretically developed in the wavenumber domain [Ferrari and Wunsch, 2009].

The slopes of wavenumber spectra in high energetic regions that are dominated

by non-linearity, follow roughly k^{-4} or k^{-3} at the mesoscale. Thus surface quasi-geostrophy turbulence theory appears more appropriate to provide a dynamical explanation of these spectral slopes. The low energy regions have flatter slopes ranging from -3 to -2 consistent with those found before [Xu and Fu, 2010]. Thus, steep spectrum can be associated with highly non-linear dynamics while the flat spectrum is associated with more linear dynamics. The wavenumber spectra derived from the models have much steeper slopes than altimetry, even to the extent that they can not be attributed to a physical process. As for the frequency domain the models capture more of the dynamics as their resolution increases, shifting gradually to higher wavenumbers and higher amplitudes. Regarding the altimetry there are no conclusive evidence that for ranges between sub-mesoscale and shorter scales the signal is purely noise.

The presented results suggest that a comparison with an even higher resolution model is needed in order to provide more conclusive results in terms of how much of the spectral tails of altimetry is actually noise. In the frequency domain it would be interesting to approach, as a future study, the hypothesis of 'inverse temporal cascade'introduced by Arbic et al. [2012] leaving the question open on whether in some subdomains altimeter data represent real physics or artefacts of the smoothed nature of the gridded altimeter data they used.

References

Apel, J. R. (1987). Principles of ocean physics. *Academic Press*, 38. 4, 15

Arbic, B., Scott, R., Flierl, G., Morten, A., Richman, J., and Shriver, J. (2012). Non-linear cascades of surface oceanic geostrophic kinetic energy in the frequency domain. *J. Phys. Oceanogr.*, in press, doi:10.1175/JPO-D-11-0151.1. 81, 91, 92, 93, 107, 113

Backeberg, B. C., Penven, P., and Rouault, M. (2012). Impact of intensified indian ocean winds on mesoscale variability in the agulhas system. *Nature Climate Change Lett.*, 2:608–612, doi:10.1038/NCLIMATE1587. 68

Böning, C. W., Dispert, A., Visbeck, M., Rintoul, S. R., and Schwarzkopf, F. U. (2008). The response of the antarctic circumpolar current to recent climate change. *Nature Geosc.*, 1, doi:10.1038/ngeo362. 50, 74

Boyer, T., Levitus, S., Garcia, H., Locarnini, R., Stephens, C., and coauthors (2005). Objective analyses of annual, seasonal, and monthly temperature and salinity for the world ocean on a 0.25° grid. *Int. J. Climatol.*, 25(7):931–945. 14

Bracco, A., LaCasce, J. H., and Provenzale, A. (2000). Velocity probability density functions for oceanic floats. *Journal of Physical Oceanography*, 30:461–474. 23

Brachet, S., Le Traon, P. Y., and Le Provost, C. (2004). Mesoscale variability from a high-resolution model and from altimeter data in the north atlantic ocean. *J. Geophys. Res.*, 109, C12025, doi:10.1029/2004JC002360. 5

Chelton, D. B., Schlax, M. G., and Samelson, R. M. (2011). Global observations of nonlinear mesoscale eddies. *Progress In Oceanography*, 91(2):167 –216, doi:10.1016/j.pocean.2011.01.002. 4

REFERENCES

Chelton, D. B., Schlax, M. G., Samelson, R. M., and de Szoeke, R. A. (2007). Global observations of large oceanic eddies. *Geophys. Res. Lett.*, 34(L15606), doi:10.1029/2007GL030812. 1, 4

Chen, S. and Qiu, B. (2010). Mesoscale eddies northeast of the hawaiian archipelago from satellite altimeter observations. *J. Geophys. Res.*, 115, C03016, doi:10.1029/2009JC005698. 60

Collins, C., Reason, C. J. C., and Hermes, J. C. (2012). Scatterometer and re-analysis wind products over the western tropical indian ocean. *J. Geophys. Res.*, 117(C03045):1–16, doi:10.1029/2011JC007531. 5

Dijkstra, H. A. (2008). Dynamical oceanography. *Springer*. 1, 4

Emery, W. J. and Thomson, R. E. (2001). Data analysis methods in physical oceanography. *Elsevier, second and revised edition.* 18

Ferrari, R. and Wunsch, C. (2009). Ocean circulation kinetic energy: Reservoirs, sources, and sinks. *Ann. Rev. Fluid Mech.*, 41:253–282, doi:10.1146/annurev.fluid.40.111406.102139. 5, 6, 23, 27, 49, 69, 79, 80, 92, 112

Ferrari, R. and Wunsch, C. (2010). The distribution of eddy kinetic and potential energies in the global ocean. *Tellus*, 62A(2), doi:10.1111/j.1600-0870.2009.00432.x. 6

Frankignoul, C., de Coëtlogon, G., Joyce, T. M., and Dong, S. (2001). Gulf stream variability and oceanatmosphere interactions. *J. Phys. Oceanogr.*, 31:3516–3528. 40, 41

Fu, L., Vazquez, J., and Parke, M. E. (1987). Seasonal variability of the gulf stream from satellite altimetry. *J. Geophys. Res.*, 92(C1):749–754, doi:10.1029/JC092iC01p00749. 40

Fu, L.-L. (1983). On the wave number spectrum of oceanic mesoscale variability observed by the seasat altimeter. *J. Geophys. Res.*, 88(C7):4331–4341. 6, 8, 79

Fu, L.-L. (2007). Intra variability of the equatorial indian ocean observed from sea surface height, wind, and temperature data. *J. Phys. Ocean.*, 37:188–202, doi:10.1175/JPO3006.1. 50, 71

Fu, L.-L. (2009). Pattern and velocity of propagation of the global ocean eddy variability. *J. Geophys. Res.*, 114(C11017):1–14, doi:10.1029/2009JC005349. 6

Fu, L.-L. and Cazenave, H. (2001). Satellite altimetry and earth sciences. *Academic Press*. 11, 12

Fu, L.-L., Chelton, D. B., Traon, P.-Y. L., and Morrow, R. (2010). Eddy dynamics from satellite altimetry. *Oceanography*, 23(4):14–25. 4, 5, 6, 8, 49

Fu, L.-L. and Le Traon, P.-Y. (2006). Satellite altimetry and ocean dynamics. *C. R. Geoscience*, 338:1063–1076, doi:10.1016/j.crte.2006.05.015. 49

Gille, S. T. and Llewellyn Smith, S. G. (2000). Velocity probability density functions from altimetry. *J. Phys. Ocean.*, 30. 4, 23, 34, 47, 110

Gouretski, V. and Koltermann, K. (2004). Woce global hydrographic climatology. *Berichte des Bundesamt für Seeschifffart und Hydrographie (BSH)*, nr. 35/2004, Hamburg und Rostock, Germany:52. 14

Hsin, Y.-C. and Qiu, B. (2012). Seasonal fluctuations of the surface north equatorial countercurrent (necc) across the pacific basin. *J. Geoph. Res.*, 117(C06001):1–17, doi:10.1029/2011JC007794. 71

Hughes, C. W., Thompson, A. F., and Wilson, C. (2010). Identification of jets and mixing barriers from sea level and vorticity measurements using simple statistics. *Ocean Modelling*, 32:44–57, doi:10.1016/j.ocemod.2009.10.004. 7, 16, 24, 27, 29, 36, 39, 48, 109, 110

Itoh, S. and Yasuda, I. (2010). Characteristics of mesoscale eddies in the kuroshio-oyashio extension region detected from the distribution of the sea surface height anomaly. *J. Phys. Oceanogr.*, 40, doi:10.1175/2009JPO4265.1. 69

Jia, F., Wu, L., and Qiu, B. (2011). Seasonal modulation of eddy kinetic energy and its formation mechanism in the southeast indian ocean. *J. Phys. Oceanogr.*, 41:657–665. 34

Kalnay, E., Kanamitsu, M., Kistler, R., Collins, W., Deaven, D., Gandin, L., Iredell, M., Saha, S., White, G., Woollen, J., Zhu, Y., Leetmaa, A., Reynolds, R., Chelliah, M., Ebisuzaki, W., W.Higgins, Janowiak, J., Mo, K. C., Ropelewski, C., Wang, J., Jenne, R., and Joseph, D. (1996). The ncep/ncar 40-year reanalysis project. *Bull. Amer. Meteor. Soc.*, 77:437–470. viii, 7, 14, 15, 51, 59, 69

Kelly, K. A., Singh, S., and Huang, R. X. (1999). Seasonal variations of sea surface height in the gulf stream region. *J. Phys. Oceanogr.*, 29:313–327. 40

REFERENCES

Langlais, C., Rintoul, S., and Schiller, S. (2011). Variability and mesoscale activity of the southern ocean fronts: Identification of a circumpolar coordinate system. *Ocean Modelling*, pages –, doi:10.1016/j.ocemod.2011.04.010. 43, 62

Lapeyre, G. and Klein, P. (2006). Dynamics of the upper oceanic layers in terms of surface quasigeostrophy theory. *J. Phys. Oceanogr.*, 36. 49

Large, W., McWilliams, J., and Doney, S. (1994). Ocean vertical mixing: a review and a model with a nonlocal boundary layer parameterization. *Rev. Geophys.*, 32:363–403. 14

Lauderdale, J. M., Garabato, A. C. N., Oliver, K. I. C., and Thomas, L. N. (2012). Climatic variations of the work done by the wind on the oceans general circulation. *J. Geophys. Res.*, 117(C09017):1–12, doi:10.1029/2012JC008135. 63

Le Traon, P. Y., Klein, P., Hua, B. L., and Dibarboure, G. (2008). Do altimeter wavenumber spectra agree with the interior or surface quasigeostrophic theory? *J. Phys. Oceanogr.*, 38, doi:10.1175/2007JPO3806.1. 6, 80, 93, 108

Le Traon, P. Y. and Rouquet, M. C. (1990). Spatial scales of mesoscale variability in the north atlantic as deduced from geosat data. *J. Geophys. Res.*, 95(C11):20267–20285. 79

Lee, T. and Marotzke, J. (1998). Seasonal cycles of meridional overturning and heat transport of the indian ocean. *J. Phys. Oceanogr.*, 28:923–943. 41, 42

Llewellyn Smith, S. G. and Gille, S. T. (1998). Probability density functions of large-scale turbulence in the ocean. *Physical Review Letters*, 81(23):5249–5252. 23, 26, 47, 109

Mahadevan, A., Tandon, A., and Ferrari, R. (2010). Rapid changes in mixed layer stratification driven by submesoscale instabilities and winds. *J. Geoph. Res.*, 115:C03017, doi:10.1029/2008JC005203. 74

Marshall, J., Adcroft, A., Hill, C., Perelman, L., and Heisey, C. (1997). A finite-volume, incompressible navier stokes model for studies of the ocean on parallel computers. *J. Geophys. Res.*, 102(C3):5753–5766, doi:10.1029/96JC02775. 14

Meredith, M. P. and Hogg, A. M. (2006). Circumpolar response of southern ocean eddy activity to a change in the southern annular mode. *Geoph. Res. Lett.*, 33(L16608), doi:10.1029/2006GL026499. 5, 50, 73

Monahan, A. H. (2006a). The probability distribution of sea surface wind speeds. part i: Theory and seawinds observations. *J. Climate*, 19(4):497–520, doi:http://dx.doi.org/10.1175/JCLI3640.1. 18, 23

Monahan, A. H. (2006b). The probability distribution of sea surface wind speeds. part ii: Dataset intercomparison and seasonal variability. *J. Climate*, 19(4):521–534, doi:http://dx.doi.org/10.1175/JCLI3641.1. 18, 23

Monahan, A. H. (2007). Empirical models of the probability distribution of sea surface wind speeds. *J. Climate*, 20. 23

Monahan, A. H. (2008). Probability distribution of sea surface wind stresses. *Geoph. Res. Lett.*, 35(L05704), doi:10.1029/2007GL032268. 18, 23

Morrow, R. and Le Traon, P.-Y. (2011). Recent advances in observing mesoscale ocean dynamics with satellite altimetry. *J. Adv. Space Res.*, doi:10.1016/j.asr.2011.09.033. 4, 49

Morrow, R., Ward, M. L., Hogg, A. M., and Pasquet, S. (2010). Eddy response to southern ocean climate modes. *J. Geophys. Res.*, 115, C10030, doi:10.1029/2009JC005894. 5, 62

Niiler, P. P., Maximenko, N. A., Panteleev, G. G., Yamagata, T., and Olson, D. B. (2003). Near-surface dynamical structure of the kuroshio extension. *J. Geophys. Res.*, 108(C6), 3193, doi:10.1029/2002JC001461. 49

Pedlosky, J. (2003). Wave in the ocean and atmosphere, introduction to wave dynamics. *Springer*, pages –. 43

Percival, D. B. and Walden, A. T. (1993). Spectral analysis for physical applications, multitaper and conventional univariate techniques. *Cambridge University Press*. 21

Philander, S. G. H., Hurlin, W. J., and Seigel, A. D. (1987). Simulation of the seasonal cycle of the tropical pacific ocean. *J. Phys. Oceanogr.*, 17:1986–2002. 31

Pickard, G. L. (1975). Descriptive physical oceanography, 2nd edition. *Pergamon Press*, pages –. 44

Polito, P. S. and Sato, O. T. (2008). Global interannual trends and amplitude modulations of the sea surface height anomaly from the topex/jason-1 altimeters. *J. Climate*, 21, doi:10.1175/2007LCLI1924.1. 68

REFERENCES

Ponte, R. M. and Lyard, F. (2002). Effects of unresolved high-frequency signals in altimeter records inferred from tide gauge data. *J. Atm. Ocean. Tech.*, 19. 79, 84, 107, 112

Provost, C. and Le Traon, P.-Y. (1993). Spatial and temporal scales in altimetric variability in the brazil-malvinas current confluence region: Dominance of the semiannual period and large spatial scales. *J. Geophys. Res.*, 98(c10):18037–18051. 79

Qiu, B. (1992). Recirculation and seasonal change of the kuroshio from altimetry observations. *J. Geophys. Res*, 97(C11):17801–17811. 40

Qiu, B. and Chen, S. (2004). Seasonal modulations in the eddy field of the south pacific ocean. *J. Phys. Oceanogr.*, 34:1515–1527. 5

Qiu, B. and Chen, S. (2006). Decadal variability in the large-scale sea surface height field of the south pacific ocean: Observations and causes. *J. Phys. Oceanogr.*, 36(9):1751, doi:10.1175/JPO2943.1. 66

Reverdin, G., Frankignoul, C., Kestenare, E., and McPhaden, M. J. (1994). Seasonal variability in the surface currents of the equatorial pacific. *J. Geophys. Res.*, 99(C10):20323–20344. 37, 39

Richardson, P. L. (2007). Agulhas leakage into the atlantic estimated with subsurface floats and surface drifters. *Deep Sea Research Part I: Oceanographic Research Papers*, 54(8):1361–1389, doi:10.1016/j.dsr.2007.04.010. 35, 36

Sasaki, H. and Klein, P. (2012). Ssh wavenumber spectra in the north pacific from a high-resolution realistic simulation. *J. Phys. Ocean.*, 42:1233–1241, doi:10.1175/JPO-D-11-0180.1. 80, 99, 102

Scharffenberg, M. and Stammer, D. (2011). Statistical parameters of the geostrophic ocean flow field, estimated by jason-1-topex/poseidon tandem mission. *J. Geophys. Res.*, 116(C12011):1–14, doi:10.1029/2011JC007376. 22, 79, 80, 88

Scharffenberg, M. G. and Stammer, D. (2010). Seasonal variations of the geostrophic flow-field and of eddy kinetic energy inferred from the topex/poseidon and jason-1 tandem mission data. *J. Geophys. Res.*, 115(C02008):29, doi:10.1029/2008JC005242. 5, 31, 39, 40, 50, 55

Schott, F. A. and McCreary Jr, J. P. (2001). The monsoon circulation of the indian ocean. *Progress in Oceanography*, 51:1–123. 43

Schouten, M., de Ruijter, W., van Leeuwen, P., and Lutjeharms, J. (2000). Translation, decay, and splitting of agulhas rings in the southeastern atlantic ocean. *J. Geophys. Res*, 105(C9):21913–21925. 36

Scott, R. B. and Wang, F. (2005). Direct evidence of an oceanic inverse kinetic energy cascade from satellite altimetry. *J. Phys. Oceangr.*, 35(9):1650–1666. 99

Serra, N., Kaesse, R. H., Koehl, A., and Stammer, D. (2010). On the low-frequency phase relation between the denmark strait and the faroe-bank channel overflows. *Tellus*, 62A:530–550. 15

Smith, S. D. (1988). Coefficients for sea surface wind stress, heat flux, and wind profiles as a function of wind speed and temperature. *J. Geophys. Res.*, 93(C12):15467–15472. 15

Smith, T., Reynolds, R., Peterson, T., and Lawrimore, J. (2008). Improvements to noaas historical merged land-ocean surface temperature analysis (1880-2006). *J. Climate*, 21:2283–2296. 14

Sokolov, S. and Rintoul, S. R. (2007). Multiple jets of the antarctic circumpolar current south of australia. *J. Phys. Oceanogr.*, 37:1394–1412, doi:10.1175/JPO3111.1. 43, 44, 62

Sokolov, S. and Rintoul, S. R. (2009a). Circumpolar structure and distribution of the antarctic circumpolar current fronts: 1. mean circumpolar paths. *J. Geophys. Res.*, 114(C11018), doi:10.1029/2008JC005108. 43, 62

Sokolov, S. and Rintoul, S. R. (2009b). Circumpolar structure and distribution of the antarctic circumpolar current fronts: 2. variability and relationship to sea surface height. *J. Geophys. Res.*, 114(C11019), doi:10.1029/2008JC005248. 43, 62

Stammer, D. (1997a). Global characteristics of ocean variability estimated from regional topex/poseidon altimeter measurements. *J. Phys. Oceanogr.*, 27:1743–1769. 6, 15, 79, 80, 81, 107, 112

Stammer, D. (1997b). Steric and wind-induced changes in topex/poseidon large-scale sea surface topography observations. *J. Geophys. Res.*, 102(C9):20987–21009. 5

Stammer, D., Böning, C., and Dieterich, C. (2001). The role of variable wind forcing in generating eddy energy in the north atlantic. *Prog. Ocean.*, 48(2-3):289–311, doi:10.1016/S0079-6611(01)00008-8. 50

REFERENCES

Stammer, D. and Böning, C. W. (1992). Mesoscale variability in the atlantic ocean from geosat altimetry and woce high-resolution numerical modeling. *J. Phys. Oceanogr.*, 22:732–752. 79

Stammer, D. and Wunsch, C. (1999). Temporal changes in eddy energy of the oceans. *Deep-Sea Research II*, 46:77–108. 49

Stammer, D., Wunsch, C., and Ponte, R. M. (2000). De-aliasing of global high frequency barotropic motions in altimeter observations. *Geopphys. Res. Lett.*, 27(8):1175–1178. 68

Stammer, D., Wunsch, C., and Ueyoshi, K. (2006). Temporal changes in ocean eddy transports. *J. Phys. Oceanogr.*, 36. 55

Sura, P. (2011). On stochastic advection and mixing barriers. *Ocean modelling*. Submitted. Available at `http://gemini.met.fsu.edu/publications.html`. 7, 16, 24, 29, 40

Sura, P. (2013). Extremes in a changing climate detection, analysis and uncertainty. *Water Science and Technology Library*, 65(Chapter 7):181–222, doi:10.1007/978-94-007-4479-0. 36

Sura, P. and Gille, S. T. (2010). Stochastic dynamics of sea surface height variability. *J. Phys. Oceanogr.*, 40:1582–1596, doi:10.1175/2010JPO4331.1. vii, 7, 16, 18, 23, 24, 26, 27, 29, 30, 34, 36, 39, 47, 109, 110

Thompson, A. F. (2010). Jet formation and evolution in baroclinic turbulence with simple topography. *J. Phys. Ocean.*, 40, doi:10.1175/2009JPO4218.1. 43, 62

Thompson, K. R. and Demirov, E. (2006). Skewness of sea level variability of the worlds oceans. *J. Geophys. Res.*, 111(C05005), doi:10.1029/2004JC002839. 7, 16, 23, 24, 29, 35, 47, 109, 110

Tulloch, R. and Smith, K. S. (2006). A theory for the atmospheric energy spectrum: Depth-limited temperature anomalies at the tropopause. *Proc. Nat. Acad. Sci.*, 103:14690–14694. 95

Tulloch, R. and Smith, K. S. (2009). A note on the numerical representation of surface dynamics in quasigeostrophic turbulence: Application to the nonlinear eady model. *J. Atm. Sc.*, 66, doi:10.1175/2008JAS2921.1. 49

Vallis, G. K. (2006). Atmospheric and oceanic fluid dynamics. *Cambridge University Press.* 1, 5, 6, 27, 44, 93

Vinogradova, N. T., Ponte, R. M., and Stammer, D. (2007). Relation between sea level and bottom pressure and the vertical dependence of oceanic variability. *Geophys. Res. Lett.*, 34(L03608), doi:10.1029/2006GL028588. 68

von Storch, H. and Zwiers, F. W. (1999). Statistical analysis in climate research. *Cambridge University Press.* 17, 20, 21, 27, 29

von Storch, J.-S., Eden, C., Fast, I., Haak, H., Hernandez-Deckers, D., Maier-Reimer, E., Marotzke, J., and Stammer, D. (2012a). An estimate of lorenz energy cycle for the world ocean based on the 1/10° storm/ncep simulation. *J. Phys. Oceanogr.*, in press:–, doi:10.1175/JPO-D-12-079.1. 14, 51, 69

von Storch, J.-S., Fast, I., Haak, H., Maier-Reimer, E., and Stammer, D. (2012b). Vertical eddy fluxes of heat, salt and momentum simulated by the 1/10° storm ogcm. *J. of Advances in Modeling Earth System*, submitted:–. 13

Waite, M. L. and Bartello, P. (2006). The transition from geostrophic to stratified turbulence. *J. Fluid Mech.*, 568:89–108, doi:10.1017/S0022112006002060. 95, 99

Wunsch, C. (1998). The work done by the wind on the oceanic general circulation. *J. Phys. Oceanogr.*, 28. 50

Wunsch, C. and Ferrari, R. (2004). Vertical mixing, energy, and the general circulation of the oceans. *Annu. Rev. Fluid Mech.*, 36:281–314, doi:10.1146/annurev.fluid.36.050802.122121. 6, 50

Wunsch, C. and Stammer, D. (1995). The global frequency-wavenumber spectrum of oceanic variability estimated from topex/poseidon altimetric measurements. *J. Geophys. Res.*, 100(C12):24895–24910. 81

Wunsch, C. and Stammer, D. (1998). Satellite altimetry, the marine geoid and the oceanic general circulation. *Annu. Rev. Earth Planet. Sci.*, 26:219–53. 51

Xu, Y. and Fu, L. (2012). The effects of altimeter instrument noise on the estimation of the wavenumber spectrum of sea surface height. *J. Phys. Oceanogr.*, in press:–, doi:10.1175/JPO-D-12-0106.1. 80, 93

REFERENCES

Xu, Y. and Fu, L.-L. (2010). Global variability of the wavenumber spectrum of oceanic mesoscale turbulence. *J. Phys. Oceanogr.*, 41:802–809, doi:10.1175/2010JPO4558.1. 80, 95, 106, 108, 113

Yuan, D. and Wang, Z. (2010). Hysteresis and dynamics of a western boundary current flowing by a gap forced by impingement of meso-scale eddies. *J. Phys. Oceanogr.*, doi:0.1175/2010JPO4489.1. 49

Zhai, X., Johnson, H. L., and Marshall, D. P. (2010). Significant sink of ocean-eddy energy near western boundaries. *Nature Geosc. Lett.*, doi:10.1038/NGEO943. 51

Zhang, J. and Rothrock, D. (2000). Modelling arctic sea ice with an efficient plastic solution. *J. Geophys. Res.*, 105:3325–3338. 14

Zhang, X. and Church, J. A. (2012). Sea level trends, interannual and decadal variability in the pacific ocean. *Geophys. Res. Lett.*, 39(L21701):1–8, doi:10.1029/2012GL053240. 49, 63, 65